Title
Nuclear level density and gamma-ray strength function of 243Pu

Author
Laplace, Thibault Andre

Publication Date
2016

Peer reviewed|Thesis/dissertation

Nuclear level density and γ-ray strength function of ^{243}Pu

by

Thibault Andre Laplace

A dissertation submitted in partial satisfaction of the
requirements for the degree of
Doctor of Philosophy

in

Engineering-Nuclear Engineering

in the

Graduate Division
of the
University of California, Berkeley

Committee in charge:

Professor Jasmina Vujic, Chair
Professor Lee Bernstein
Professor Magne Guttormsen
Professor Dan Stamper-Kurn

Fall 2016

Nuclear level density and γ-ray strength function of ^{243}Pu

Abstract

Nuclear level density and γ-ray strength function of ^{243}Pu

by

Thibault Andre Laplace
Doctor of Philosophy in Engineering-Nuclear Engineering

University of California, Berkeley

Professor Jasmina Vujic, Chair

The level density and γ-ray strength function of ^{243}Pu have been determined using the Oslo method.
A 12 MeV deuteron beam from the University of Oslo cyclotron was used to populate excited states in the quasi-continuum of ^{243}Pu using the ^{242}Pu(d,p) reaction. The distribution of primary γ-rays as function of the excitation energy has been extracted from particle-γ coincidence data. Based on the Brink-Axel asumption that the primary γ-ray spectrum is proportional to the product of the γ-ray transmission coefficient (which only depends on the transition energy) times the level density at the excitation energy of the final state. The γ-ray strength function is calculated from the γ-ray transmission coefficient assuming pure dipole radiation. Both, the level density and γ-ray strength function, are normalized using available experimental data from libraries.
The level density of ^{243}Pu follows closely the constant-temperature level density formula. An enhancement of the γ-ray strength function is seen at low energies that is similar to that previously measured in other actinides. This structure is interpreted as the M1 scissors resonance. Its centroid $\omega = 2.42(5)$ MeV and its total strength $B = 10.1(15)\ \mu_N^2$ are in excellent agreement with sum-rule estimates. The measured level density and γ-ray strength function were then used to calculate the ^{242}Pu(n,γ) cross section within the Hauser-Feshbach formalism.

Contents

List of Figures

List of Tables

Acknowledgments

I would like to gratefully acknowledge my dissertation committee for their expert advice and proofreading of this thesis. I am thankful to my academic advisor Jasmina Vujic for her support and guidance throughout my graduate studies.

I am deeply grateful to the Nuclear Physics Group at the Oslo Cyclotron Laboratory for its help in performing the experiment and its warm hospitality during my stay in Oslo. Magne Guttormsen played a principal role at every stage of this work. He patiently took the time to guide me through the experimental details and the Oslo method. I'd also like to thank Ann-Cecilie Larsen for providing assistance with TALYS and Fabio Zeiser for the numerous discussions.

I am very thankful to the Bay Area Neutron Group, particularly Bethany Goldblum, Lee Bernstein, Darren Bleuel and Josh Brown for providing feedback on scientific inquiries, general advice and funding. I thank Walid Younes for always finding the time to answer my questions and fruitful discussions.

Finally I thank my mother and father for being the most wonderful parents a son could have. And at last my girlfriend Morayma for her patience, encouragement and love.

Chapter 1

Introduction

All of the four fundamental interactions, except gravity, play an important role in the binding and decay of the complex nuclear many-body quantum system that are nuclei. The interactions between nucleons are the residual part of the more fundamental interactions between quarks inside the nucleons. Since the forces between nucleons are not fully understood, nuclear properties cannot be derived theoretically from the first principle. Furthermore, even if the interactions between nucleons could be described exactly, calculating nuclear properties would still be limited by the gigantic size of the problem. Therefore, the understanding and calculation of nuclear properties relies on approximations and models.

Two of the most important models in nuclear physics are the liquid drop model and the nuclear shell model. The liquid drop model was historically the first model attempting to describe several bulk properties of nuclei. In it, the nucleus is treated as a drop of incompressible quantum liquid. This model leads to the famous semi-empirical mass formula [1] giving the total binding energy of a nucleus as a function of its number of protons and neutrons. Deformations, rotations, vibrations and fission have also been described using the liquid drop model. In contrast, the nuclear shell model [2] describes the nucleus in terms of nucleons moving independently within a mean field. This model was motivated by the presence of shell gaps for neutrons and protons similar to electron shell gaps in atomic physics. Single particle energies can be calculated using the Hartree-Fock formalism and used as input parameters in more advanced calculations incorporating some residual interaction.

Ab initio calculations based on the shell model can reproduce some observables such as energy levels with given spin and parity, and transition strengths and branching ratios between low excitation energy levels. However, with increasing excitation energy, the spacing between levels decreases. When the density of levels is so high that it is impractical or impossible to resolve them, the nucleus can be described with statistical quantities. Two important statistical quantities are the level density (number of energy levels per unit of excitation energy) and the γ-ray strength function (average reduced γ-decay probability independent of the number of final states).

The nuclear physics group at the University of Oslo has developed a method to simultaneously extract the level density and γ-ray strength function below the neutron separation energy from first generation γ-ray spectra [3, 4, 5]. Recent work has provided experimental evidence of the breaking of nucleon Cooper pairs [6]. The $M1$ scissors resonance, corresponding to a collective excitation mode, has been observed in rare-earth nuclei and actinides [7, 8]. The level density and γ-ray strength function are important input parameters for modeling nuclear reactions that proceed via the formation of an intermediate "compound nucleus" whose decay is independent of the way in which it was formed.

In the compound nucleus model, reaction cross sections can be calculated using the Hauser-Feshbach formalism [9]. Reliable reaction cross sections are of importance for astrophysical models of stellar evolution and improved predictions of actinide abundances on Earth [10], advanced nuclear energy systems [11, 12], and the US DOE stockpile stewardship program.

Plutonium and uranium are perhaps the most practically important elements for nuclear applications since they can produce energy via fission reactions. Furthermore, since there are many long-lived isotopes of each of these elements, they offer the possibility of measuring nuclear statistical properties for several isotopes over a large mass region. The $^{238-242,244}$Pu isotopes have long enough half lives (from 14 years for ^{241}Pu to 80 million years for ^{244}Pu) that targets can be fabricated. Because they are neutron rich isotopes, neutron skin oscillation should be strong and pygmy dipole resonances should be observed [13]. Those nuclei are also well deformed and the scissors resonance should be observed as in other actinides. Two measurements were performed at the Oslo cyclotron, populating the ^{240}Pu and ^{243}Pu compound nuclei in the quasi-continuum. This thesis reports the measurement of the nuclear level density and γ-ray strength function of ^{243}Pu, and uses this data to calculate the neutron capture cross section of ^{242}Pu via the Hauser-Feshbach formalism.

Chapter 2 gives a historic overview of the major models and experimental techniques concerning level densities and γ-ray strength functions. The Hauser-Feshbach formalism is briefly introduced. Chapter 3 presents the experimental setup, the detection systems and their calibration, and the extraction of the distribution of measured γ rays as function of the excitation energy of ^{243}Pu, which will be used as the starting point for the Oslo method detailed in Chapter 4. Chapter 5 contains experimental results. The measured level density and γ-ray strength function of ^{243}Pu are then used as input of Hauser-Feshbach calculations in order to predict the ^{242}Pu(n,γ) cross section. Finally, conclusions are drawn in Chapter 6.

Chapter 2

Theory and models

2.1 Nuclear energy level density

At low excitation energies, nuclear levels display a discrete spectrum of low-lying energy levels. With increasing excitation energy, the average spacing between the levels is progressively reduced. Above a few MeV of excitation energy, the spacing between the levels becomes so small that it is difficult to experimentally resolve different levels. At higher energies, the amount of levels per unit energy becomes so high that states are overlapping. This does not depend on the experimental resolution, but on the fact that the average level spacing becomes comparable with the γ width of the level, which is in turn inversely proportional to the level lifetime. Thus, it is necessary to use a continuous description using the nuclear level density, representing the number of levels per unit of excitation energy. This nuclear level density is a fundamental quantity in nuclear physics, and is a crucial ingredient in nuclear reaction theories, allowing prediction of nuclear reactions rates and cross sections used to predict astrophysical processes and to model processes in nuclear reactors.

Several different models have been developed to describe the level density. Semi-empirical models have been developed by analogy with other areas of physics such as thermodynamics. Microscopic models attempt to calculate the level density solving the many-body Schrödinger equation. In the following sections, the most common models are introduced and the experimental methods to extract level densities. In addition, a comparison between the major databases of level densities is given.

2.1.1 Semi-empirical models

Foundation

In his 1936 seminal paper [14], Hans Bethe presented a first theoretical calculation of the level density by comparing the excited states of a nucleus to a Fermi gas, and the logarithm of the level density to the gas entropy. The derived level density, ρ_{int}, is given

as a function of the excitation energy of the nucleus, E_x:

$$\rho_{\text{int}}(E_x) = \frac{\sqrt{\pi}}{12}\frac{\exp(2\sqrt{aE_x})}{a^{\frac{1}{4}}E_x^{\frac{5}{4}}}, \tag{2.1}$$

where a is the level density parameter. A possible empirical formulation of this parameter is given by:

$$a = \frac{\pi^2}{4}\frac{A}{\xi_0}, \tag{2.2}$$

where A is the mass number of the considered nucleus and ξ_0 is the average Fermi energy for protons and neutrons. The derived level density can be compared to experimental resonance spacing data. The latter gives information about the average energy difference between two consecutive levels at a given excitation energy. Available resonance spacing data are generally for s- or p-wave neutrons, which will only populate levels with total angular momentum equal to $\pm 1/2$ or $\pm 3/2\ \hbar$ with respect to the total angular momentum of the target. Thus, the angular momentum dependence of the level density needs to be known to compare it to resonance data. Based on Bethe's initial expression, and more experimental data available, Ericson [15] proposed a spin dependent formulation of the level density, known as the Fermi-gas Model:

$$\rho_{\text{int}}^{\text{FG}}(E_x, J) = \frac{2J+1}{2\sqrt{2\pi}\sigma^3}\exp\left(-\frac{(J+1/2)^2}{2\sigma^2}\right)\frac{\sqrt{\pi}}{12}\frac{\exp(2\sqrt{aU})}{a^{\frac{1}{4}}U^{\frac{5}{4}}}, \tag{2.3}$$

where J is the total angular momentum of the nucleus, σ is the spin cut-off parameter, which represents the width of the angular momentum distribution, and U is a shifted energy given by:

$$U = E_x - \Delta, \tag{2.4}$$

where Δ is an empirical parameter included to take into account the pairing energy. Summing over all spins yields the total level density:

$$\rho_{\text{int}}^{\text{FG}}(E_x) = \frac{1}{\sqrt{2\pi}\sigma}\frac{\sqrt{\pi}}{12}\frac{\exp(2\sqrt{aU})}{a^{\frac{1}{4}}U^{\frac{5}{4}}}. \tag{2.5}$$

Thus, the total level density is determined by the three parameters: a, σ, and Δ.

Various parametrizations of a, σ, and Δ are available. Moreover, the level density parameter can be taken as either independent or dependent of the excitation energy. W. Dilg *et al.* [16] and more recently T. von Egidy and D. Bucurescu [17, 18, 19] compiled values of the three parameters for over 300 nuclei.

The constant temperature model

In 1965, A. Gilbert and A.G.W. Cameron [20] proposed a new formulation of the level density, based on experimental data. Experimental evidences show that the cumulative

number of levels in a nucleus, $N(E_x)$, follows an exponential law:

$$N(E_x) = \exp\left(\frac{E_x - E_0}{T}\right), \tag{2.6}$$

where the energy shift E_0 and a parameter T are to be adjusted to the experimental discrete levels. The level density $\rho_{\rm int}^{\rm CT}$ is obtained by taking the derivative of the cumulative number of levels with respect to the excitation energy:

$$\rho_{\rm int}^{\rm CT}(E_x) = \frac{dN(E_x)}{dE_x} = \frac{1}{T}\exp\left(\frac{E_x - E_0}{T}\right). \tag{2.7}$$

Considering the nucleus as a microcanonical ensemble, the nuclear entropy of the system, $S(E_x)$, is proportional to the logarithm of the level density:

$$S(E_x) = k_B \ln\left(\frac{\rho_{\rm int}^{\rm CT}(E_x)}{\rho_0}\right), \tag{2.8}$$

where k_B is the Boltzmann and ρ_0 is a constant set to ensure the third law of thermodynamics (i.e $S(T \to 0) = S_0$ with S_0 being a constant). The nuclear temperature, T_{nuc}, is defined as:

$$T_{nuc} = \left[\frac{\partial S(E_x)}{\partial E_x}\right]^{-1} = k_B T. \tag{2.9}$$

The constant T is equivalent to the nuclear temperature, but expressed in units of energy.

The constant temperature model is, in general, only used to describe the level density up to a given excitation energy E_M. Above this excitation energy, the Fermi-gas model is used. The level densities obtained from the Fermi-gas model and the constant temperature model, as well as their derivatives, have to be equal at the matching excitation energy E_M.

The physical picture for this model is that the nucleus undergoes a first order phase transition over the constant temperature energy range, and then has an increasing temperature with excitation energy for the Fermi-gas part of the level density. The first order phase transition has been traditionally associated with the transition from superfluid to non-superfluid behavior arising from the breaking of the nuclear pairing interaction.

The generalized superfluid model

Similarly to the constant temperature model, the generalized superfluid model [21, 22] distinguishes two energy regions. At high energies, the level density is described by the Fermi-gas model. At low energy, the concepts of pairing and shell effects are included in the model. Similarly to the Fermi-gas model, the level density is written as:

$$\rho_{\rm int}^{\rm GSM}(E_x) = \frac{1}{\sqrt{2\pi}\sigma}\frac{e^S}{\sqrt{D}}, \tag{2.10}$$

where S is the entropy and D is the determinant related to the saddle-point approximation from the partition function method [23]. All the parameters are defined at the critical energy U_c:

$$\left\{ \begin{array}{rcl} U_c & = & a_c T_c^2 + E_{cond} \\ S_c & = & 2a_c T_c \\ D_c & = & \frac{144}{\pi} a_c^3 T_c^5 \\ \sigma_c^2 & = & \frac{6}{\pi^2} A^{1/3} a_c \langle m^2 \rangle T_c \end{array} \right. , \tag{2.11}$$

where a_c is the critical level density parameter, T_c is the critical temperature, E_{cond} is the condensation energy, characterizing the decrease of the ground state energy of the superfluid phase relative to the Fermi gas phase, and $\langle m^2 \rangle$ the average square of the angular momentum projection of the single particle states near the surface. Using the superfluid equation of state [22], it is possible to calculate the level density below the critical energy.

All of the models above are phenomenological rather than microscopic. Several parameters are introduced in order to reproduce experimental data. Those parameters are dependent on the mass number, shell effects and sometimes the excitation energy, which makes it difficult to calculate them and even harder to predict them for poorly known nuclei.

Collective enhancement

The phenomenological models described so far do not explicitly take into account collective effects. The total nuclear level density, ρ_{tot}, can be expressed as:

$$\rho_{tot}(E_x, J) = \rho_{int}(E_x, J) K_{rot}(E_x) K_{vib}(E_x), \tag{2.12}$$

where K_{rot} and K_{vib} are respectively the rotational and vibrational enhancement of the level density, which can be considered as additional degrees of freedom "built" on the intrinsic single-particle wavefunctions for high-lying nuclear states.

The rotational enhancement can be estimated by [24]:

$$K_{rot}(E_x) = \left\{ \begin{array}{ll} 1 & \text{for spherical nuclei,} \\ \Theta_\perp T & \text{for deformed nuclei,} \end{array} \right. \tag{2.13}$$

where $\Theta_\perp$ is the projection of the nuclear moment of inertia perpendicular to the symmetry axis given by:

$$\Theta_\perp = \frac{2}{5} \frac{m_0 R^2 A}{(\hbar c)^2}, \tag{2.14}$$

where m_0 is the neutron mass given in energy units, R is the nuclear radius and A the total number of nucleons. $\Theta_\perp$ is expressed in units of inverse energy. T is the nuclear temperature expressed in units of energy, and depends on the excitation energy.

A damping parameter can be added in order to have the rotational enhancement vanish for high excitation energies, where the breakdown in axially-symmetric deformation due to the mixture of levels from many harmonic oscillator shells makes these enhancements vanish.

A liquid drop model estimation of the vibrational enhancement is given by [24]:

$$K_{\text{vib}}(E_x) \approx \exp(0.0555 A^{\frac{2}{3}} T^{\frac{4}{3}}). \tag{2.15}$$

Different calculations of the vibrational enhancement based on a more microscopic approach are detailed in [25].

Vibrational and particularly rotational enhancement can have a large effect on the level density ($K_{vib} \sim 3$, $K_{rot} \sim 10 - 100$ [26]).

2.1.2 Microscopic models

Although a reasonable agreement can be achieved between experimental data and semi-empirical or phenomenological models such as the ones mentioned above, they are based on various simplifying approximations. Shell effects, pairing, collective enhancement and parity distribution are either not taken into account or included in some parameters calculated to reproduce experimental data. Microscopic models have been developed in order to be able to describe fine structure of the level density as well as being able to predict it for nuclei far from the valley of stability where little to no experimental data are available.

Most microscopic theories treat the nucleus as a quantum mechanical many-body system, in which the velocities of nucleons are small enough to neglect relativistic effects. Also, interactions between nucleons are generally limited to a two-body interaction. A full description is given by the many-body Schrödinger equation:

$$H\left|\Psi\right\rangle = \left[-\sum_{i=1}^{A}\frac{\hbar^2}{2m}\Delta_i + \sum_{i<j}^{A} v(i,j)\right]\left|\Psi(1,...,A)\right\rangle = E\left|\Psi(1,...,A)\right\rangle, \tag{2.16}$$

where H is the Hamiltonian of the system with energy E and described by the wave-function $|\Psi\rangle$, m is the nucleon mass, Δ_i is the Laplacian for the nucleon i, and $v(i,j)$ is the two-body interaction between the nucleon i and the nucleon j. This Hamiltonian can be written in the second quantization formalism using single particle energies ε_k:

$$H = \sum_k \varepsilon_k a_k^\dagger a_k + \frac{1}{2}\sum_{k,l,m,n} V_{klmn} a_k^\dagger a_l^\dagger a_n a_m, \tag{2.17}$$

where $a_k^\dagger$ and a_k are, respectively, creator and annihilation operators of a particle in the state k. V_{klmn} is the matrix element of the two-body interaction. Most current microscopic models neglect the three-body interaction or any higher order contribution due to the high increase in complexity and computing power, thereby allowing the form

given in Eq. (2.17) to be considered valid. Successful ab initio calculations including the three-body interactions have been performed for nuclei with masses up to $A = 132$ [27] focusing on reproducing the ground state energy and the first few excited states.

Combinatorial calculation

Combinatorial calculations of the level density have been first suggested by Hillman and Grover [28]. The nuclear level density can be calculated as a function of the excitation energy, the spin and parity by means of a combinatorial counting of excited many particle-hole states. No assumptions on the spin and parity distributions are made. Recently, with the increase in computational power, the method has gained interest and collective effects are taken into account [29, 30, 31]. Comparison of the calculations made by Uhrenholt *et al.* [30] to experimentally measured data using the Oslo method [32, 33, 34, 35] are shown in Figure 2.1. Relatively good agreement is found in the rare-earth region. The work of Goriely *et al.* [31] contains calculated level densities using a combinatorial approach for more than 8500 nuclei. The model predicts s- and p-wave neutron resonance spacings with a degree of accuracy comparable to the best semi-empirical models.

Shell model monte carlo

The exact diagonalization of the Shell-Model Hamiltonian given in Equation(2.17) can, in principle, give an accurate and consistent description of a wide range of nuclear properties (assuming correct single-particle energies and two-body matrix elements). Computation capabilities limit this method to light nuclei or heavier nuclei that can be treated as an inert core plus a few valence nucleons. The Shell Model Monte Carlo method could potentially consider all correlation effects exactly within the limits of the two-body interaction even though exact diagonalization of the Hamiltonian is not performed. In the Shell Model Monte Carlo method, the path integral of the imaginary-time evolution operator, $\exp(-\beta H)$, where $\beta \in \mathbb{R}$, is evaluated by a Monte Carlo calculation. This method does not result in the complete solution of the problem (i.e. all eigenvalues and eigenstates of the Hamiltonian of the system), but expectation values corresponding to some observables in the grand canonical ensemble can be determined [36, 37]. This method currently works for even-even nuclei only, with masses ranging from $50 < A < 70$ and in the rare-earth region ($A \sim 150$). A good agreement with experimentally measured data is achieved [38].

2.1.3 Experimental methods to extract the level density

Spectroscopy

At low energy, discrete levels can be extracted by coincident γ-ray spectroscopy following various types of nuclear reactions. They can be grouped in energy bins to give an equivalent of the level density. Depending on the nuclear reaction used, not all spins might

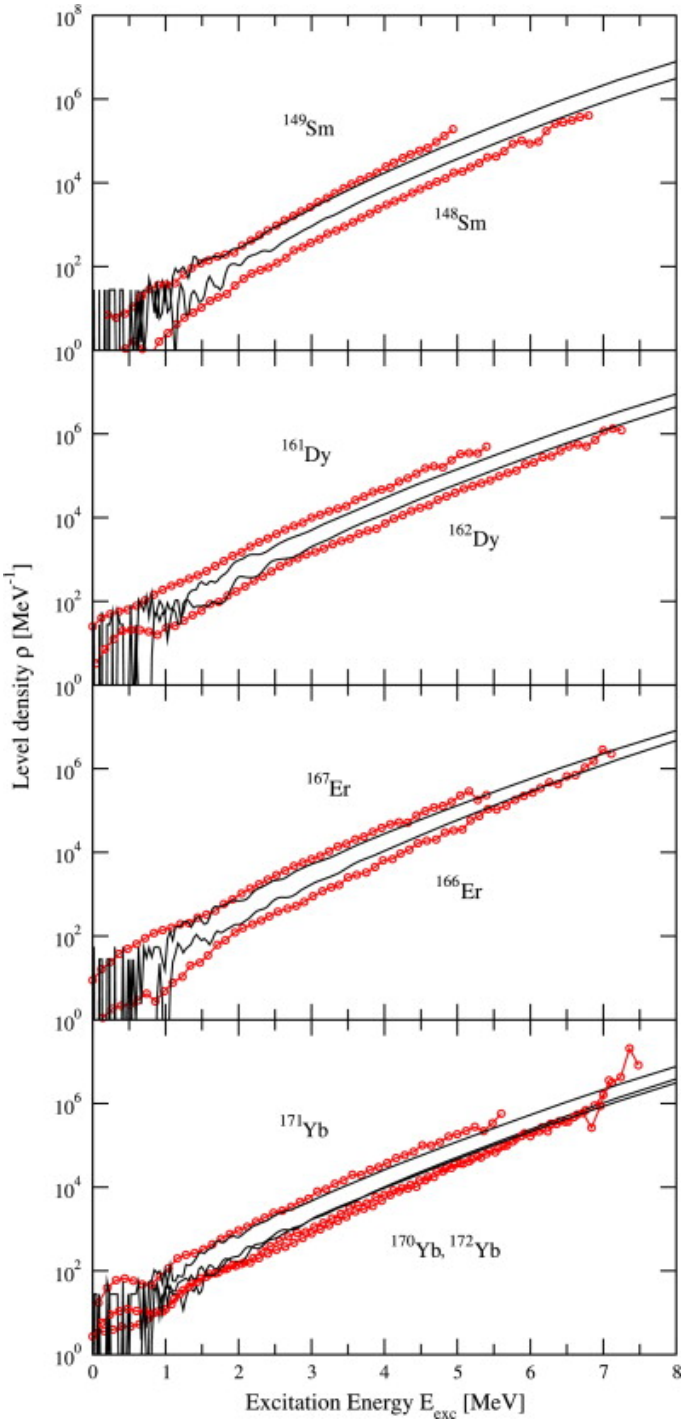

Figure 2.1: Comparison of the combinatorial calculation of the level density as a function of the excitation energy by Uhrenholt *et al.* [30] (black solid lines) to experimentally extracted level density using the Oslo method [32, 33, 34, 35] (red dots). Figure taken from Ref. [30].

be excited. However, the level scheme is often complete up to the excitation energies of $E_{\rm x} \approx 2\Delta$ where the first pair of nucleons breaks up (Cooper pairs). Adopted levels can be found in databases such as the Evaluated Nuclear Structure Data File (ENSDF)[1].

Resonance spacing

The level density at the neutron or proton separation energy can be calculated using resonance spacing data [25]. For example, considering the following reaction:

$$n + {}^{A}_{Z}X \rightarrow {}^{A+1}_{Z}Y^{*}, \tag{2.18}$$

the average neutron resonance spacing of the nucleus X for s-wave neutrons, D_0, can be written as function of the level density for the nucleus Y at the neutron separation energy S_n:

$$\frac{1}{D_0} = \frac{1}{2}\left[\rho_Y(S_n, J_Y = I_X + 1/2) + \rho_Y(S_n, J_Y = I_X - 1/2)\right], \tag{2.19}$$

where J_Y is the angular momentum of the product nucleus Y, and I_X is the total ground state angular momentum of the target nucleus X. This simple formulation assumes equal contribution from both parities to the level density at the neutron separation energy. Knowing the resonance spacing parameter, the previous relation can be used to calculate the level density. For a target nucleus with total ground state angular momentum $I_X = 0$, the equation simplifies to:

$$\frac{2}{D_0} = \rho_Y(S_n, J_Y = 1/2). \tag{2.20}$$

Ericson fluctuations

For excitation energies where the average level width, Γ, is larger than the average spacing between levels, D, the Ericson fluctuation method can be used [39]. The method relies on carefully measuring the variance of the total neutron cross section, $\sigma_{\rm T}$, which allow calculation of the level density of the compound nucleus, ρ_{CN}, using the following relation:

$$\begin{aligned} var\sigma_{\rm T} &\equiv < (\sigma_{\rm T} - < \sigma_{\rm T} >)^2 > \\ &= 2\left[\frac{\pi\chi_P^2}{(2I_P+1)(2I_t+1)}\right]^2 \frac{1}{\pi\Gamma\rho_{\rm CN}} \sum_J \frac{(2J+1)^2}{H(J)} \sum_i (\mathcal{T}^J_{nl})^2, \end{aligned} \tag{2.21}$$

where χ_P is the reduced wavelength of the projectile, I_P is the spin of the projectile, I_t is the spin of the target, Γ is the average level width, $H(J)$ is the fraction of compound nucleus levels with spin J, and $\mathcal{T}^J_{nl}$ is the transmission coefficient for a neutron of orbital angular momentum l coupled to the compound nuclear spin J. To extract the level density of the compound nucleus, $\rho_{\rm CN}$, one needs to experimentally measure the variance

[1] http://www.nndc.bnl.gov/ensdf/

of the total cross-section, $var\sigma_{\mathrm{T}}$, along with the average level width Γ. Then, the neutron transmission coefficients are calculated using the Hauser-Feshbach formalism, and the $H(J)$ parameter is obtained using a calculated spin distribution (generally using a calculated spin-cutoff parameter). This method provides a mean to determine the level density at high excitation energies where other techniques are difficult or impossible to use [40].

The particle evaporation method

This method consists of measuring the particle evaporation spectra following a nuclear reaction [41]. In the Hauser-Feshbach formalism, the particle evaporation spectra can be calculated and their shape depend only on the nuclear temperature, which can be derived from the level density, and the transmission coefficient of the outgoing particle. The latter can be calculated using optical model potentials, which should be accurate for nuclei with well measured elastic scattering and total cross sections. The accuracy of this method depends on the ability to accurately calculate transmission coefficients and meeting the underlying assumptions of the Hauser-Feshbach theory, including the formation of a compound nucleus. Pre-equilibrium emission and direct reaction could result in distorted evaporation spectra [41]. Using this method, the level density can be calculated for energies above the neutron separation energy but well below the two neutron emission threshold (in order to avoid non-equilibrium emission).

The Oslo method

The Oslo method allows simultaneous extraction of the level density and the γ-ray strength function [5]. Coincidence measurement of particles and γ rays following a nuclear reaction are used to construct particle-γ-ray matrices. The matrix of primary γ rays (which consists of the spectrum of the first γ ray emitted after creation of the compound nucleus as a function of the excitation energy of the compound nucleus) is extracted [3]. The Brink-Axel hypothesis [42, 43], which states that the γ ray emission probability depends only on the energy of the transition and not on the initial or final excitation energy of the transition, is assumed. The functional form of the level density and transmission coefficient can be extracted from the primary γ-ray matrix. To obtain absolute values, normalization using discrete levels at low energy and neutron or proton resonance data at the binding energy is necessary. The accessible range of energies for the extraction of the level density using the Oslo method is limited to energies below the neutron binding energy.

2.1.4 Level density in databases

Level densities and γ-ray strength functions are key ingredients to calculate cross sections using the Hauser-Feshbach formalism. The Evaluated Nuclear Data File (ENDF/B-

VII.1) [11] library adopts the cross sections given by the Japanese Evaluated Nuclear Data Library (JENDL-4.0) [44] library for most minor actinides. Parameters used for the level density are unfortunately not available when the evaluation is not based on JENDL-4.0. The JENDL-4.0 [44] contains cross sections which are calculated using the Comprehensive COde for Nuclear data Evaluation (CCONE) code [45]. Talys-based Evaluated Nuclear Data Library (TENDL-2014) [46] uses TALYS [26]. In the codes underlying the JENDL-4.0 and TENDL-2014 evaluations, the level density is described by the constant temperature model [20] at low energies and the Fermi gas model [15] above a matching energy, but with different parameters. Figure 2.2(a) shows the level density for ^{241}Pu and ^{242}Pu used by JENDL-4.0 and TENDL-2014. The difference is striking for ^{241}Pu. The slope given by the constant temperature is different at low energy ($T_{JENDL} = 0.37$ MeV, $T_{TENDL} = 0.41$ MeV) and the matching excitation energy marking the transition from the constant temperature model to the Fermi gas model is different ($E_M^{JENDL} = 3.6$ MeV, $E_M^{TENDL} = 5.1$ MeV). Those differences are highlighted in Figure 2.2(b) where the ratio between the level density used by JENDL-4.0 and the one used by TENDL-2014 is plotted for $^{239-243}$Pu. The level density plotted for the isotope with A nucleons is the one used for the calculation of the neutron capture cross section in the $(A-1)$ nucleons isotope. Of the nuclei shown in this figure, only the level density of ^{240}Pu shows reasonable agreement between the databases and is used for the ^{239}Pu(n,γ) cross section calculation. The level density used in TENDL-2014 shows discontinuity at the matching excitation energy for several isotopes which explains the discontinuities in the ratios from Figure 2.2b.

In the TENDL-2014 input files, the default TALYS parameters of the level density are modified. Figure 2.3 shows the ratio between the level density used by JENDL-4.0 to the default level density in TALYS-1.6 [26]. The default level density model in TALYS is the constant temperature model, as used in TENDL-2014 and JENDL-4.0. The agreement is better but there are still discrepancies of up to a factor of two for excitation energies below the neutron separation energy.

JENDL-4.0 level densities used for a given isotope depend on the reaction of interest. Figure 2.4 shows the level density used for ^{239}Pu (a) and ^{241}Pu (b), for neutron induced reactions on different Pu isotopes. For example, the level density of ^{239}Pu is used for the calculation of cross sections for the following reactions: ^{238}Pu(n,γ), ^{239}Pu(n,n'), ^{240}Pu$(n,2n)$, ^{241}Pu$(n,3n)$ and ^{242}Pu$(n,4n)$. The level density of a given isotope is an intrinsic quantity and should not depend on the considered reaction. While the disagreement is small for ^{239}Pu, it is above 25% for ^{241}Pu. The changes in slopes are due to different matching excitation energies. Reliable level densities are required to predict accurate cross sections where experimental data are not available.

2.2 γ-ray emission

When observing γ decay between discrete levels, one can infer branching ratios and the level scheme of a given nucleus. This task becomes practically quite difficult when

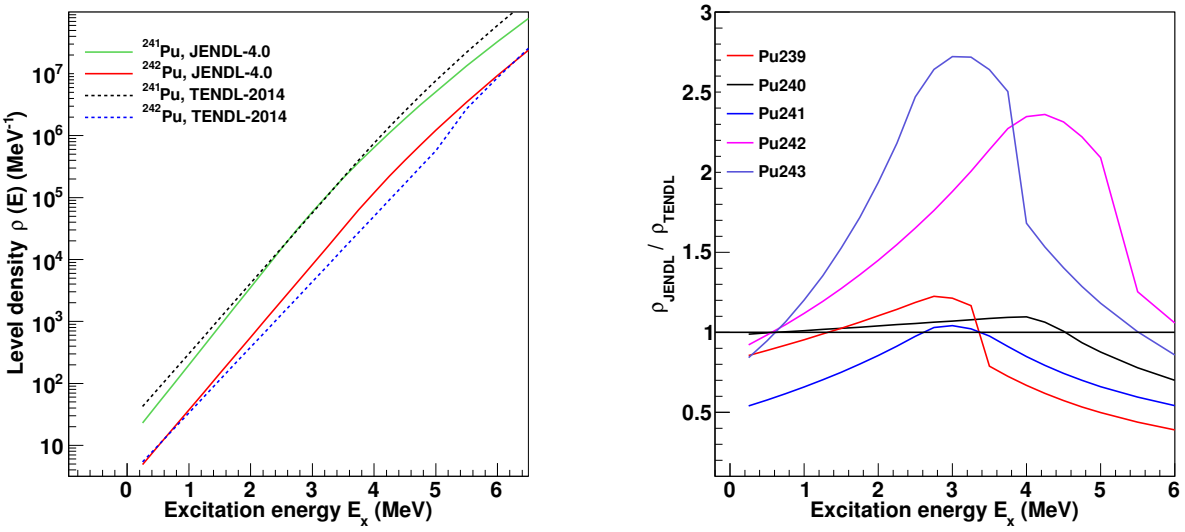

(a) (b)

Figure 2.2: (a) Comparison of the ^{241}Pu and ^{242}Pu level density from JENDL-4.0 and TENDL-2014 [44, 46]. (b) Ratio of the level density from JENDL-4.0 to TENDL-2014 for several Pu isotopes. The discontinuity in the ratio comes from a discontinuity in the TENDL-2014 level density at the matching excitation energy marking the transition from the constant temperature model to the Fermi gas model.

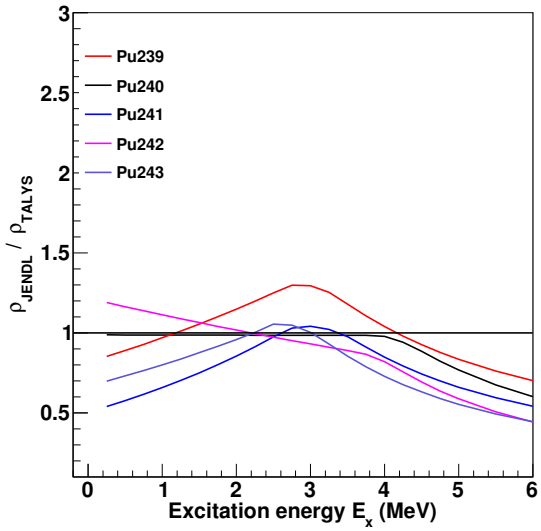

Figure 2.3: Ratio of the level density from ENDF/B-VII.1 (or JENDL-4.0) to the default input for TALYS-1.6 calculations for several Pu isotopes.

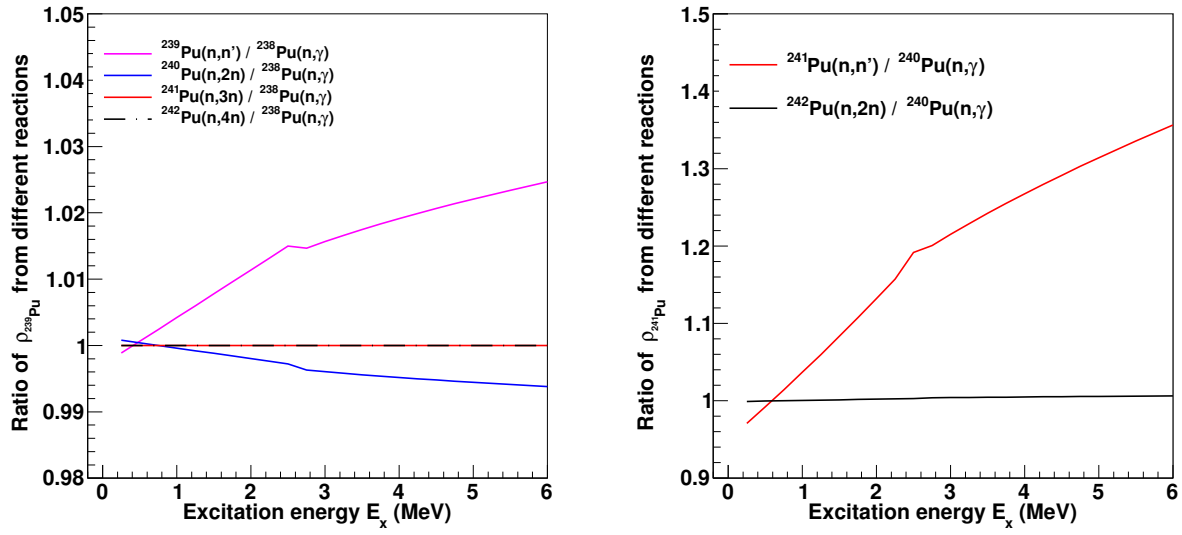

(a) (b)

Figure 2.4: (a) Ratio of the ^{239}Pu level density retrieved from JENDL-4.0 for various reactions. All reactions are compared to the level density used for the calculation of the ^{238}Pu(n,γ) cross section. Some disagreement exists but remains small (below 3%). (b) Ratio of the ^{241}Pu level density retrieved from JENDL-4.0 for various reactions. All reactions are compared to the level density used for the calculation of the ^{240}Pu(n,γ)cross section. The disagreement between the level density used to calculate ^{241}Pu(n,n') and ^{240}Pu(n,γ) is above 25%!

looking at levels in the quasi-continuum, making a description using continuous function referred to as statistical quantities relevant. In this section, γ-ray transition probabilities are introduced, followed by collective excitations. This leads to the γ-ray strength function, describing the average electromagnetic transition properties of the nucleus. Some of the most common macroscopic models used to describe the γ-ray strength function are introduced, as well as an overview of relevant microscopic calculations. Finally, some experimental methods used to extract the γ-ray strength function are presented as well as their implementation in various databases.

2.2.1 γ-ray transition probabilities

Nuclear reactions may leave the nucleus in an excited state. One possible way to de-excite to a more stable form is the emission of a γ ray of energy E_γ. Electromagnetic transitions can be characterized by their type X (i.e electric E, or magnetic M) and their multipolarity L. The magnetic substates are denoted by the variable μ. The transition probability between an initial state i and a final state f, $T^{XL\mu}_{i\to f}$, is given by Fermi's golden rule of time-dependent perturbation theory in the long wavelength limit (for $E_\gamma \lesssim 20$ MeV) [47, 48]:

$$T^{XL\mu}_{i\to f} = \frac{2}{\varepsilon_0 \hbar}\frac{L+1}{L\left[(2L+1)!!\right]^2}\left(\frac{E_\gamma}{\hbar c}\right)^{2L+1}\left|\left\langle \epsilon_f J_f m_f \left| H^{(XL\mu)} \right| \epsilon_i J_i m_i \right\rangle\right|^2, \tag{2.22}$$

where ε_0 is the vacuum permittivity, ϵ_k, J_k and m_k are, respectively, the energy, spin and magnetic substate of the state k, and $H^{(XL\mu)}$ is the nuclear operator associated with the multipole radiation field $XL\mu$. Summing over the magnetic substates, using the Wigner-Eckart theorem [48], the multipole transition rate becomes:

$$T^{XL}_{i\to f} = \frac{2}{\varepsilon_0 \hbar}\frac{L+1}{L\left[(2L+1)!!\right]^2}\left(\frac{E_\gamma}{\hbar c}\right)^{2L+1} B^{XL}_{i\to f}, \tag{2.23}$$

where the reduced transition probability $B^{(XL)}_{i\to f}$ is given by:

$$B^{(XL)}_{i\to f} = \frac{1}{2J_i+1}\left|\left\langle \epsilon_f J_f \left\| H^{(XL)} \right\| \epsilon_i J_i \right\rangle\right|^2. \tag{2.24}$$

One can distinguish between the reduced transition probabilities for excitation ($\epsilon_f > \epsilon_i$), $B^{(XL)}_{i\to f}\uparrow$, and de-excitation ($\epsilon_f < \epsilon_i$), $B^{(XL)}_{i\to f}\downarrow$. Considering two states a and b with $\epsilon_a < \epsilon_b$, the two reduced transition probabilities are proportional by a spin ratio between the two states, according to the principle of detailed balance:

$$B^{(XL)}_{a\to b}\uparrow = \frac{2J_b+1}{2J_a+1} B^{(XL)}_{b\to a}\downarrow. \tag{2.25}$$

2.2.2 Selection rules

The decomposition of an electromagnetic interaction in terms of multipoles allows to characterize γ-ray transitions and simplifies the calculation of the transition matrix elements. Selections rules constrain the possible transitions between two states. The electric and magnetic operators are given by [48]:

$$H^{(EL\mu)} \propto r^L Y_{L\mu}, \qquad H^{(ML\mu)} \propto \left.\begin{matrix} \vec{l} \\ \vec{s} \end{matrix}\right\} \cdot \vec{\nabla}\left(r^L Y_{L\mu}\right), \tag{2.26}$$

where $Y_{L\mu}$ are the spherical harmonics with parity $(-1)^L$, $r^L$is the position scalar with parity $(+1)$, $\vec{l}$ and $\vec{s}$ are respectively the orbital and spin angular momentum vectors, with parity $(+1)$ as axial vectors, and finally the parity of the vector operator $\vec{\nabla}$ is (-1). Therefore, the electric L-pole has a parity $\pi^{EL} = (-1)^L$ and the magnetic L-pole $\pi^{ML} = (-1)^{L+1}$. Considering a transition from an initial state with parity π_i to a final state with parity π_f, the following parity conservation rule has to be followed:

$$\pi_i \pi_f = \begin{cases} (-1)^L & \text{for } EL \\ (-1)^{L+1} & \text{for } ML. \end{cases} \tag{2.27}$$

For a transition between states of angular momenta J_i and J_f, the total angular momentum of the system needs to be conserved, introducing the second selection rule:

$$|J_i - J_f| \leq L \leq J_i + J_f. \tag{2.28}$$

The only exception is the transition $0 \rightarrow 0$ which is forbidden because the spin of a photon is 1. $M0$ transitions are not possible because the magnetic operator described in Equation 2.26 vanishes for $L = 0$. The electric operator is constant for $L = 0$, and therefore cannot connect two different nuclear states. There is no $E0$ single γ-ray transition but $E0$ transitions are possible via internal conversion. In that case, the nucleus de-excites by the ejection of an electron from the atomic nucleus. The double γ decay, which is a second order process of quantum electrodynamics, can connect two $J = 0$ states. It has been observed in ^{16}O, ^{40}Ca and ^{90}Zr with branching ratio on the order of 10^{-4} [49, 50, 51].

Depending on the spins of the initial and final states, several multipolarities might be allowed. For example, a $2^+ \rightarrow 1^+$ transition allows $M1$, $E2$, and $M3$ multipolarities. In this particular example, $M3$ will most likely be without significance because the transition probability decreases drastically with increasing multipolarity. $E2$ and $M1$ transitions are in general competing and mixing has to be taken into account.

2.2.3 Collective excitations

Giant resonances

Giant resonances are collective excitations involving all nucleons. The Giant Electric Dipole Resonance (GEDR) was first discovered by Baldwin and Klaiber in 1947 [52] by

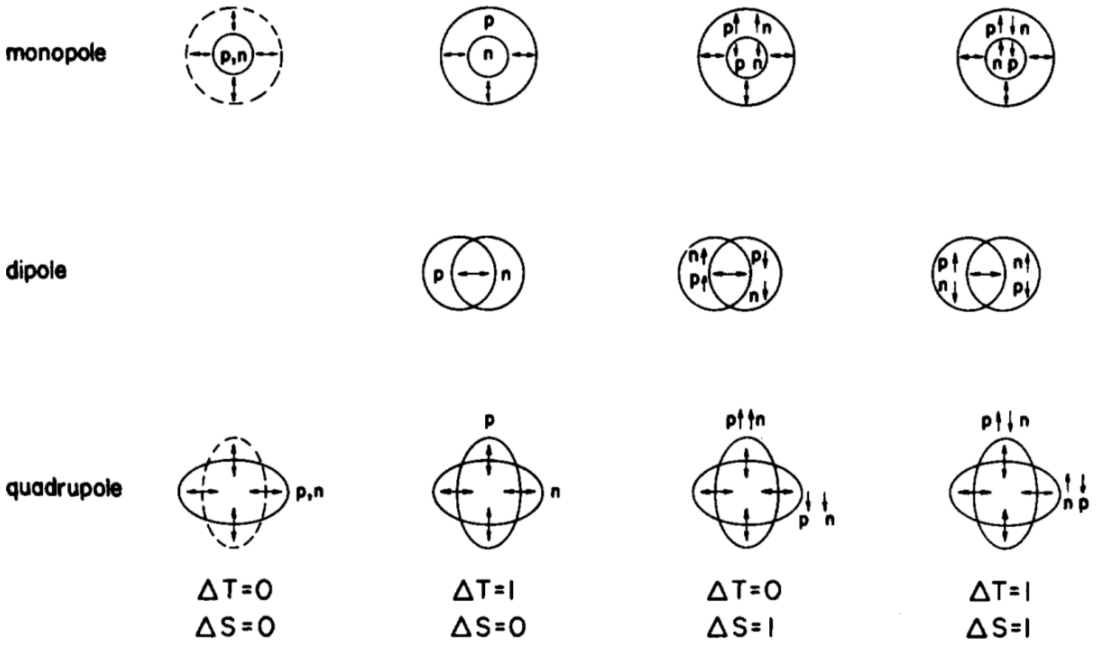

Figure 2.5: Macroscopic picture of the different giant resonances for L=0 (monopole), L=1 (dipole) and L=2 (quadrupole) modes as well as their electric ($\Delta S = 0$) or magnetic ($\Delta S = 1$) character and their isoscalar ($\Delta T = 0$) or isovector ($\Delta T = 1$) character. Schematic taken from Ref. [54].

measuring the photo-fission cross section in actinides. A resonance-like behavior of the cross section is seen and is a general feature of all nuclei in the $E_\gamma = 10 - 20$ MeV energy region. Giant resonances can be classified by their multipolarity and their character (isoscalar or isovector). In the macroscopic picture, the isoscalar character ($\Delta T = 0$) corresponds to protons and neutrons oscillating in phase, while the isovector character ($\Delta T = 1$) corresponds to neutrons oscillating against the protons. Giant magnetic resonances differ from the electric ones by having a spin flip ($\Delta S = 1$). Figure 2.5 shows schematics for the different possible giant resonances. The strongest resonance is the isovector giant electric dipole resonance (IVGEDR) whose macroscopic picture corresponds to neutrons oscillating against protons. A comprehensive review on giant resonances, experimental methods as well as theoretical description can be found in Refs. [53, 54].

Pygmy dipole resonances

The macroscopic picture of the IVGEDR is the oscillations of all protons against all neutrons. Inspired from the discovery of halo nuclei, Suzuki *et al.* [55] described the pygmy dipole resonance in neutron (proton) rich nuclei as a core nucleus and the excess neutrons (protons) vibrating against the core. The energy centroid of the resonance and its magnitude are smaller than the GDR since the restoring force will depend on the

number of excess neutrons (protons). A review on the pygmy dipole resonance can be found in Ref. [13].

Scissors resonances

The scissors resonance is a $M1$ resonance expected at low energy in deformed nuclei. It has been measured in rare-earth nuclei [7], and more recently in actinides [8, 56]. This resonance is generally viewed as the neutrons oscillating against the protons in a scissors-like motion (see Figure 2.6). However, a recent review concluded that the scissors resonance is mostly due to single particle transition and is only weakly collective [57]. Recent microscopic calculations suggest that the scissors resonance is both due to the orbital scissors mode (counter rotation of protons against neutrons) and the spin scissors mode (oscillations of spin-up nucleons against spin-down nucleons) [58].

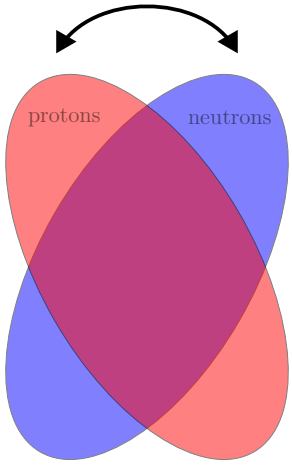

Figure 2.6: Macroscopic picture of the scissors resonance. In deformed nuclei, the proton core oscillates against the neutron core in a scissor-like motion.

Resonance strength calculation using the sum rule approach

One possible way to theoretically calculate the strength of a resonance is to use the sum rule approach detailed in Ref. [59]. Considering an operator F exciting the nucleus from its ground state $|0\rangle$ to an excited state $|k\rangle$ of the nuclear Hamiltonian H. The strength function, $S(\omega)$, characterizing the action of the operator F on the nuclear ground state is given by:

$$S(\omega) = \sum_k |\langle k\,|F|\,0\rangle|^2\,\delta(\omega - \omega_k), \tag{2.29}$$

where ω_k is the excitation energy of the eigenstates $|k\rangle$. In this form, the calculation of the strength requires also the calculation of the eigenstates $|k\rangle$. In the sum rule approach,

the completeness relation is used to calculate the moment of order p, m_p of the strength function,

$$m_p = \int_0^\infty S(\omega)\omega^p \mathrm{d}\omega, \tag{2.30}$$

as mean values of the ground state. If the operator F fulfills the relation $\langle 0\,|F|\,0\rangle = 0$, for any $p \geq 0$, the moments fulfill the relation:

$$m_p = \left\langle 0 \left| F^\dagger (H - E_0)^p F \right| 0 \right\rangle, \tag{2.31}$$

where E_0 is the ground state energy. In the presence of resonant phenomena, a few moments are able to characterize the strength function [59]. The isovector rotational motion associated with the $M1$ scissors resonance can be defined by the operator [60]:

$$\mathfrak{M}_{1,SR} \propto \sum_i \mathcal{T}_i^x \hat{\tau}_i^3, \tag{2.32}$$

where the angular momentum operator perpendicular to the symmetry axis is given by $\mathcal{T}^x$, and the isospin projection is denoted by $\hat{\tau}^3$. Because $\mathfrak{M}_{1,SR}$ is an Hermitian operator, the moments for $p = 1$ and $p = -1$ can be written as the following commutation relations:

$$m_1 = \left\langle 0 \left| \mathfrak{M}_{1,SR}^\dagger (H - E_0)^1 \mathfrak{M}_{1,SR} \right| 0 \right\rangle = \frac{1}{2} \left\langle 0 \left| [\mathfrak{M}_{1,SR}, [H, \mathfrak{M}_{1,SR}]] \right| 0 \right\rangle, \tag{2.33}$$

$$m_{-1} = \left\langle 0 \left| \mathfrak{M}_{1,SR}^\dagger (H - E_0)^{-1} \mathfrak{M}_{1,SR} \right| 0 \right\rangle = \frac{1}{2} \left\langle 0 \left| \left[\left[X^\dagger, H \right], X \right] \right| 0 \right\rangle, \tag{2.34}$$

where the operator X is solution of the equation:

$$[H, X] = \mathfrak{M}_{1,SR}. \tag{2.35}$$

Using the Breit-Wigner distribution to describe the energy dependence of the resonance cross section, $\sigma(\omega)$, the strength of the resonance, $S(\omega)$, is given by:

$$\sigma(\omega) = A\omega S(\omega) = \frac{\sigma_0 \omega^2 \Gamma^2}{(\omega^2 - \omega_c^2)^2 + \omega^2 \Gamma^2}, \tag{2.36}$$

where A is a constant, σ_0 is the cross section maximum at the resonance centroid energy ω_c, and Γ is the width of the resonance. With the assumption that $\omega_c \gg \Gamma$, the m_1 and m_{-1} moments become:

$$m_1 = \int_0^\infty S(\omega)\omega \mathrm{d}\omega = \frac{\sigma_0 \Gamma \pi}{\mathrm{A}}, \tag{2.37}$$

$$m_{-1} = \int_0^\infty \frac{S(\omega)}{\omega} \mathrm{d}\omega = \frac{\sigma_0 \Gamma \pi}{\mathrm{A}\omega_\mathrm{c}^2}, \tag{2.38}$$

and the integrated strength is:

$$\int_0^\infty S(\omega)\mathrm{d}\omega = \frac{\sigma_0 \Gamma \pi}{\mathrm{A}\omega_\mathrm{c}}. \tag{2.39}$$

Combining Equations (2.37,2.38), the resonance centroid and strength can be extracted:

$$\omega_c = \sqrt{\frac{m_1}{m_{-1}}}, \tag{2.40}$$

$$S(\omega) = \sqrt{m_1 m_{-1}}. \tag{2.41}$$

Theoretical calculation of Equations (2.33,2.34) for the scissors resonance, using a Skyrme-type Hamiltonian allows to express the moments in terms of observables [59, 60]:

$$m_1 = \frac{3}{20\pi} r_0^2 A^{5/3} \delta^2 \omega_D^2 m_N (g_p - g_n)^2 \xi \quad \left[\mu_N^2 MeV\right], \tag{2.42}$$

$$m_{-1} = \frac{3}{16\pi} \Theta_{IV} (g_p - g_n)^2 \quad \left[\mu_N^2 MeV^{-1}\right], \tag{2.43}$$

where r_0 is the nuclear radius, A is the mass number, δ is the ground state deformation parameter, ω_D is the centroid of the IVGDR, m_N is the nucleon mass, g_p and g_n are the orbital gyromagnetic ratios of the deformed neutrons and protons valence bodies, Θ_{IV} is the moment of inertia from the isovector motion, and ξ represents the contribution from the IVGQR of centroid ω_Q:

$$\xi = \frac{\omega_Q^2}{\omega_Q^2 + \omega_D^2}. \tag{2.44}$$

2.2.4 γ-ray strength function

The γ-ray strength function, f_{XL}, (also called radiative strength function or photon strength function in the literature), was first introduced by Bartholomew [61] to describe neutron capture data. The de-excitation process depends on the average width of the states $\langle \Gamma_{XL} \rangle$ and the resonance spacing parameter D_{XL} for a type X photon of multipolarity L and energy E_γ:

$$f_{XL} = \frac{\langle \Gamma_{XL} \rangle}{E_\gamma^{2L+1} D_{XL}}. \tag{2.45}$$

While initially considered to describe γ decay following neutron capture, two γ-ray strength functions can be considered, the "downward" strength function, $\overleftarrow{f}$, related to the emission of γ-rays by the nucleus during de-excitation, and the "upward" strength function, $\overrightarrow{f}$, related to the absorption of γ-rays by the nucleus. The excitation process depends on the photo-absorption cross section $\langle \sigma_{XL}(E_\gamma) \rangle$ and is given by:

$$\overrightarrow{f_{XL}} = \frac{1}{(\pi\hbar c)^2 (2L+1)} \frac{\langle \sigma_{XL} \rangle}{E_\gamma^{2L+1}}. \tag{2.46}$$

To calculate the competition between the γ-ray emission and other reaction channels (such as particle emission, fission, etc...), transmission coefficients are used as input to Hauser-Feshbach calculations. The γ-ray emission transmission coefficient, $T_{XL}(E_\gamma)$, for a type X photon of multipolarity L and energy E_γ is given by:

$$T_{XL}(E_\gamma) = 2\pi \overleftarrow{f_{XL}}(E_\gamma) E_\gamma^{2l+1}. \tag{2.47}$$

2.2.5 The generalized Brink-Axel hypothesis

In 1955, D.M. Brink suggested in his Ph.D thesis [42] that the cross section for photoabsorption has the same transition energy dependence if the absorption happens on the ground state or an excited state. In addition, P. Axel made the assumption that as long as the dipole selection rule is fulfilled, there is no dependence on the spin value of the initial and final state [43]. As a result of the Brink-Axel hypothesis, the upward and downward strengths are equal: $\overleftarrow{f_{XL}}(E_\gamma) = \overrightarrow{f_{XL}}(E_\gamma)$. Despite the strong assumptions of Brink and Axel, this hypothesis is frequently used to calculate E1 and M1 strength functions. This hypothesis has also been used for β decay and electron capture to calculate Gamov-Teller and Fermi transitions strength [62]. Some experimental and theoretical calculations support the Brink-Axel hypothesis [63, 64]. Other experimental work and theoretical calculations reveal deviation from the hypothesis [65, 66]. Under which conditions is the Brink-Axel hypothesis valid remains an open question.

2.2.6 γ-ray strength function models

Several parametrizations of the γ-ray strength function are available in the literature. Only the most used models are given here, describing the collective excitation modes with Lorentzian-like functions. The $E1$ strength function is the main focus of the following. While the following models only describe single isolated resonances, the total γ-ray strength function is generally described as a sum of multiple resonances with different centroids and total strength.

The Standard Lorentzian model (SLO)

This is the model implementing the Brink-Axel hypothesis and is widely used to describe the GEDR strength. The strength is only dependent of the γ-ray energy, E_γ:

$$f_{E1}^{SLO}(E_\gamma) = \frac{1}{(\pi\hbar c)^2}\frac{\sigma_0 E_\gamma \Gamma_0^2}{(E_\gamma^2 - E_0^2)^2 + E_\gamma^2\Gamma_0^2}, \tag{2.48}$$

where σ_0, Γ_0 and E_0 are, respectively, the cross section, width and energy centroid of the resonance. Parameters derived from experimental data are available for 121 nuclides in RIPL-3 [25]. This mathematical function describes properly photo-nuclear data for $A > 50$ [67, 68]. However, γ-ray emission is underestimated for $E_\gamma < 2$ MeV [25] and experimental data around the neutron separation energy, such as neutron capture cross sections and the average radiative widths of heavy nuclei are overestimated [69, 70, 71, 72].

Another formulation adding an energy dependence of the resonance width has been suggested [73]:

$$f_{E1}(E_\gamma) = \frac{1}{(\pi\hbar c)^2}\frac{\sigma_0 E_\gamma \Gamma_0 \Gamma_K(E_\gamma, T)}{(E_\gamma^2 - E_0^2)^2 + E_\gamma^2\Gamma_K(E_\gamma, T)^2}, \tag{2.49}$$

where Γ_K is the energy dependent resonance width. Based on the Fermi liquid theory, it is dependent on both the γ-ray energy and the temperature of the state on which the giant resonance is built on [71]:

$$\Gamma_K(E_\gamma, T) = \Gamma_0 \frac{E_\gamma^2 + 4\pi^2 T^2}{E_0^2}, \tag{2.50}$$

where T is the nuclear temperature of the final state. This formulation slightly breaks the Brink-Axel hypothesis because of the dependence on the nuclear temperature. Good agreement is also found with proton or heavy-ion capture experiments [71].

The Generalized Lorentzian model (GLO)

The generalized Lorentzian model was first proposed by Kopecky and Chrien [74], and consists of a Lorentzian term with energy and temperature dependent width and a term corresponding to the temperature dependent width for $E_\gamma = 0$:

$$f_{E1}^{GLO} = \frac{\sigma_0 \Gamma_0}{(\pi\hbar c)^2} \left[\frac{E_\gamma \Gamma_K(E_\gamma, T)}{(E_\gamma^2 - E_0^2)^2 + E_\gamma^2 \Gamma_K(E_\gamma, T)^2} + 0.7 \frac{\Gamma_K(E_\gamma = 0, T)}{E_0^3} \right], \tag{2.51}$$

where Γ_K is given by Equation (2.50). It is the model of choice for spherical nuclei. This model provides a good description of average resonance capture data (ARC), neutron capture cross sections and γ-ray production [71].

The Enhanced Generalized Lorentzian model (EGLO)

Both the SLO and GLO models fail to reproduce γ-ray strength function data over the whole mass region. The more flexible EGLO model was introduced to reproduce experimental data for strongly deformed nuclei, the energy and temperature dependent width parametrization is modified:

$$\Gamma_K^{EGLO}(E_\gamma, T) = \left[k_0 + (1 - k_0) \frac{E_\gamma - \epsilon_0}{E_0 - \epsilon_0} \right] \Gamma_K(E_\gamma, T), \tag{2.52}$$

where the enhancement parameter k_0 is used to reproduce experimental data at the reference energy ϵ_0. For $k_0 = 1$, $\Gamma_K^{EGLO}(E_\gamma, T) = \Gamma_K(E_\gamma, T)$. A possible parametrization given in Ref. [75] uses $\epsilon_0 = 4.5$ MeV and:

$$k_0 = \begin{cases} 1 & \text{for A} < 148 \\ 1 + 0.09(A - 148)^2 \exp\left[-0.18(A - 148)\right] & \text{for A} \geqslant 148 \end{cases}. \tag{2.53}$$

The Modified Lorentzian model (MLO)

All the models above are usually based on parametrizations of experimental data. The shapes of the temperature dependent models (all except SLO) are in contradiction with microscopic theoretical studies [76, 77, 78]. The modified Lorentzian model has been suggested to take into account theoretical studies, and is based on general relations between the γ-ray strength function and the imaginary part of the nuclear response function to the electromagnetic field [25]. It is given by:

$$f_{E1}^{MLO}(E_\gamma) = \frac{\Lambda(E_\gamma, T_f)\sigma_0\Gamma_0}{(\pi\hbar c)^2} \frac{E_\gamma \Gamma_K(E_\gamma, T_f)}{(E_\gamma^2 - E_0^2)^2 + E_\gamma^2 \Gamma_K(E_\gamma, T_f)^2}, \tag{2.54}$$

where T_f is the nuclear temperature of the final state, and a scaling factor $\Lambda(E_\gamma, T_f)$ is introduced, given by:

$$\Lambda(E_\gamma, T_f) = \frac{1}{1 - \exp(1 - E_\gamma/T_f)}. \tag{2.55}$$

This scaling factor determines the enhancement of the γ-ray strength function as a function of the nuclear temperature. Different semi-empirical expression are available for the energy and temperature dependent width [25].

Other macroscopic models

More macroscopic models and variations of the presented ones exists. Some of them can be found in Ref. [25]. Most consist in different formulation of the scaling factor, Λ, or the γ-ray energy and temperature dependent width, Γ_K. In TALYS [26], $E1$ resonances are modeled by default using the GLO model while all other resonance types and multipolarities are modeled using SLO. SLO and MLO parameters for a large number of nuclei are available in the RIPL-3 database [25].

In Figure 2.7 is shown a comparison of the SLO, GLO, EGLO and MLO models for ^{239}Pu and measured (γ, x) data from Gurevich [79]. Parameters for the SLO model are taken from Ref. [79]. The same parameters are taken for the GLO and EGLO calculations. Parameters for the MLO model are taken from RIPL-3 [25]. Because ^{239}Pu is a deformed nucleus, the GEDR is split in two components characterizing the proton-neutron oscillations along the two symmetry axis of the deformed nucleus. The agreement between the different models is good close the centroid energies of the GEDR. The deviation between the GLO, EGLO and MLO models is relatively small for a large energy range, even though there is significant deviation of the MLO model at low energies. The SLO model shows significant deviation from the other models and measured data for $E_\gamma < 10$ MeV.

Microscopic calculations

Despite the good fit of the GEDR and possible empirical determination of the strength, centroid and width of the GEDR, a microscopic calculation of the γ-ray strength function

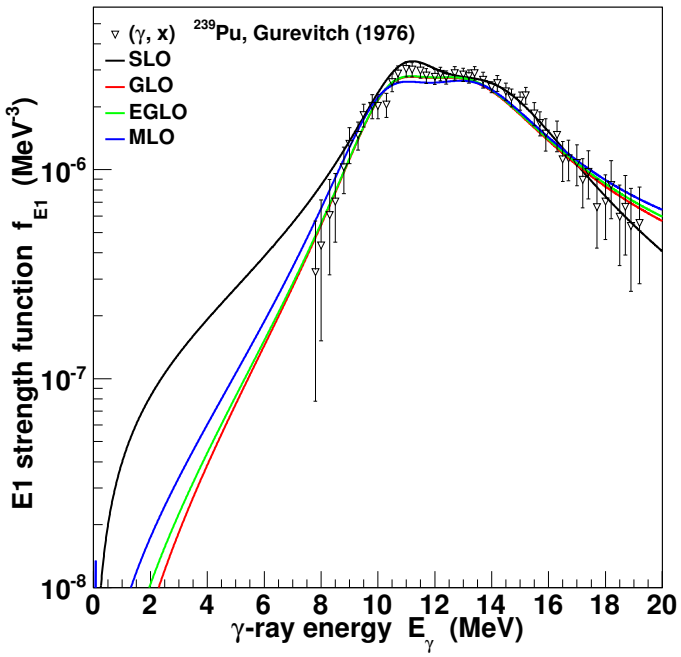

Figure 2.7: Comparison of the SLO, GLO, EGLO and MLO models to experimental data from Ref. [79] for ^{239}Pu.

is necessary in order to understand the underlying nuclear structure, predict strength function for exotic nuclei and possible low-energy enhancements.

Large scale QRPA calculations of the $E1$ strength were performed by Goriely and Khan for over 8000 nuclei with $8 \leqslant Z \leqslant 110$ [80]. The results are in good agreement with available experimental data, in particular at low energies. Theoretical predictions are available at http://www.astro.ulb.ac.be. Figure 2.8 shows the calculated $E1$ strengths for several Sn isotopes. It can be observed that the shape of the γ-ray strength function becomes increasingly more complicated with the number of excess neutrons and more low-energy strength is present. Small variations in the low energy region of the γ-ray strength function can have a big impact on the neutron capture cross sections calculated using the Hauser-Feshbach formalism.

Recently, theoretical calculations focused on the low lying strength and its origins. In Ref. [81], realistic potentials derived from nucleon-nucleon forces are used to generate Hartree-Fock-Bogoliubov basis of states. The dipole response is calculated using the Quasi-particle Tamm-Dancoff and Quasi-particle Random-Phase Approximation approaches [48]. The description of the dipole response is improved but discrepancies between the theory and the experiments subsist, which is currently filled by adding a phenomenological density dependent repulsive term to the potential.

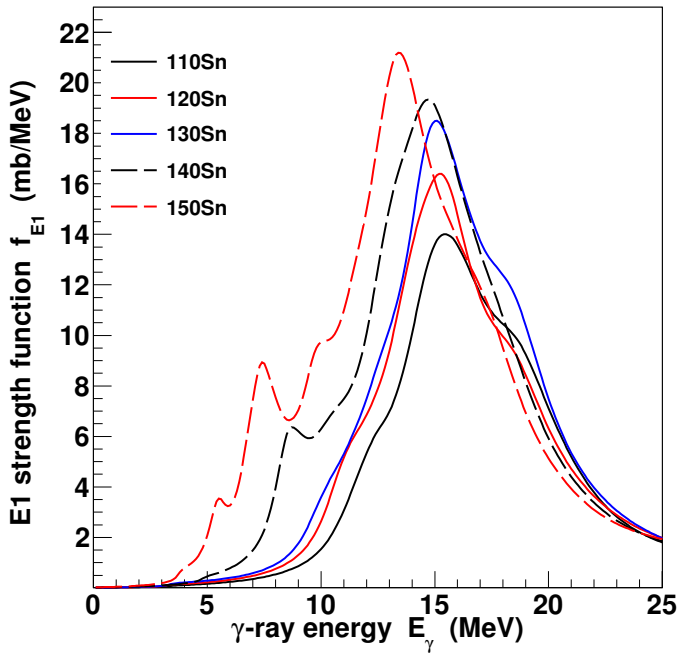

Figure 2.8: Microscopic calculation of $E1$ γ-ray strength function for several Sn isotopes by Goriely and Khan [80].

2.2.7 Experimental methods to extract the γ-ray strength function

Photonuclear reactions

The photoexcitation strength function, $\overrightarrow{f}$, can be extracted by measuring the average photon absorption cross section using Eq. (2.46). For energies higher than a few hundred keV above the neutron separation energy, the particle emission mechanism dominates over the γ-ray emission mechanism [69]. The absorption cross section is then assumed to be equal to the sum of the different particle emission cross sections and the fission cross section for fissionable nuclei. Measurements using broad bremsstrahlung beam are possible but require a differential analysis to extract the average particle emission cross section [82].

Quasi-monoenergetic photon beams with 100-200keV energy spread are achieved using in-flight positron annihilation [67]. The photons are created by electron-positron annihilation occurring when a beam of fast positrons interacts with a thin low-Z target. The energy spread of the photon beam depends on the thickness of the low-Z target and the momentum spread of the positron beam. This technique enables measurements of the strength function across the nuclear chart in the GEDR energy region. RIPL-3 recommended parameters for the GEDR are given according to those measurements.

Below the neutron separation energy and the fission threshold, the total absorption cross section, $\langle\sigma_{\gamma,\mathrm{abs}}\rangle$, is given by:

$$\langle\sigma_{\gamma,\mathrm{abs}}\rangle = \langle\sigma_{\gamma,\gamma}\rangle + \sum_{\gamma'}\langle\sigma_{\gamma,\gamma'}\rangle\,, \tag{2.56}$$

where $\langle\sigma_{\gamma,\gamma}\rangle$ is the photoelastic scattering cross section and the summation of photoinelastic cross sections $\sum_{\gamma'}\langle\sigma_{\gamma,\gamma'}\rangle$. Direct measurement of the inelastic contribution is a hard task and is generally replaced by an estimate of the ground state branching ratio. The average elastic scattering cross section can be measured using a bremsstrahlung monochromator [83, 84]. Rough values of the strength function can be extracted by estimating the inelastic cross section.

Nuclear resonance fluorescence measurements use high energy resolution detector, like High-purity germanium detectors, to measure discrete states populated by photoexcitation. If the interrogating photon beam is linearly polarized, angular distribution of emitted photons will allow extraction of the spin and parity of the measured levels. In practice, only γ rays from the de-excitation from the populated state to the first excited state and ground state are seen. Thus a common approximation is to only consider the branching ratio to the ground state and to the first excited state. Photoexcitation is very selective and only one to two units of angular momentum are transferred. Weak transitions cannot be seen and this method is not reliable to extract the total γ-ray strength function but gives a lower limit.

Radiative capture

In Ref. [85], the primary γ rays following neutron capture in ^{156}Gd have been measured for two neutron beam energies (2 keV and 24 keV). Relative intensities of the γ rays are extracted and are used to calculate the γ-ray strength function. The 2 keV beam was used to extract the strength function while the 24 keV beam was used to resolve $E1$ transitions from $M1$ and $E2$ transitions.

Improvement of this method leads to the Two Step Cascade method[72]. The γ rays are measured in coincidence following neutron capture. The method consists of looking for two coincident γ rays whose energies sum up to the energy difference between the capturing state and a low-lying state. The obtained γ spectra are fitted with trial γ-ray strength functions. The level density is assumed and therefore remains a large source of systematic uncertainty. This method allows to separate between the different transition types and multipolarities. This method is often not able to give a unique solution. Recently, the method has been applied to proton capture data [86]. The use of protons offers better precision on the Two Step Cascade intensities and because proton capture undergoes less Porter-Thomas fluctuations, therefore the range of possible γ-ray strength functions is reduced.

The Oslo method

In the Oslo method, particle-γ coincidences are recorded. Presently, measurements have been realized detecting protons, deuterons, tritons, helions, and α particles. The primary γ-ray spectra are extracted as a function of the excitation energy [3, 4]. The level density and the γ-ray strength function are simultaneously extracted below the particle emission threshold [5]. This method does provide the shape of the γ-ray strength function, but not its absolute values. It is normalized to the average total radiative neutron resonance width. Very good agreement has been observed with the extrapolation of the γ-ray strength function extracted from photonuclear reactions.

Recently, the Oslo method has been adapted to unstable neutron rich isotopes. The nuclei are populated by β decay with a high Q-value. This method is called β-Oslo in the literature [87].

2.2.8 γ-ray strength function in databases

As for the level density, JENDL-4.0[44] databases use the CCONE code[45] to calculate cross sections, and TENDL-2014 [46] uses the TALYS code [26]. In the two databases, the EGLO model is used to describe the $E1$ strength, and the SLO model is used to describe the $M1$ and $E2$ strengths. Parameters used by JENDL-4.0 are given in the interpreted ENDF file. TALYS uses by default the EGLO parameters from RIPL-3 [25]. When no parameters are available in RIPL-3, empirical formulas are used to calculate the EGLO parameters. Empirical formulas are also used to calculate SLO parameters for the $M1$ and $E2$ resonances. Figure 2.9 shows the γ-ray strength functions used to calculate neutron capture cross section by JENDL-4.0, and TENDL2014 for ^{238}Pu$(n,\gamma)^{239}$Pu (a) and ^{242}Pu$(n,\gamma)^{243}$Pu (b). For ^{239}Pu, the $E1$ and $M1$ contributions of the JENDL-4.0 strength function are shown along with measured photonuclear data [79]. JENDL-4.0 is reproducing the measured data. The discrepancy between JENDL-4.0, and TENDL2014 is rather significant at low energies. In TENDL2014, the γ-ray strength function shown is multiplied by a constant factor in order to reproduced the average radiative capture width. Results of QRPA calculations of the $E1$ strength by Goriely do not reproduce well GEDR measured data. For ^{243}Pu, no GEDR parameters are available in RIPL-3. The GEDR strength is calculated using an empirical formula for spherical nuclei, therefore only one Lorentzian is used to describe the GEDR.

2.3 The Hauser-Feshbach formalism

The Hauser-Feshbach formalism is based on the compound nucleus picture based on Bohr's independence hypothesis [88]. It states that the decay of the compound nucleus is independent of its formation. The formalism was developed initially for neutron induced reaction [89], but is applicable for all nuclear reactions forming a compound nucleus. The idea is that because of the large number of states in the quasi-continuum and continuum

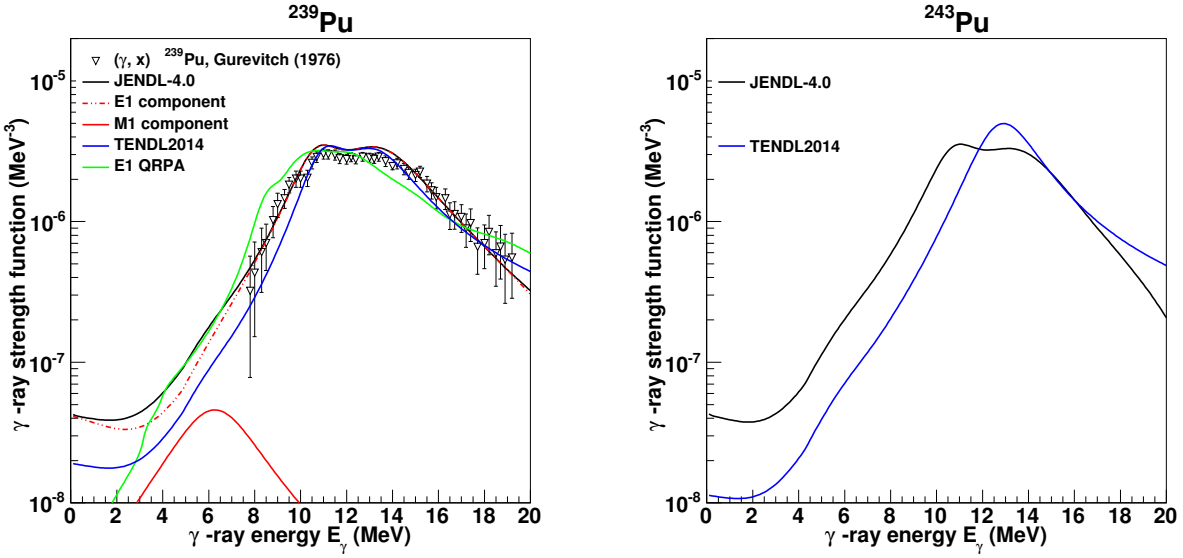

(a) (b)

Figure 2.9: (a) Comparison between the γ-ray strength function used by JENDL-4.0 (black line) and TENDL2014 (blue line) and measured data by Gurevitch (open triangles) for ^{239}Pu. The $E1$ (dashed red curve) and $M1$(continuous red curve) for the JENDL-4.0 γ-ray strength function is also shown along with QRPA calculation of the $E1$ component by Goriely. (b) Comparison between the γ-ray strength function used by JENDL-4.0 (black line) and TENDL2014 (blue line) for ^{243}Pu. Empirical calculation of the GEDR resonance parameter is done for the TENDL2014 evaluation (for a spherical nucleus!) since evaluated data are absent from RIPL-3.

regions of the excitation energy, statistical averages over the resonances can be used instead of treating each resonance separately. A quick demonstration of the Hauser-Feshbach cross section is given here.

Applying Bohr's independence hypothesis, if we consider a compound nucleus formed via the entrance channel α which subsequently decays via the exit channel β, the reaction cross section, $\sigma_{\alpha,\beta}$, can be written as:

$$\sigma_{\alpha,\beta} = \sigma_\alpha P_\beta, \tag{2.57}$$

where σ_α is the cross section for forming the compound nucleus though the entrance channel α and P_β is the decay probability of the compound nucleus through the exit channel β. Each reaction channel is characterized by the particles and the quantum numbers involved. Considering all possible decay channels, the sum over all decay probabilities has to be unity:

$$\sum_\beta P_\beta = 1. \tag{2.58}$$

Using time-reversal symmetry, we can write:

$$k_\alpha^2 \sigma_{\alpha,\beta} = k_\beta^2 \sigma_{\beta,\alpha}, \tag{2.59}$$

where k_i is the wave number for the entrance channel i. Combining Eq. (2.57) and Eq. (2.59), we obtain:

$$\frac{k_\alpha^2 \sigma_\alpha}{P_\alpha} = \frac{k_\beta^2 \sigma_\beta}{P_\beta}. \tag{2.60}$$

Because α and β are independent channels, both sides of Eq. (2.60) must be equal to a channel independent constant Λ:

$$\text{For all } \iota \quad \frac{k_\iota^2 \sigma_\iota}{P_\iota} = \Lambda. \tag{2.61}$$

Combining Eqs. (2.57), (2.58) and (2.61), we obtain the Hauser-Feshbach formula:

$$\sigma_{\alpha,\beta} = k_\beta^2 \frac{\sigma_\alpha \sigma_\beta}{\sum_\iota k_\iota^2 \sigma_\iota}, \tag{2.62}$$

where the sum is carried over all possible exit channels.

The cross section for the scattering of a particle α on a potential barrier, σ_α, can be decomposed in terms of partial waves of orbital angular momentum l:

$$\sigma_\alpha = \frac{\pi}{k_\alpha^2} \sum_l (2l+1) T_\alpha^{(l)} = \frac{\pi}{k_\alpha^2} T_\alpha, \tag{2.63}$$

where $T_\alpha^{(l)}$ is the transmission coefficient of the l^{th} partial wave for the channel α, and T_α the transmission coefficient for the channel α summed over all spins. These coefficients

give the probability of penetrating the potential barrier. Inserting Eq. (2.63) in Eq. (2.62), we obtain:

$$\sigma_{\alpha,\beta} = \frac{\pi}{k_\alpha^2} \frac{T_\alpha T_\beta}{\sum_\iota T_\iota}. \tag{2.64}$$

The given formula doesn't take into account the total angular momentum J and parity Π. The complete Hauser-Feshbach formula which conserves angular momentum and parity is given by [90]:

$$\sigma_{\alpha,\beta}(E_x) = \frac{\pi}{k_\alpha^2} \sum_{J,\Pi} \frac{2J+1}{(2J_\alpha+1)(2J_\beta+1)} \frac{T_\alpha(E_x,J,\Pi) T_\beta(E_x,J,\Pi)}{\sum_\iota T_\iota(E_x,J,\Pi)}, \tag{2.65}$$

where E_x is the excitation energy of the compound nucleus.

The Hauser-Feshbach formalism, via Eq. (2.65), is a powerful tool to describe reaction cross section if a compound nucleus is created. The main difficulty resides in the evaluation of the transmission coefficients. Level densities are required to estimate the transmission coefficient for the formation of the compound nucleus while γ-ray strength functions are important for the description of the γ-ray emission channel. Measurement of those two quantities for ^{243}Pu are presented in this work. Finally, the optical model, describing the interaction between the incident particle and a mean field potential representing the nucleus, plays an important role in the cross section calculation. No parameters of the optical model are extracted in this work.

Chapter 3

The ^{242}Pu experiment

This chapter presents the experimental setup used to measure the nuclear reaction $(d, p\gamma)$ on a thin ^{242}Pu target. First are given details about the facility and the target fabrication, followed by details on the detection systems used to detect the outgoing protons, γ rays and fission products. Then, the calibration of the detectors is presented as well as corrections for the leading edge discrimination used to trigger the electronic acquisition chain. A gate on proton events as well as a time gate on γ rays coincident with the protons are set to extract the distribution of measured γ rays as function of the excitation energy of ^{243}Pu, which will be used as the starting point for the Oslo method presented in Chapter 4.

3.1 Introduction

The experiment was performed at the Oslo Cyclotron Laboratory (OCL) at the University of Oslo, Norway, in June 2014. The MC-35 Scanditronix cyclotron used was installed in 1979 and has been operating since then, delivering pulsed light ion beams (^{1}H$^+$, ^{2}H$^+$, ^{3}He^{2+}, ^{4}He^{2+}). A ^{242}Pu target (≈ 0.4 mg/cm^2), mounted on a ^{9}Be backing (1.8 mg/cm^2), was bombarded with a ≈ 1 nA, 12 MeV deuteron beam.

Prior to electrodeposition, the Pu material was cleaned from decay products and other impurities using an anion-exchange resin column procedure [91]. The purified product was electroplated onto a thin Be foil (1.8 mg/cm^2 thickness) from a small aliquot of dilute nitric acid placed into a large volume of isopropanol. The resulting target was dried, baked at 500 °C in a muffle furnace, then glued to the Aluminum target frame. Passive spectroscopy was used to quantify radioactive impurities in the target. Table 3.1 gives the number of atoms of ^{242}Pu and impurities detected by the passive spectroscopy. The number of ^{242}Pu nuclei is at least four orders of magnitude greater than any other isotopes detectable using passive spectroscopy.

Table 3.1: Target composition obtained by passive spectroscopy.

Nuclide	Number of atoms	Uncertainty (%)
^{237}U	2.20×10^{6}	14.1
^{238}Pu	3.52×10^{13}	9.5
^{241}Pu	6.85×10^{13}	32.7
^{242}Pu	1.53×10^{18}	2.7
^{241}Am	1.49×10^{11}	6.5

3.2 Experimental setup

Figure 3.1, shows an illustration of the experimental setup. The ^{242}Pu target is placed in the beam using the target ladder at the center of the CACTUS array, which is used to measure γ rays. The beam goes first through the Be backing and then through the ^{242}Pu layer. The silicon detector array SiRi is used to measure light outgoing particles (in our case protons, deuterons and tritons), and the NIFF detector to detect fission products. Both SiRi and NIFF are not drawn to scale.

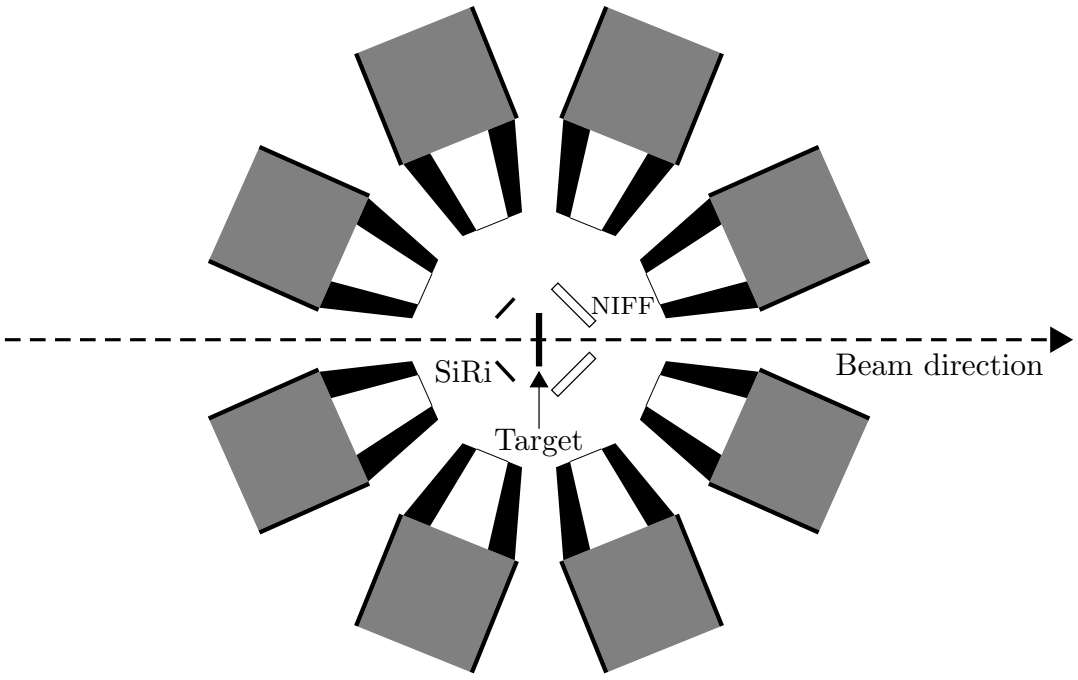

Figure 3.1: Detection setup. The NaI crystals (gray squares) are surrounded by a 3 mm lateral lead shielding. Each detector is collimated with a 10 cm conical lead collimator (black cones). The target is surrounded by the particle telescope array SiRi and the fission fragment array NIFF (not to scale).

3.2.1 The CACTUS array

The CACTUS array [92, 93], shown in Figure 3.2, is composed of 28 5" × 5" NaI detectors mounted on a 25 cm radius spherical frame surrounding the target. The NaI crystals are doped with Tl (NaI(Tl)). Two detectors were not used in order to make room for the fission detector NIFF. The distance between the target and the face of the NaI detectors is 22 cm. Each NaI detector is collimated with a 10 cm conical lead collimator. A 3 mm lateral lead shielding is present around the crystals to reduce the probability of having a given γ ray interact in more than one detector. X-rays are suppress with a 2 mm Cu plate positioned on the face of the detectors.

The total solid angle covered by the 26 collimated NaI scintillators is 16.4 % of 4π. The total efficiency is 14.1(2) %, and the resolution is ≈ 7 % Full Width at Half Maximum (FWHM) at $E_\gamma = 1.33$ MeV.

The target is placed in a cylindrical tube, directly connected to the beam line, with a diameter of 11.7 cm and inner length of 48 cm. This chamber is brought to vacuum (≈ 0.1 Pa) and also contains the SiRi and NIFF detectors.

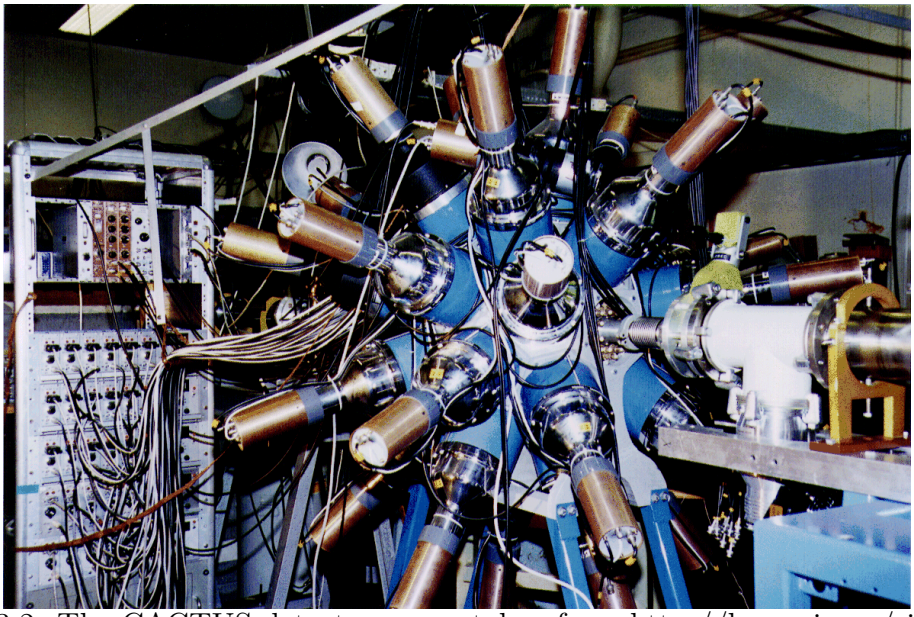

Figure 3.2: The CACTUS detector array, taken from http://lynx.uio.no/siri.html.

3.2.2 The SiRi particle telescope system

The γ rays detected in the NaI detectors are measured in coincidence with charged particle ejectiles. The Silicon Ring, SiRi [94], is composed of 64 [$\Delta E - E$] particle telescopes. The front ΔE detectors are 130 μm thick and the back E detectors are 1550 μm

thick. The array is shown in Figure 3.3. Each front detector ΔE is segmented into eight segments, each one covering a two degree angle, from 125° to 141° relative to the beam direction and at a distance of 5 cm from the target. Placing the particle detector at backwards angles from the beam direction drastically reduced the contribution from elastically scattered deuterons. Another advantage is that a broader spin distribution is populated in backward angles.

SiRi has been specifically designed to measure the outgoing particles observed in experiments at the OCL. The detection energy range is $3.7 - 16.5$ MeV for protons and $15.0 - 63.0$ MeV for α particles. Proper deuteron detection is possible for particles with energies between 4.9 and 22.3 MeV. The Full Width at Half Maximum (FWHM) for the total energy deposited in both the ΔE (front) and E (back) detectors is approximately $100 - 200$ keV.

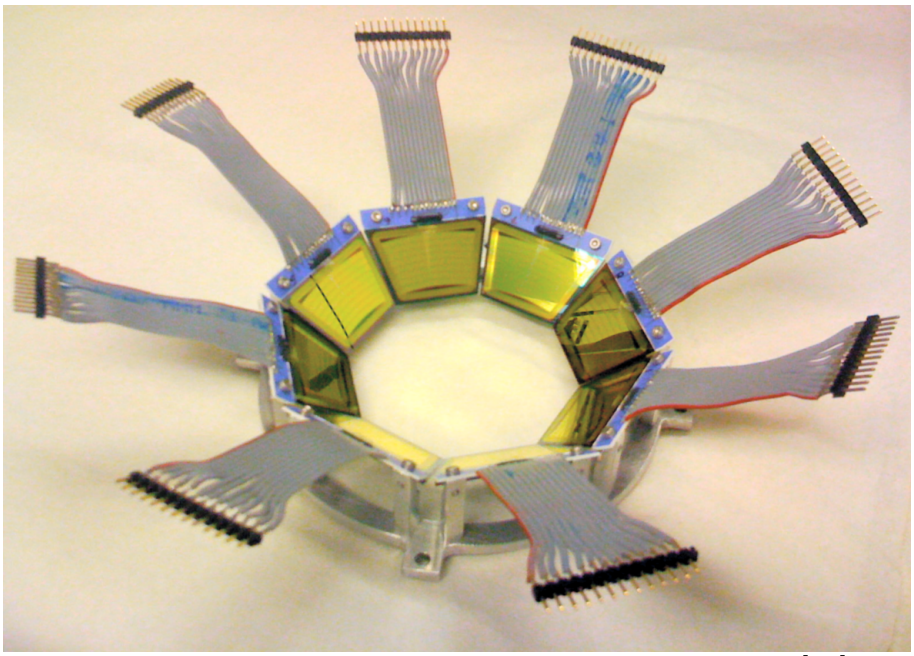

Figure 3.3: The SiRi particle telescope, picture taken from Ref. [94], Figure 3.

3.2.3 The NIFF array

The Nuclear Instrument for Fission Fragments (NIFF) array is used for the detection of fission fragments [95]. It is composed of four low pressure gas-filled Parallel Plate Avalanche Counters, (PPAC), and covers an estimated solid angle of 30 % of 4π and is shown in Figure 3.4. The face of each counter is at 45° with respect to the beam axis. The isobutane gas filling the detector gets polymerized by the avalanche process created by the interaction of an incident heavy ion. A constant gas flow is needed to maintain the detection efficiency. The detector's purpose is to tag or veto fission events. Therefore, it was designed to achieve high detection efficiency, fast time response (on the order of

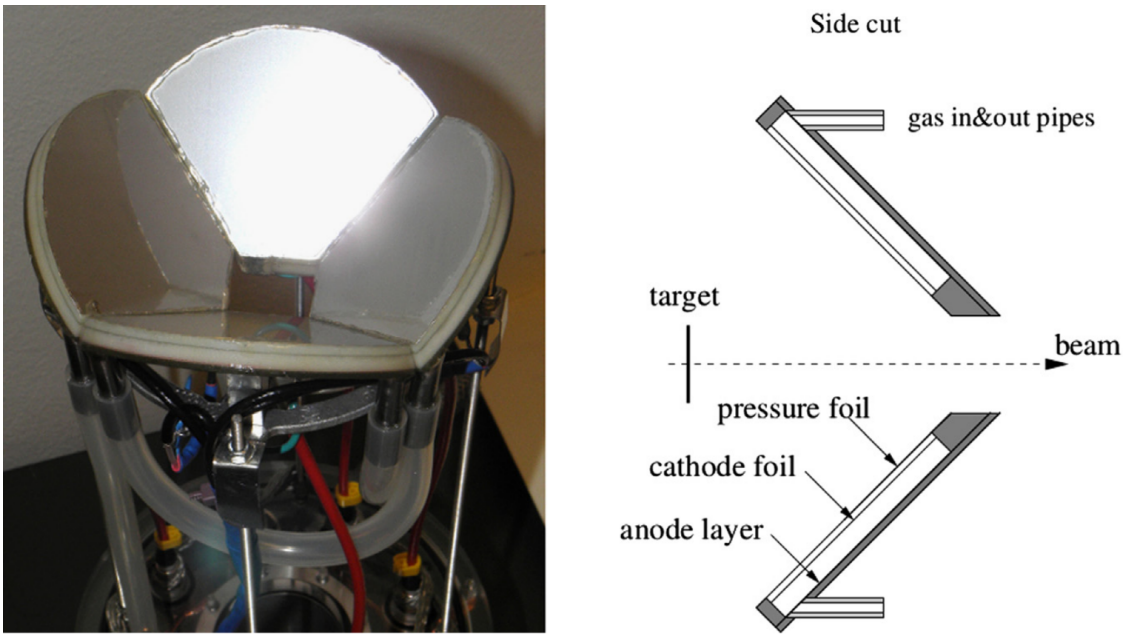

Figure 3.4: The NIFF fission fragment detector; taken from Ref. [95], Figure 2.

nanoseconds), durability, and sensitivity to only heavy ions (it should be insensitive to α particles or lighter ions, electrons and γ rays). Due to its design, there is no information about the energy or the position of fission fragments interacting. The intrinsic efficiency is above 90 %. The detection efficiency of one of the two fission fragment is 55(2) % [95].

3.2.4 Data acquisition

The signals from the 64 ΔE detectors from SiRi are sent to four 16-channel preamplifiers and one 16-channel preamplifier for the eight E detectors. The preamplified signals are sent to Mesytec STM-16 modules that serves as spectroscopy amplifiers, timing filter amplifiers and leading-edge discriminators. To start of the acquisition system it is possible to select between the following different master trigger conditions:

- output of at least one E detector (logic OR for all E detector outputs)
- output of at least one ΔE detector
- coincidence between E and ΔE detector

Because of the use of leading-edge discriminators and not constant fraction discriminators the signal rise times are different for different energy deposited. This is taken into account and corrected in the offline analysis as presented in Section 3.3.4.

The stop signal is individual for each of the 26 NaI detector and the four PPACs. A time gate is applied in the offline analysis to select γ-ray events coincident with the detection of a particle by SiRi.

3.3 Data analysis

In this section, details on the calibration of the particle spectra obtained from SiRi and γ-ray spectra obtained from CACTUS are given. Then, the timing and correction for the leading edge triggering is presented. The energy deposited in SiRi is then converted in the excitation energy left in ^{243}Pu after the (d,p) reaction. The measured data is then expressed as a matrix of the nucleus excitation energy versus the γ-ray spectra resulting from the de-excitation, which is the starting point of the Oslo method.

3.3.1 Particle spectra

Bombardment of the ^{242}Pu target with a deuteron beam opens several reaction channels. Calculation of the reaction Q value gives the threshold for the reaction to be energetically feasible. For a nuclear reaction $X(a,b)Y$, where a is the projectile impinging on a target nucleus X, and Y is the residual nucleus after emission of the ejectile b, the reaction Q value is given by:

$$Q = \left[m_a^0 + m_X^0 - m_b^0 - m_Y^0\right] \cdot c^2, \tag{3.1}$$

where m_i^0 is the rest mass of the nucleus/particle i and c is the speed of light in vacuum. Table 3.2 gives the Q values for the (d,p) reaction on ^{242}Pu and the major target contaminants as well as ^{27}Al from which the target holder is made of. Nuclear masses are taken from the NNDC database [96].

Table 3.2: Q values for the (d,p) reaction on ^{242}Pu, and the major target contaminants and the target holder.

Element	^{242}Pu	^{16}O	^{9}Be	^{237}U	^{238}Pu	^{241}Pu	^{241}Am	^{27}Al
Q (MeV)	2.809	1.919	4.586	3.930	3.422	4.085	3.313	5.501

Using the conservation of energy and momentum, we can predict the energy of the proton that will be detected by the particle telescopes. The conservation of the total energy for the reaction $X(a,b)Y$, on a stationary target X, is given by:

$$m_X^0 c^2 + m_a^0 c^2 + T_a = m_Y^0 c^2 + T_Y + m_b^0 c^2 + T_b, \tag{3.2}$$

where the m^0's are the rest masses and the T's are the kinetic energies. $T_X = 0$ because the target is stationary in the laboratory reference frame. By considering the plane defined by the incident projectile and the outgoing ejectile, the linear momentum conservation relation can be written as:

$$p_a = p_b \cos\theta + p_Y \cos\phi, \tag{3.3}$$

$$0 = p_b \sin\theta + p_Y \sin\phi, \tag{3.4}$$

where θ and ϕ are the angle as defined in Figure 3.5. The silicon detectors are positioned at fixed angles θ, and therefore, it is possible to calculate the kinetic energy of the ejectile that will be detected, T_b using Equations (3.2),(3.3) and (3.4).

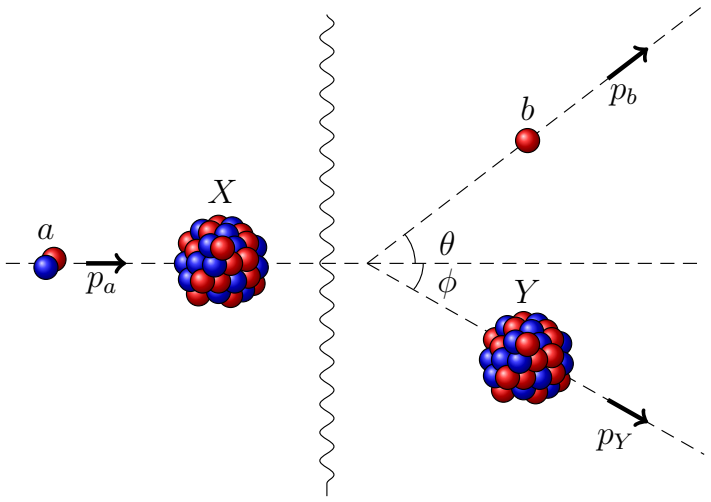

Figure 3.5: Schematic illustration of the kinematics of the $X(a,b)Y$ reaction.

The energy lost by the ejectile in the silicon $[\Delta E - E]$ detectors can be calculated using the Bethe-Bloch formula, giving the mean rate of energy loss per unit path length of the heavy charged particle in solids [97]:

$$-\frac{dE}{dx} = \frac{4\pi}{m_e c^2}\left(\frac{e^2}{4\pi\epsilon_0}\right)^2 \frac{Z\rho N_A z^2}{AM_u\beta^2}\left[\ln\left(\frac{2m_e c^2\beta^2}{I}\right) - \ln\left(1-\beta^2\right) - \beta^2\right], \qquad (3.5)$$

where m_e is the electron rest mass, c is the speed of light in vacuum, e is the electron charge, ϵ_0 is the vacuum permittivity, Z, A, and ρ are the atomic number, mass number and density of the absorbing medium, M_u is the molar mass constant, z is the charge state of the interacting particle, β is the special relativity factor of the charged particle and I represents the average excitation and ionization potential of the absorbing medium. For nonrelativistic charged particles, $\beta \to 0$ and only the first term in the brackets is significant. When comparing nonrelativistic charged particles, the dependence of the energy loss outside of the logarithm is z^2/β^2 meaning that the charge state has a quadratic influence on the energy loss. For ions with the same charge state, only β is influencing the energy loss. At low kinetic energies T_{ion}, $\beta \approx 2T_{\text{ion}}/(m_0 c^2)$, where m_0 is the rest mass of the ion. The energy loss is then linearly dependent on the rest mass. As a rule of thumb, at the same kinetic energy, a deuteron will lose twice as much energy as a proton, and an α particle will lose sixteen times as much energy as a proton.

Each particle type will, therefore, lose a different amount of energy in the ΔE detectors. The particle is then stopped in the E detector, losing all the energy left after

interacting in the ΔE detector. Characteristic banana-shaped curves for each type of particles are seen by plotting the energy deposited in the ΔE detector against the energy deposited in the back detector E, therefore allowing particle identification, as seen in Figure 3.6.

Predictions of the measured data using the SiRi array are made using the Qkinz[1] software developed at the University of Oslo. This software does the kinematic calculations, including the mean energy loss for the particle going through the target. The output is a calculated ΔE vs E spectrum for the SiRi detector. Figure 3.6 shows the expected energy lost in the front detector versus the back detector for protons (red), deuterons (green) and tritons (grey) detected after interaction of the 12 MeV deuteron beam with the ^{242}Pu target.

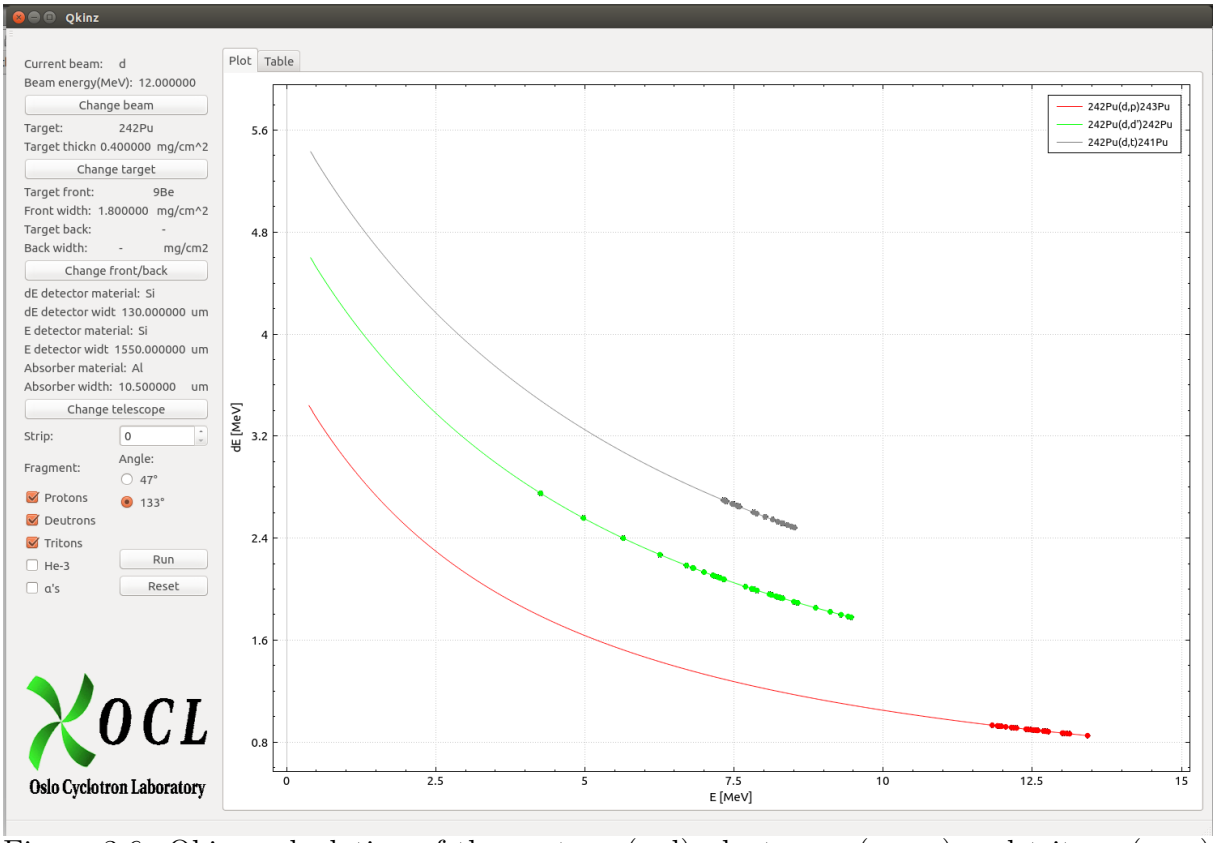

Figure 3.6: Qkinz calculation of the protons (red), deuterons (green) and tritons (grey) detected in strip 0 of SiRi after interaction between a 12 MeV deuteron beam and our ^{242}Pu target.

Figure 3.7 shows a measured ΔE vs E spectrum for one E detector and one ΔE strip ($\theta \in [139°; 141°]$). A total of 64 spectra are measured with the SiRi array. Horizontal and vertical features are due to incomplete charge collection in, respectively, the back

[1]The software can be downloaded at https://github.com/oslocyclotronlab/Qkinz

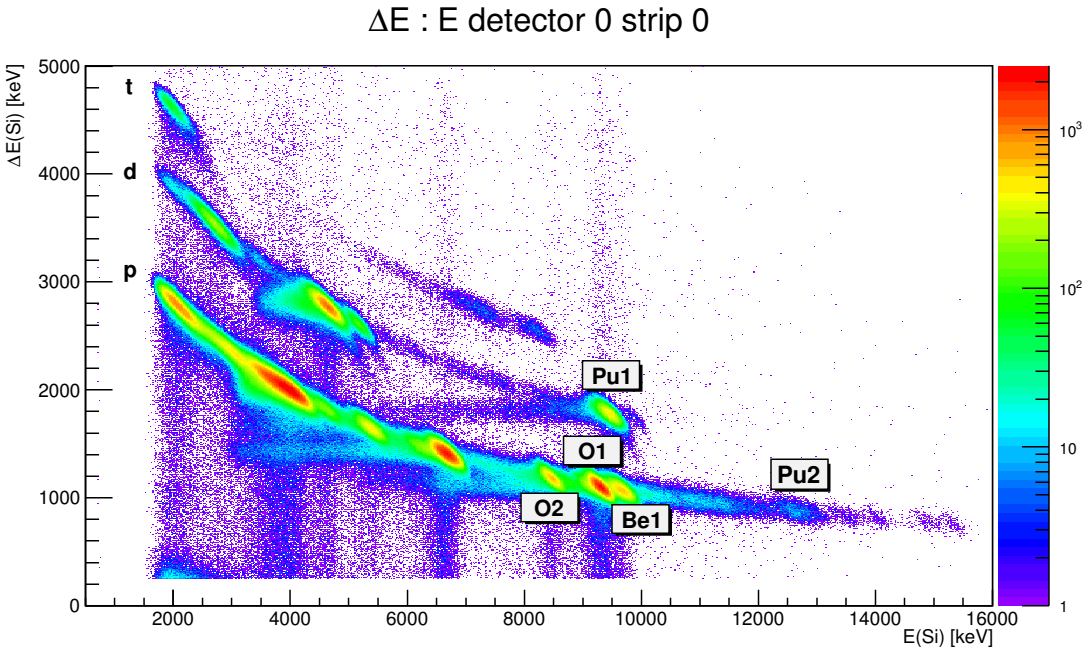

Figure 3.7: Measured $\Delta E - E$ spectrum, for one E detector and one ΔE strip ($\theta \in [139°; 141°]$). The proton (p), deuteron (d), and triton (t) bananas are clearly distinguishable.

E detector or the front ΔE detector. Contamination peaks from Oxygen (labeled O1 and O2 for (d, p) to respectively the ground state and first excited state of ^{17}O) and Beryllium (labeled Be1 for (d, p) to the first excited state of ^{10}Be which decays back to the ground state via internal conversion only) can be seen in the proton banana. In the ^{243}Pu excitation energy range of interest for the Oslo method (below the neutron separation energy), only O2 will produce γ rays and will need to be corrected for in the particle-γ coincidence spectrum.

Despite the fact that the O and Be peaks have good statistics and are well isolated, they are not used for energy calibration of the E and ΔE detectors. The proton energy following a (d, p) reaction on those light nuclei has a higher angular dependence in order to fulfill conservation of linear momentum. For a heavy nucleus like Pu, the effect is a lot smaller. If the angles for the detector stripes are slightly off, or if the target is not perfectly centered, the error on the energy calibration will be more important if light nuclei are used. For comparison, with an angle of 2° between 2 stripes, the difference in energy deposited in the back detector of the particle telescope is ≈ 5 keV for ^{242}Pu while it is 33, 45 and 69 keV for, respectively, ^{28}Si, ^{16}O and ^{9}Be. Thus, to calibrate the particle telescope in energy, Pu1 and Pu2 are chosen. Pu1 is the result of deuteron elastic scattering on ^{242}Pu.

A good Pu2 calibration point was more difficult to find since the (d, p) reaction to the ground state of ^{243}Pu is not seen in the ΔE vs E spectrum. Spectroscopic measurement

of ^{243}Pu has been realized using the ^{242}Pu(d,p) reaction in Ref. [98]. Cross sections for each energy level are measured at 90° and 150° with respect to the beam direction. Low lying states have small cross sections which explains why the (d,p) reaction to the ground state of ^{243}Pu is so weak that the state is not seen in the ΔE vs E spectrum. The first state seen is at 388 keV above the ground state. Results from Ref. [98] have been folded with a 180 keV FWHM detector response function to reproduce the spectrum using the MAMA software[2] as shown in Figure 3.8. This spectrum is a histogram of the number of counts as a function of the total energy deposited by the proton, $\Delta E + E$. The feature seen in the $\Delta E + E$ spectrum centered around 13500 keV corresponds to a group of states at $E_x \approx 835$ keV above the ground state in ^{243}Pu. This feature is used as the second calibration point Pu2 shown in Figure 3.7. Both E and ΔE detectors signals are digitized using a 2048 channels Analog to Digital Converter (ADC). A linear function is used to convert from channels (voltage) to the energy deposited by the particle in the detectors.

3.3.2 γ-ray spectra

The CACTUS array is composed of 26 NaI detectors, and it is used to detect γ rays. Interaction between γ rays and a NaI crystal occur via three main mechanisms: photoelectric absorption, Compton scattering and pair production.

The photoelectric absorption process is the complete absorption of the incoming γ ray by an atom. The energy is transferred to an outgoing electron from one of the atom bound shells. The most probable origin of the photoelectron is the most tightly bound shell [97]. In a NaI crystal, iodine atoms are the primary absorbers. The binding energy of the K-shell is ≈ 33 keV. A free electron from the medium is then captured and the vacancy created by the ejection of the photoelectron might be filled by an electron from a less tightly bound electron, producing a characteristic X-ray. In the majority of cases, the characteristic X-ray is reabsorbed near the original interaction site. If the photoelectric effect occurs near the surface of the detector, the X-ray might escape and the energy deposited in the detector decreases by the energy of the escaped X-ray. These peaks tend to be most prominent for low energy γ rays and large surface-to-volume ratio detectors. When an electron transitions to a lower shell, it is possible that the energy is transferred to an Auger electron.

The photoelectric effect is dominant for low energy γ rays. For NaI crystals, the probability for photoelectric absorption becomes smaller than Compton scattering for γ rays with energy greater than $E_\gamma \approx 200 - 400$ keV [97].

The Compton scattering process occurs when the incoming γ ray inelastically scatters on an electron. The energy transferred depends on the angle at which the photon is scattered, which results in a continuum of possible energies deposited in the NaI crystal. Multiple scatters within the detector can occur. In our experiment, cross-talk, i.e. inter-

[2]The Matrix Manipulation (MAMA) software allows application of arithmetic operations, peak fitting, smoothing and (un)folding procedures on one and two dimensional spectra [99].

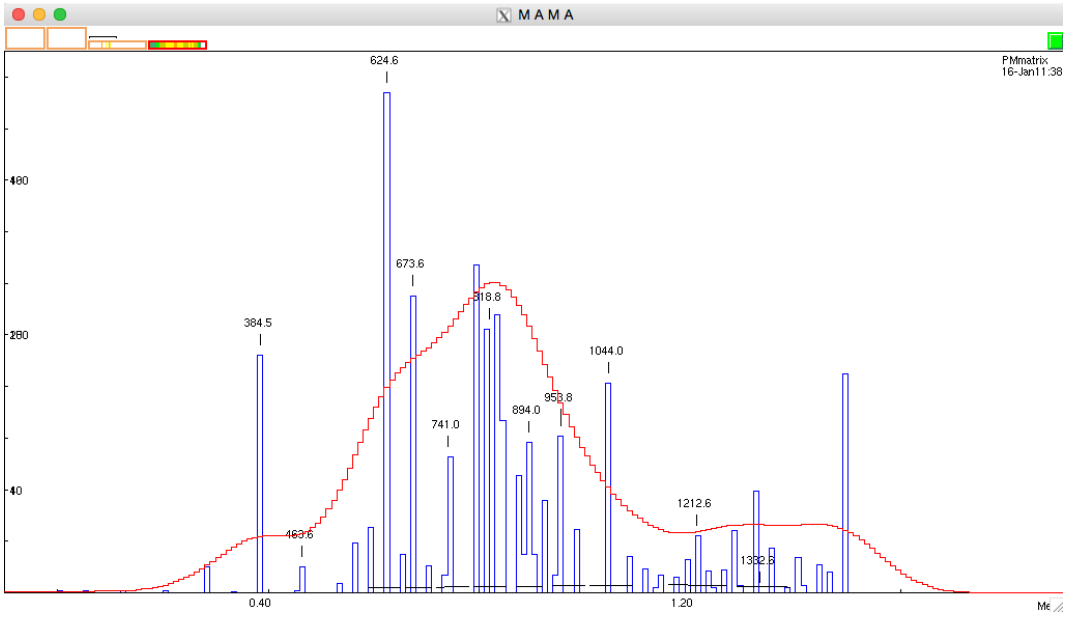

(a)

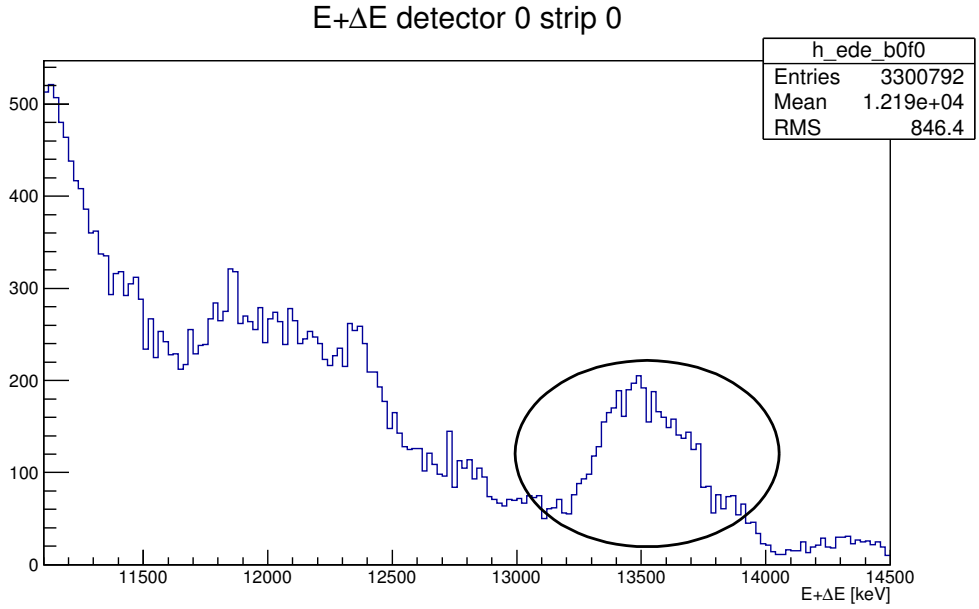

(b)

Figure 3.8: Second calibration point for the $\Delta E - E$ detectors corresponding to a group of states in ^{243}Pu centered around $E_x = 835\,\text{keV}$. (a) States measured in Ref. [98] folded with a 180 keV FWHM response function to reproduce SiRi's measurement using the Mama software [100]. The abscissa represents the excitation energy in ^{243}Pu. (b) Measurement of the $E + \Delta E$ spectrum for one strip. The feature in the ellipse corresponds to the prediction made with the Mama software. The abscissa is the energy of the proton after the (d, p) reaction, which is opposite to the excitation energy in ^{243}Pu.

action within multiple detectors is reduced by the presence of lateral shielding around the detectors. The remaining cross-talk is suppressed by requiring only one γ-ray detector to trigger within a given time stamp. Multiple detector triggering events are deleted because it is not possible to distinguish between two unrelated γ rays interacting in neighboring detectors or γ rays resulting from the same initial photon.

Pair production is only possible for γ rays with energy greater or equal to twice the electron rest mass energy (1.022MeV). The cross section for pair production increases with increasing γ-ray energy. Pair production consists of the absorption of the γ ray and the creation of an electron-positron pair. In order to conserve both energy and momentum, this process cannot occur in vacuum, but only when a photon is subject to the Coulomb field of a nucleus and some of its momentum can be transferred to the nucleus. The positron will quickly annihilate in the medium and create two 511 keV photons. In NaI detectors, pair production is the most probable interaction mechanism for photons with energy $E_\gamma > 6 - 8\,\mathrm{MeV}$ [97].

Figure 3.9, taken from Ref. [101], shows the contribution of the photoelectric absorption, Compton scattering and pair production to the linear attenuation coefficient of NaI as a function of the γ-ray energy. The linear attenuation coefficient, μ_l, is directly proportional to the reaction cross section σ:

$$\sigma = \frac{\mu_l}{\rho}\frac{M}{N_A}, \tag{3.6}$$

where ρ is the density of the material, M is the molar mass, and N_A is the Avogadro constant.

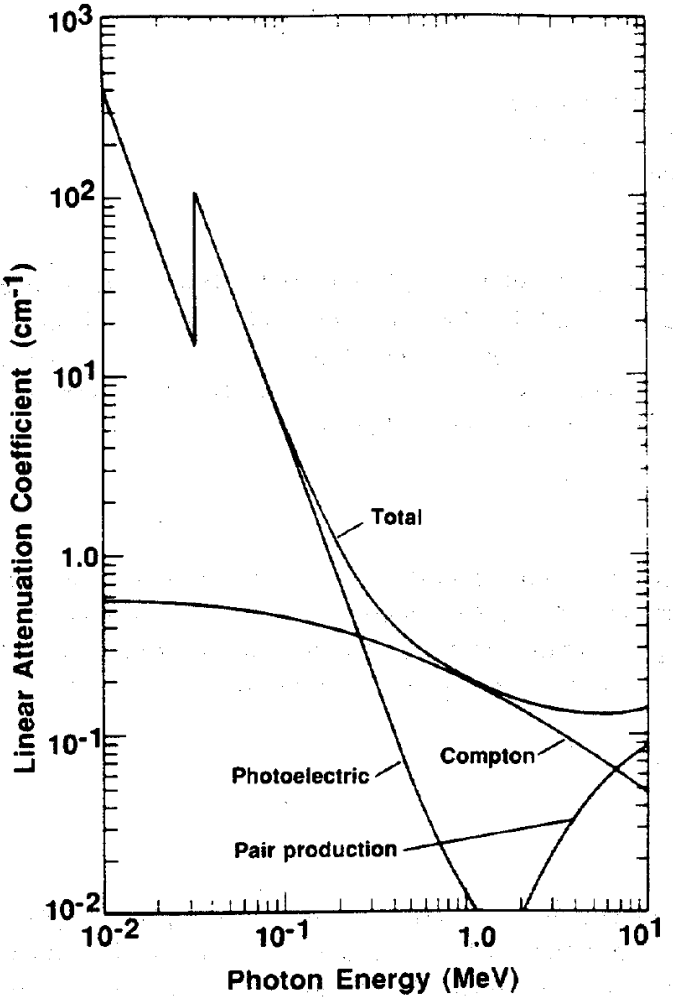

Figure 3.9: Linear attenuation coefficient of NaI. The different contribution from photo-electric effect, Compton scattering and pair production are shown; taken from Ref. [101], Figure 2.3.

The three processes lead to electrons being ejected from their atomic shell. Those electrons will travel through the NaI(Tl) crystal and excite electrons from the valence band (electrons bounded at lattice sites of the crystal) to the conduction band (electrons which have enough energy to move freely through the crystal). Those latter electrons will de-excite at the lattice sites where the Tl impurities are present. Those impurities modify the band structure from the one of a pure crystal and lower the gap energy between the valence and conduction band, facilitating de-excitation of conduction electrons back to the valence band. This transition will lead to the emission of visible photons whose energy is too low to re-excite the scintillation material. Those photons are collected by a photomultiplier tube located at one face of the crystal. Photons are converted into electrons by a photocathode located at the entry of the photomultiplier tube. Electrons

are accelerated by an electrical potential through a series of dynodes. The accelerated electrons will hit the dynodes releasing secondary electrons. An increasing number of electrons is released at each dynode. An anode is located at the end of the series of dynode. The current read on the anode is proportional to the amount of light that enters the photomultiplier tube, and therefore, to the energy deposited in the crystal.

In Figure 3.10 is shown a γ-ray spectrum from one of the 26 NaI detectors. Some photoelectric peaks are clearly discernible from the interaction of γ rays emitted by ^{17}O (871 keV), ^{10}Be (2590, 2895 and 3367 keV). Some features can be seen around 6 and 6.9 MeV and can be due to ^{16}O, ^{17}O or ^{10}Be. Figure 3.11 shows the energy region from 500 keV to 4000 keV. The 871 keV line is particularly hard to fit properly. It is fortunately possible to fit the 871 keV line from the time versus energy spectrum presented in Figure 3.15. A linear function is used to convert from channels (voltage) to the energy deposited by a γ ray in the detectors. Deviation from linearity for the CACTUS detectors remains very small and no general trend has been observed [93]. The energy calibration is checked using γ-ray spectra measured when the beam was hitting a natural $^{\text{nat}}$Si calibration target. Figure 3.12 shows the 1273 and 2028 keV lines from ^{29}Si and the 1779 keV line from ^{28}Si.

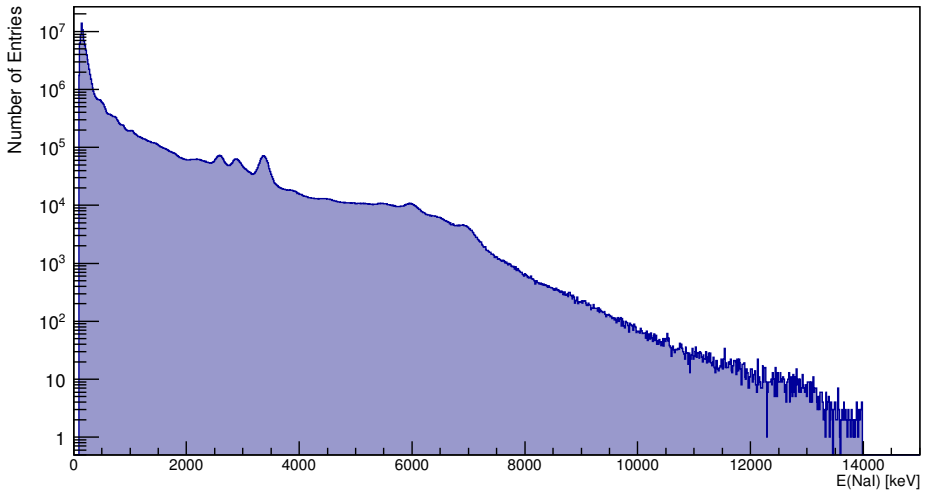

Figure 3.10: Full γ-ray spectrum from one NaI detector before unfolding.

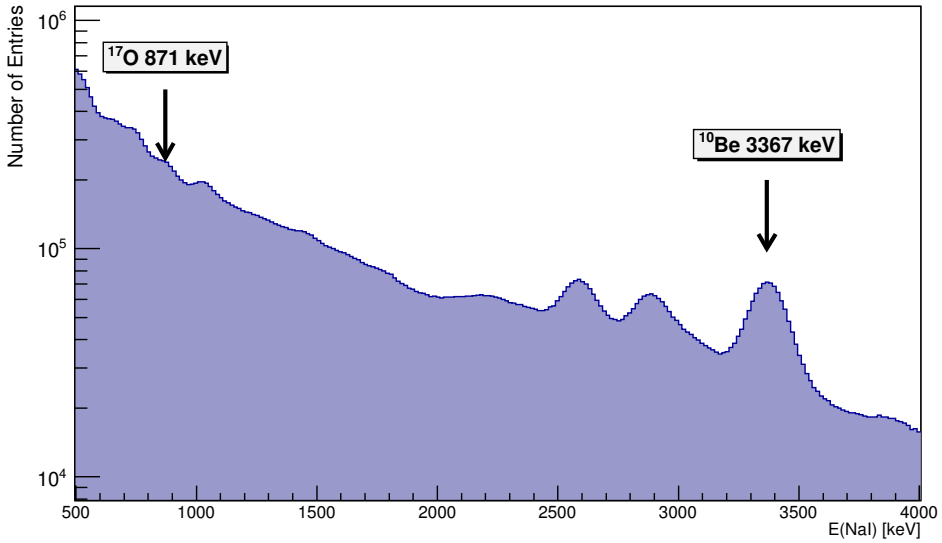

Figure 3.11: γ-ray spectrum from one NaI detector, before unfolding, showing the photoelectric peaks at 871 and 3367 keV from respectively ^{17}O and ^{10}Be used for the energy calibration of the NaI detectors.

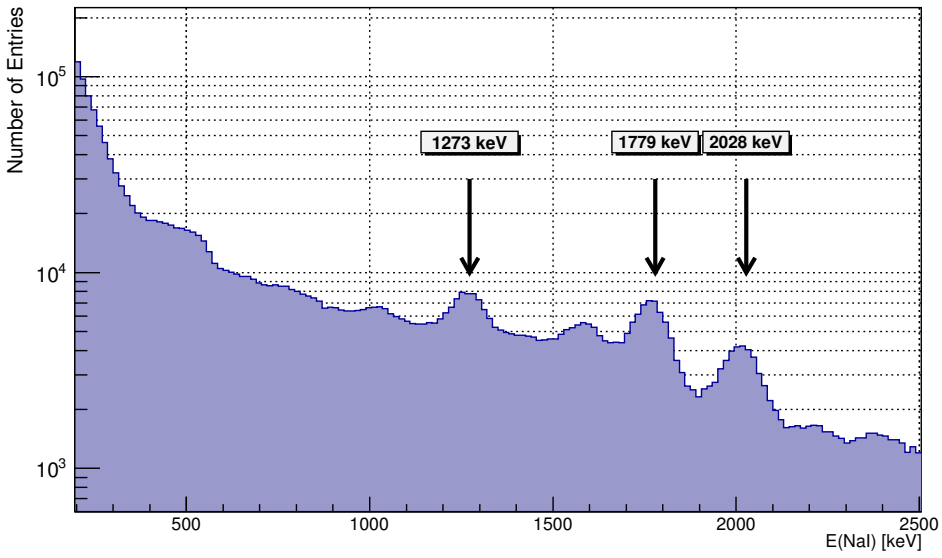

Figure 3.12: Raw γ-ray spectrum measured with a ^{28}Si calibration target.

3.3.3 Timing calibration

The start signal of the acquisition chain is given by detection of a charged particle in SiRi. The stop signal is given by interaction of one or more γ rays in the NaI detectors. The time between the start and stop signals is referred as Δt. The individual time spectra are aligned with a shift such that the prompt peak comes in the same channel arbitrarily set to $\Delta t = 0$ ns as shown in Figure 3.13. Detector channels 8 and 9 were not used while the signals from the four PPAC detectors from NIFF were recorded in channels 4, 12, 30 and 31.

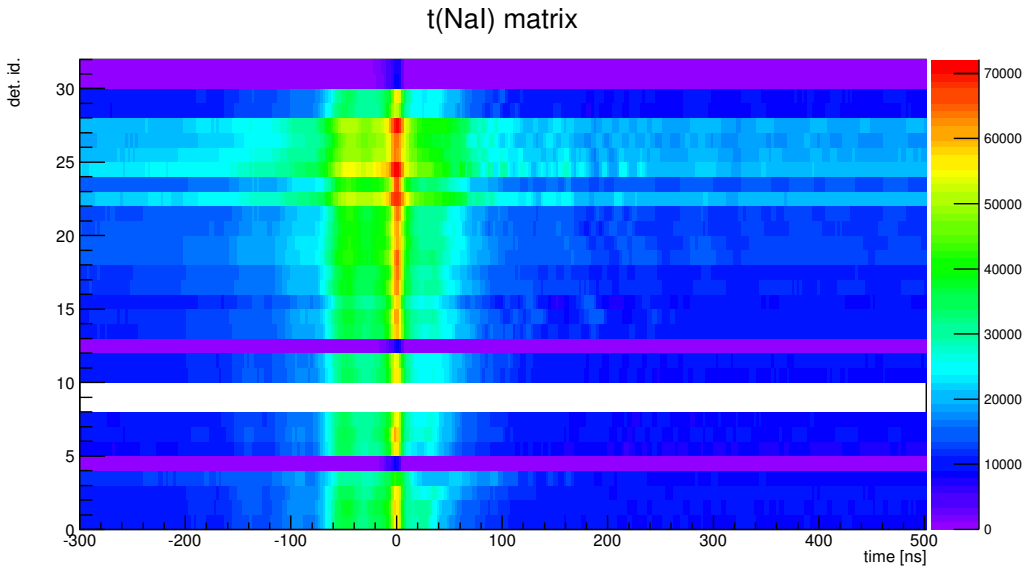

Figure 3.13: Timing spectra for the NaI detectors. The individual time spectra are aligned such that the prompt peak occurs at $\Delta t = 0$ ns. The detectors with ID 4, 12, 30 and 31 are the PPAC detectors. The detector channels 8 and 9 were not used.

3.3.4 Triggering

The start and stop logic pulses are generated using leading edge discriminators. Figure 3.14 shows two signals having identical shapes and start times but different amplitudes. They cross the trigger level at different times t_1 and t_2 introducing amplitude walk. Because lower energy γ rays will produce an electronic signal with lower voltage, they will appear delayed in time as seen in Figure 3.15. Similarly, walk can also be introduced if the shape of pulses or rise times of the signal are varying. Corrections for the walk has to be done before setting time gates to the data.

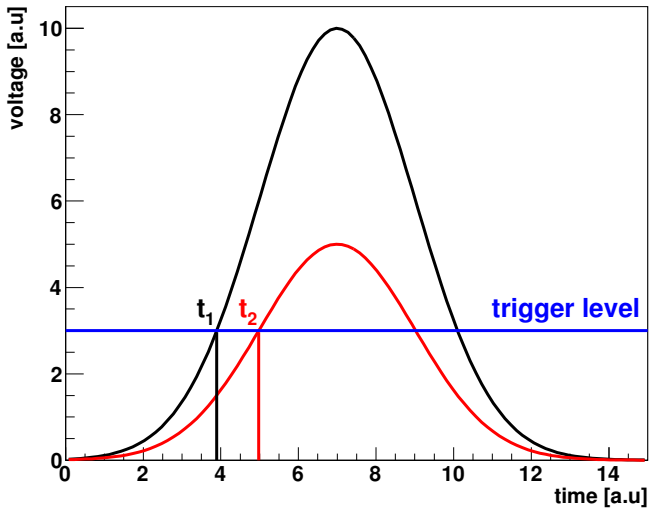

Figure 3.14: Amplitude walk due to the leading edge triggering. Two signals with identical shapes and start times but different amplitudes will cross the trigger level at different times.

Figure 3.15 shows a 2-D histogram of the stop time from the NaI detector versus the γ-ray energy measured for all NaI detectors. The low energy γ-ray stop signal comes at a later time compared to higher energy γ rays. To correct for walk, the time dependence is fitted with the following function [102]:

$$f = a_0 + a_1 \times t_{NaI} + \frac{a_2}{a_3 + t_{NaI}}, \tag{3.7}$$

where a_0, a_1, a_2 and a_3 are free parameters and t_{NaI} is the time difference between the start and stop signals which we want centered around $\Delta t = 0$ ns. Figure 3.16 shows the time versus energy spectrum once walk correction is applied. The stop signal from the NaI detectors is centered around $\Delta t = 0$ ns. The same correction needs to be applied to the particle detector array SiRi. Figure 3.17 shows the stop time in the NaI detectors as function of the energy deposited in SiRi. The correction is bad when less than 5 MeV are deposited in the E detector of SiRi. Fortunately it doesn't impact the analysis because the region of interest for the Oslo method is below the separation energy of ^{243}Pu, which corresponds to at least 7.8 MeV deposited in in the E detector of SiRi. Similarly, only γ rays with energy $E_\gamma > 900$ keV are used for the Oslo method so the spreading for low energy γ rays is not of interest.

Figure 3.18 shows the time versus energy deposited in the NaI detectors spectrum once walk correction is applied and for a maximum excitation energy left in ^{243}Pu below its neutron separation energy ($S_n(^{243}\text{Pu}) = 5.034$ MeV). The spectrum is a lot cleaner since most of the contamination γ rays (except contamination from ^{17}O with $E_\gamma = 870$ keV) occur when the excitation energy is higher than the ^{243}Pu neutron separation energy as it can be seen in Figure 3.21.

Once the raw data are corrected for the walk, a time gate around the prompt peak can be applied (≈ 50 ns window center around $\Delta t = 0$ ns) as indicated by the two horizontal black lines in Figure 3.18. Thus the background can be subtracted.

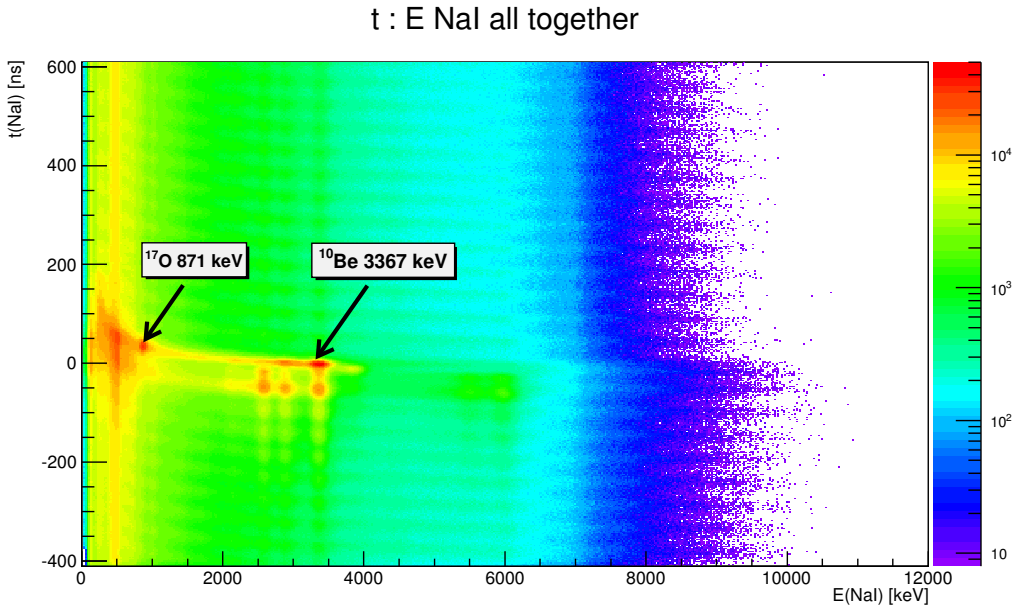

Figure 3.15: 2-D histogram of the time difference between the start and stop signals as a function of the γ-ray energy. Walk is clearly seen as the stop signal comes at later times for low energy γ rays. The periodicity is due to events coming from former or latter cyclotron turns.

3.3.5 From $E + \Delta E$ to E_x

Now that the detectors are calibrated and corrected for walk due to the leading edge discrimination triggering, the energy deposited in the particle telescopes needs to be converted into the excitation energy left in a ^{243}Pu nucleus after the (d, p) reaction. The excitation energy of the nucleus E_x is given by:

$$E_x = E_d + Q - E_p, \tag{3.8}$$

where $E_d = 12\,\text{MeV}$ is the energy of the incoming deuteron beam, Q is the Q value for the (d, p) reaction and E_p is the outgoing proton energy. Following the nuclear reaction, the proton has to go through the 1.8 mm Be target backing and a 10.5 μm Al layer on the surface of the particle telescope. The attenuation is taken into account using the Qkinz program shown in Figure 3.6. A table of corresponding excitation energies, E_x, and total energy deposited in the particle telescopes, $\Delta E + E$, is given as output of the calculation.

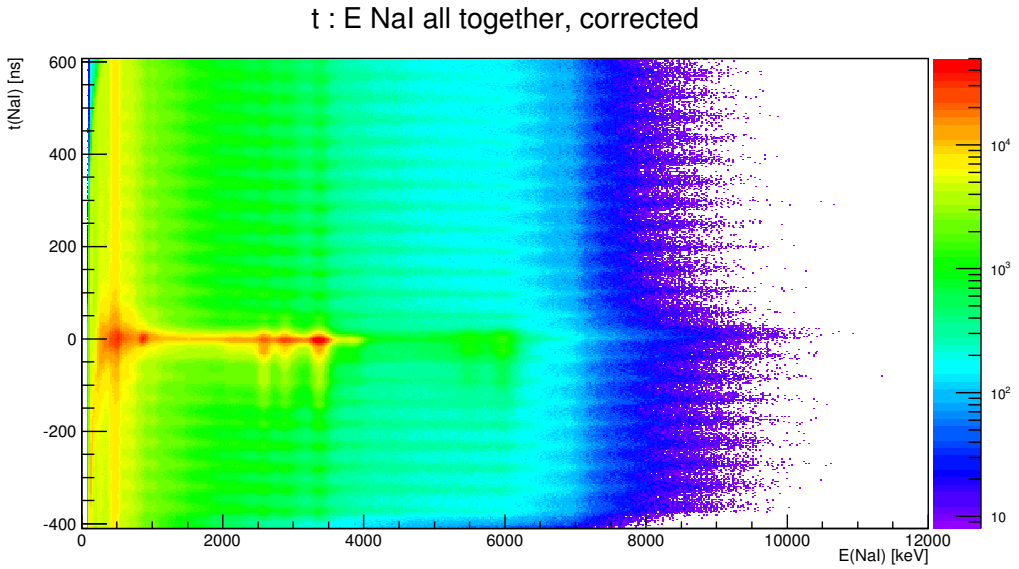

Figure 3.16: 2-D histogram of the time difference between the start and stop signals as a function of the γ-ray energy after walk correction. A time gate can now be applied on the NaI detectors to correct for background.

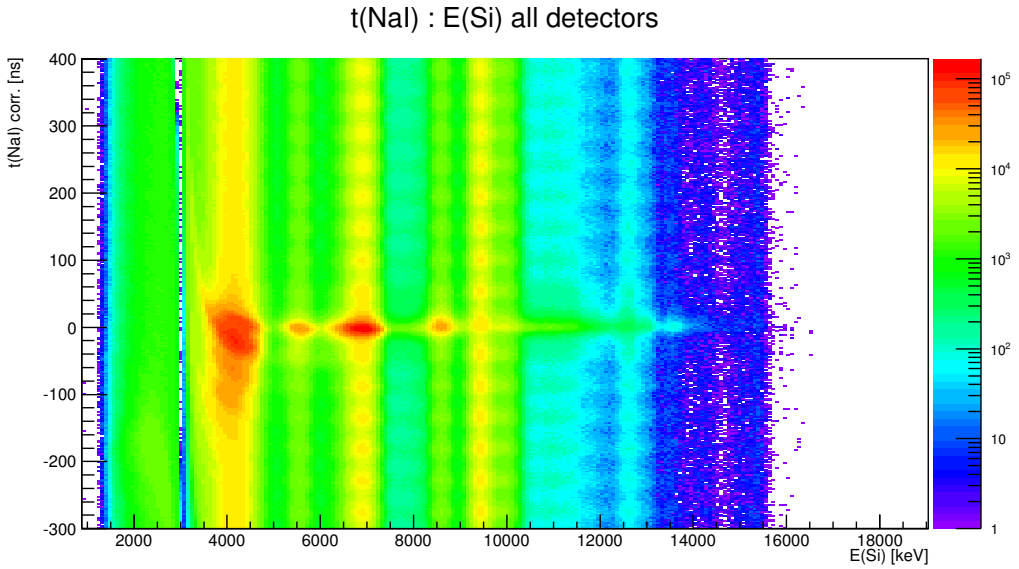

Figure 3.17: 2-D histogram of the time difference between the start and stop signals as a function of the energy deposited in the E particle detector after walk correction.

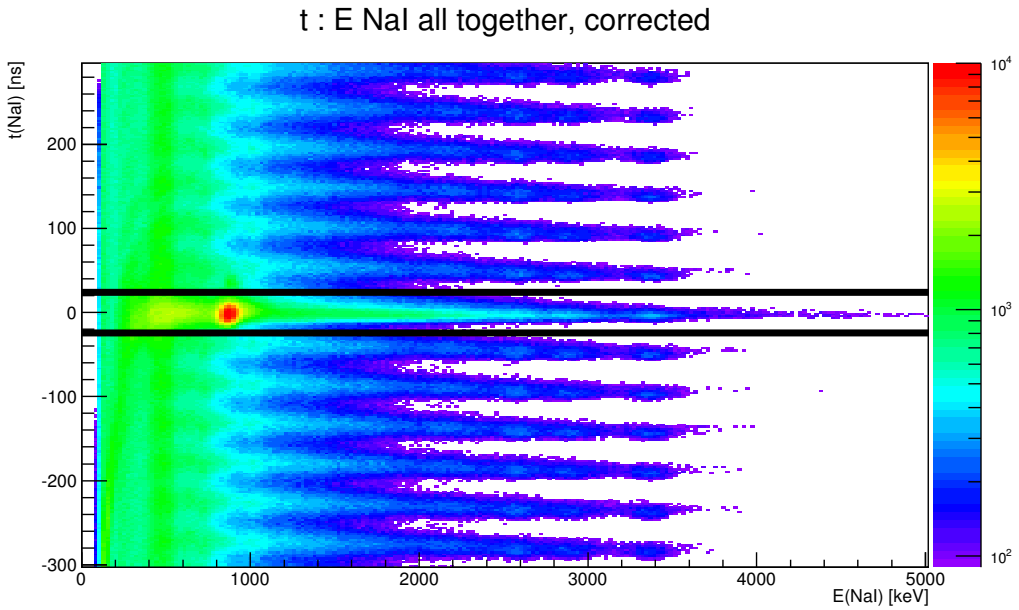

Figure 3.18: 2-D histogram of the time difference between the start and stop signals as a function of the γ-ray energy after walk correction restricting the excitation energy left in ^{243}Pu to be below the neutron separation energy. The time window is given by the two black lines.

A second order polynomial function is fitted through the points, giving the excitation energy as a function of the total energy deposited in SiRi, $(\Delta E + E)$:

$$E_x = a_0 + a_1(\Delta E + E) + a_2(\Delta E + E)^2, \tag{3.9}$$

where a_0, a_1 and a_2 are free parameters. The a_0 parameter corresponds to the sum of the deuteron energy and Q value from Eq. 3.8, but corrected for attenuation in the target backing. The attenuation is $\approx 0.8 - 0.9$ MeV over the angular range covered. The a_1 parameter corresponds to the proton energy dependence in Eq. 3.8, also corrected from attenuation in the target backing, and is therefore close to -1. The a_2 parameter, describing the non-linearity of the excitation energy as a function of the energy deposited in the particle detector, remains fairly small. The tables of corresponding E_x, ΔE and E along with the a_i parameters for each detector ring can be found in Appendix A.

Fine tuning of the excitation energy is realized by fitting the feature at $E_x \approx 835$ keV that was used for the calibration (see Figure 3.8). The alignment of the eight detector rings is shown in Figure 3.19.

3.3.6 Correction for fission events

The NIFF detector is used to veto fission events. For ^{243}Pu, the fission barrier is empirically predicted at 6.05 MeV [25], which is above the neutron separation energy,

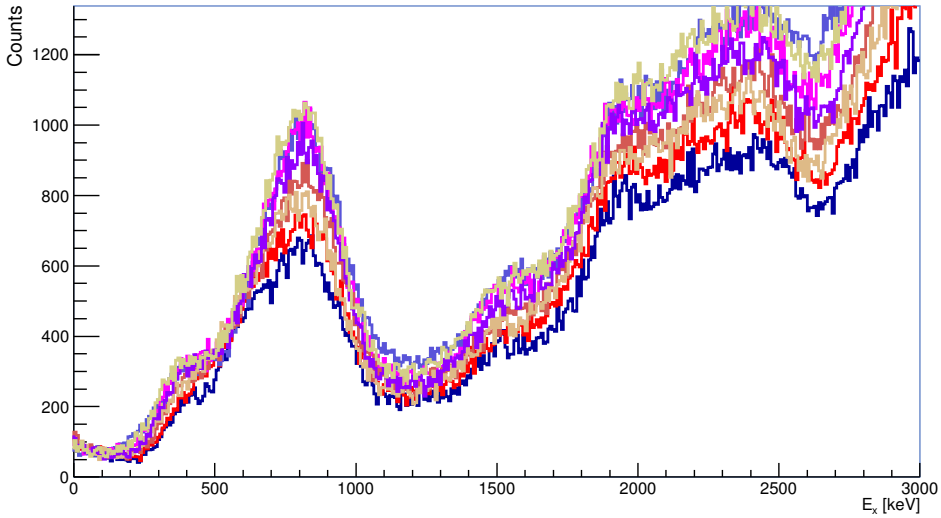

Figure 3.19: Alignment of the eight particle detector rings. The feature at $E_x \approx 835\,\text{keV}$, was used for the calibration and predicted using available particle spectroscopy data (see Figure 3.8).

$S_n^{^{243}Pu} = 5.034\,\text{MeV}$ [103]. The Oslo method only allows extraction of the level density and γ-ray strength function up to the neutron separation energy. Figure 3.20 (a) shows coincident particle-γ events as a function of the excitation energy (blue) and requiring coincidence with the fission detector (red). The fission barrier is clearly visible with the sharp rise of coincident particle-γ-fission events between 5 and 6 MeV. Some sub-barrier fission events are seen between 3 and 4MeV, and have been observed in other actinides[104, 105]. The number of coincident fission events is at least two orders of magnitude lower than the total number of events for the energy region of interest. Figure 3.20 (b) shows the particle-γ coincident events (blue curve) and particle-γ-fission coincident events (red curve) as a function of the γ-ray energy deposited in the NaI detectors. At all γ-ray energies the number of coincident particle-γ-fission events is negligible with regards to the number of coincident particle-γ events. We note the Maxwellian shape of the prompt fission γ rays. The level density and γ-ray strength function have been extracted with and without fission corrections over the excitation energy range $E_x = 2.6 - 4.3\,\text{MeV}$, and as expected, no statistically significant deviation is observed.

3.3.7 Extraction of the particle-γ matrix

Now that the excitation energy left in the residual ^{243}Pu nucleus is correctly calibrated, along with the γ-ray energy deposited in the NaI detectors, a particle-γ matrix can be extracted. The following gates and corrections are used:

- Particle gate on the proton banana, thus only considering $(d, p\gamma)$ events

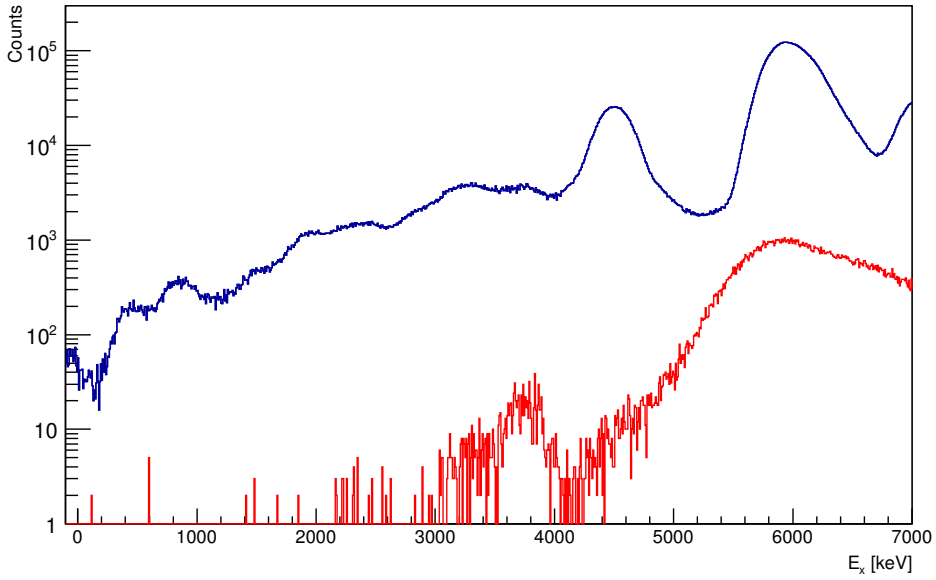

(a)

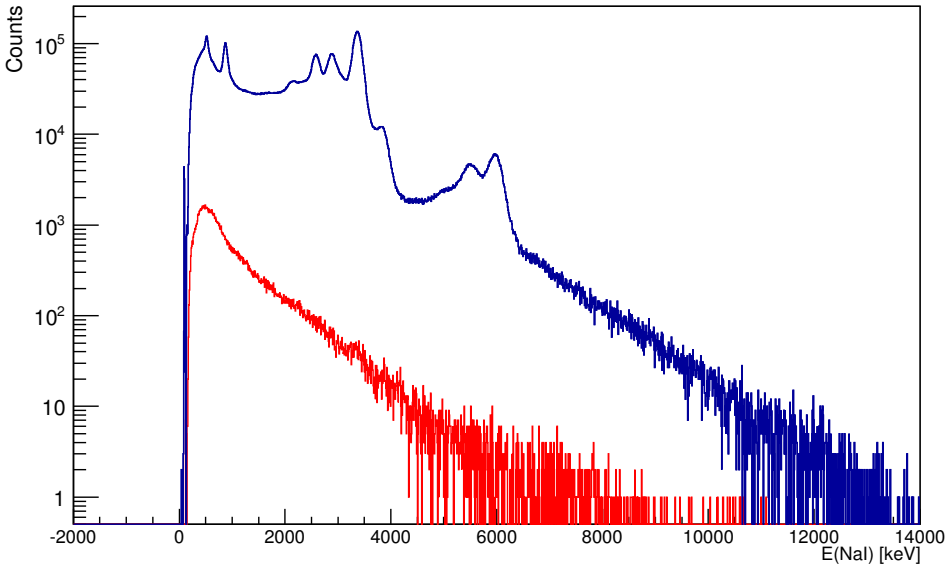

(b)

Figure 3.20: (a) Comparison of the number of γ rays measured as a function of the excitation energy left in the residual nucleus in coincidence with fission (red curve) and without (blue curve). (b) Comparison of the number of γ rays measured as a function of their energy in coincidence with fission (red curve) and without (blue curve).

- Time gate on the NaI stop time. Only events with time $\Delta t \in [-24\,\text{ns}, +24\,\text{ns}]$ are considered and background subtracted.
- Subtraction of fission events[3].

The raw particle-γ matrix is shown in Figure 3.21. Below the ^{243}Pu neutron separation energy indicated by the horizontal black line, there is one contamination line from ^{17}O at $E_\gamma = 871\,\text{keV}$, which will be subtracted. This particle-γ spectrum is the starting point of the Oslo method described in Chapter 4.

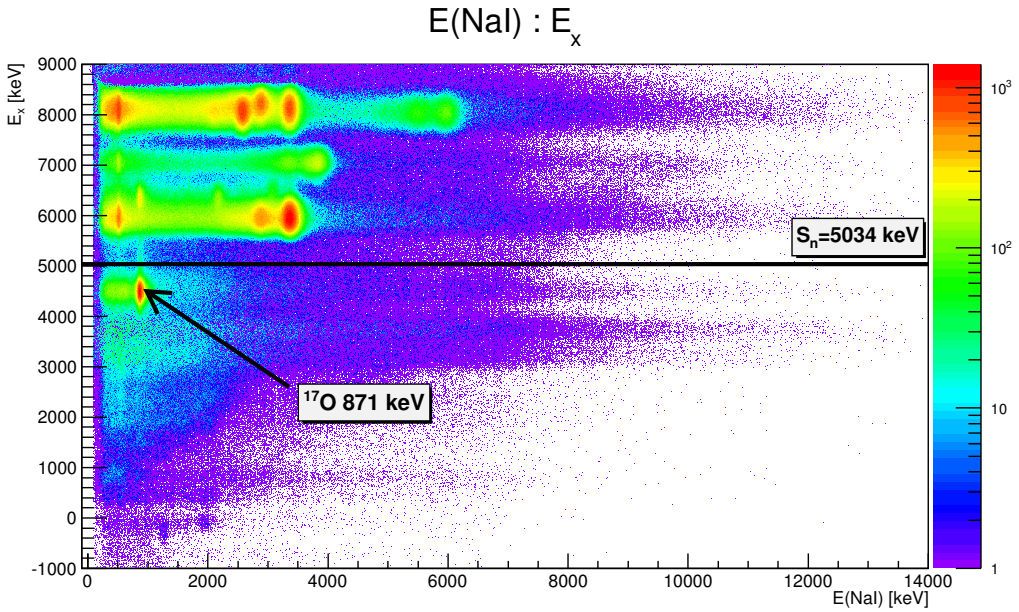

Figure 3.21: Raw particle-γ spectrum. Below the neutron separation energy of ^{243}Pu, there is only one contamination line from ^{17}O at $E_\gamma = 871\,\text{keV}$.

[3]No statistical significant deviation has been observed with no correction for fission.

Chapter 4

The Oslo method

Starting from the raw particle-γ-ray matrix, the Oslo method leads to simultaneous extraction of the level density and the γ-ray strength function. The raw particle-γ-ray matrix is first unfolded with the known NaI detector response. A folding iteration method [4] similar to Ref. [106] is applied to estimate the shape of a spectrum containing a Compton continuum, single and double escape peaks. The obtained spectrum is then subtracted from the measured spectrum to obtain the true full γ-ray energy spectrum. From it, the distribution of first generation γ rays is extracted by an iterative subtraction method described in Ref. [3]. This first generation matrix is proportional to the product of the level density times a transmission coefficient (from which the γ-ray strength function is calculated) [5]. The level density and γ-ray strength function need to be normalized since only their functional forms are extracted in a model independent way via the Oslo method.

4.1 Unfolding

Several different interactions of γ rays with the NaI detectors can occur, such as the photoelectric effect, Compton scattering and pair production, as described in Section 3.3.2. This leads to complicated detector response functions as shown in Figure 4.1 showing the response of a LaBr detector to a 3 MeV monoenergetic γ-ray source. The LaBr spectrum is shown here instead of the response of a NaI detector used in this work because of its better energy resolution to clearly distinguish the different features.

The principal features of a γ-ray spectrum are the full energy peak (f), corresponding to the γ ray depositing all its energy via photoelectric absorption or multiple scatter through the detector. It also assumes that all photoelectrons are stopped in the detector, as well as characteristic X-rays. The single (s) and double (d) escape peaks correspond to pair production within the detector and one or two 511 keV γ rays escaping from the detector after the electron-positron annihilation. An annihilation peak at 511 keV is seen from electron-positron annihilation in the materials surrounding the detectors. Lastly, if the incident photon is scattered by an electron, only a partial amount of its energy

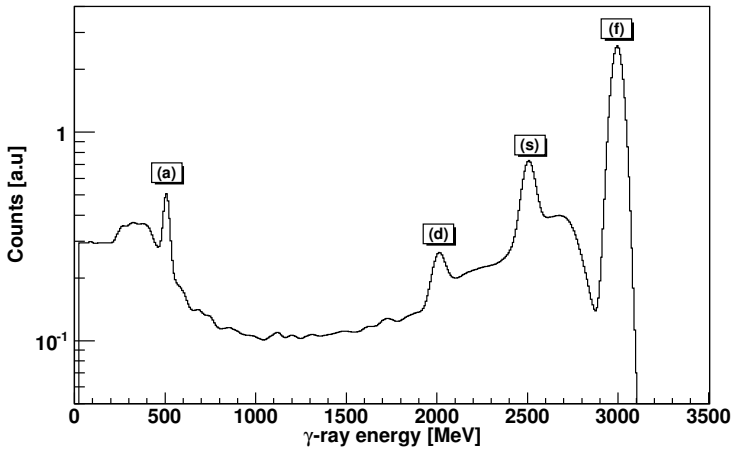

Figure 4.1: Folded spectrum for a monoenergetic 3 MeV γ-ray source. Distinct features can be seen, the full energy peak (f), the single (s) and double (d) escape peaks as well as the annihilation peak (a). (s), (d) and (a) are on top of the Compton continuum distribution. This spectrum is obtained for a LaBr detector which has better energy resolution than the NaI used in this work.

is deposited in the detector, depending on the scattering angle. The event will appear in the Compton continuum. Events corresponding to an energy deposited less than the full energy are rather frequent. In the NaI detectors used, the probability for full energy deposition varies from 74% for a 100 keV incident photon to 11% for a 10 MeV incident photon [4].

The response function of the detector $R(E, E_\gamma)$, where E_γ is the energy of the incident photon and E the energy deposited in the detector, should ideally be know for all possible incident γ-ray energies. Unfortunately, only a few monoenergetic γ-ray sources are available. The response function has been measured for a total of 10 monoenergetic lines ranging from 122 to 15110 keV from radioactive sources and in-beam experiments [4]. Proper interpolation between measured incident photon energies is necessary. The interpolation is easily done for peak structures, modeled by Gaussian distributions, knowing the detector energy dependent efficiency and resolution. Proper interpolation of the Compton continuum is more complicated because the energy deposited in the detector, E, depends on both the incident γ-ray energy, E_γ, and the angle θ at which it gets scattered:

$$E = E_\gamma - \frac{E_\gamma}{1 + \frac{E_\gamma}{m_e c^2}(1 - \cos\theta)}, \tag{4.1}$$

where $m_e c^2$ is the rest mass energy of the electron. The observed Compton continuum energy range is increasing with increasing incident photon energy. The interpolation is done connecting channels corresponding to the same scattering angle θ. In Figure 4.2, the

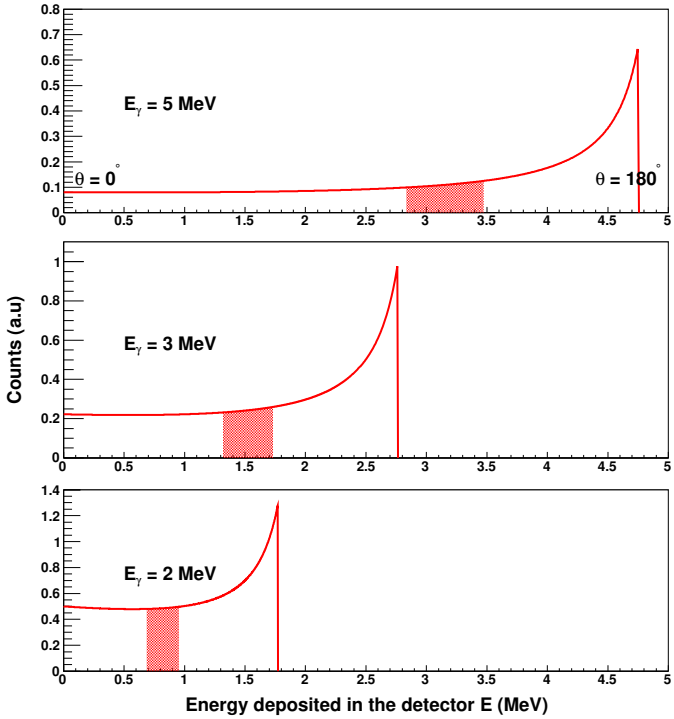

Figure 4.2: Calculation of the Compton continuum for three different incident photon energy E_γ for all angles. The colored band under the curve represents the Compton continuum for a scattering angle $\theta \in [30°, 40°]$. Interpolation between different incident photon energies is complicated by the deposited energy and scattering angle dependence of the Compton continuum to the incident photon energy. Those Compton continuum curves have not been convoluted with the detector resolution and efficiency and assume that no multiple scattering occurs within the detector volume. The figure is inspired by Fig. 1 from Ref. [4].

distribution of the energy E lost by a photon undergoing Compton scattering is plotted. It corresponds to what would be seen in a detector with perfect resolution and constant efficiency. It is also assumed that no multiple scattering occurs within the detector volume. The energy deposited differential cross section for Compton scattering, $\mathrm{d}\sigma_c/\mathrm{d}E$, is given by:

$$\frac{\mathrm{d}\sigma_c}{\mathrm{d}E} \propto \frac{1}{E_\gamma^2}\left[2 + \frac{(m_e c^2)^2 E^2}{E_\gamma^2(E_\gamma^2 - E^2)} + \frac{E(E - 2m_e c^2)}{E_\gamma(E_\gamma - E)}\right]. \tag{4.2}$$

The colored area under the curve represents the Compton continuum for a scattering angle $\theta \in [30°, 40°]$. This figure illustrate the variation of the energy range of the Compton continuum and the variable number of energy bins corresponding to a given angle range.

Given the appropriate response function function of the detector, $R(E, E_\gamma)$, discretized in a matrix $\mathbf{R}$, the folding iteration method described in Ref.[4] is used because it is reliable even with spectra where the number of counts are strongly fluctuating from channel to

channel. The method takes advantage of the fact that the folding operation (multiplying the unfolded by the detector response function) is computationally easy and fast. The matrix element R_{ij} corresponds to the detector response in the energy channel i when the detector is hit by a incident photon of energy E_γ corresponding to channel j. Each response function for a channel j is normalized to 1:

$$\forall j, \quad \sum_i R_{ij} = 1. \tag{4.3}$$

The folding procedure is then given by:

$$\begin{pmatrix} f_1 \\ f_2 \\ \vdots \\ f_N \end{pmatrix} = \begin{pmatrix} R_{11} & R_{12} & \dots & R_{1N} \\ R_{21} & R_{22} & \dots & R_{2N} \\ \vdots & \vdots & \ddots & \vdots \\ R_{N1} & R_{N2} & \dots & R_{NN} \end{pmatrix} \begin{pmatrix} u_1 \\ u_2 \\ \vdots \\ u_N \end{pmatrix}, \tag{4.4}$$

where f_i and u_i represent, respectively, the folded and unfolded spectra. A diagram of the folding algorithm is shown in Figure 4.3. The first trial function for the unfolded spectrum $u^{(0)}$ is the experimentally measured spectrum r. A first folding spectrum $f^{(0)}$ is calculated using the detector response function $\mathbf{R}$. A new trial function is obtained by adding the difference between the measured spectrum and the calculated folded spectrum to the previous trial function. This process is repeated until the folded spectrum agrees with the measured spectrum within experimental uncertainties. With about 10 iterations, the folded spectrum $f^{(i)}$ agrees with the measured spectrum. It has been observed [4, 107] that the best unfolding results are obtained when the response matrix is calculated with an energy resolution smaller than the experimentally observed one. As suggested, the energy resolution of the response matrix is half of the experimental one.

The obtained unfolded spectrum $u^{(i)}$ displays strong oscillations, which gives an artificially better resolution than the experimental one. A Compton subtraction method [4] is used to correct this effect.

We define $p_f(i)$, $p_s(i)$, $p_d(i)$, $p_a(i)$ and $p_c(i)$ the probabilities of observing, for an incoming photon in the energy channel i, respectively a photopeak, single escape peak, double escape peak, annihilation peak or Compton continuum. Estimated values for those probabilities as a function of the incoming photon energy is given in Table 1 from Ref. [4]. Starting the Compton subtraction method with the unfolded spectrum obtained with the folding algorithm, renamed $u_0 = u^{(\text{last})}$, we define the expected contribution from the full energy deposition peak, u_f, single escape peak, u_s, double escape peak, u_d, and annihilation peak, u_a:

$$u_f(i) = p_f(i)u_0(i), \tag{4.5}$$

$$u_s(i - i_{511}) = p_s(i)u_0(i), \tag{4.6}$$

$$u_d(i - i_{1022}) = p_d(i)u_0(i), \tag{4.7}$$

$$u_a(i_{511}) = \sum_i p_a(i)u_0(i), \tag{4.8}$$

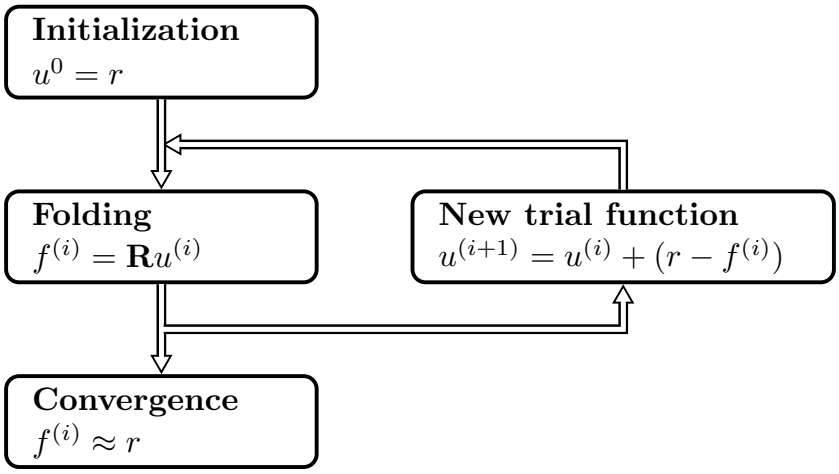

Figure 4.3: Diagram of the folding algorithm. r is the measured spectrum, $u^{(i)}$ are the trial unfolded spectra, $f^{(i)}$ the trial folded spectra and $\mathbf{R}$ the detector response matrix.

where i_{511} and i_{1022} are the channels corresponding to $E = 511\,\text{keV}$ and $E = 1022\,\text{keV}$. In order to reproduce the experimental data, the u_a spectrum corresponding to the annihilation peak is smoothed to reproduce the experimental energy resolution. The resolution of u_f, u_s, u_d is determined by the resolution of the measured spectrum and the response matrix. Those spectra are smoothed to match the experimental resolution. The Compton continuum spectrum $u_c(i)$ can be obtained by subtracting all the other features from the measured spectra $r(i)$:

$$u_c(i) = r(i) - u_f(i) - u_s(i) - u_d(i) - u_a(i). \tag{4.9}$$

The obtained Compton continuum spectrum $u_c(i)$ still displays strong oscillations when it should be slowly varying as function of energy. This spectrum is smoothed again. The final resolution of u_c is $\sqrt{2}$ times the experimental resolution. The new unfolded spectrum, u_{new} is obtained by subtracting the smoothed Compton continuum along with all features others than the photopeak, weighted by the photopeak probability, $p_f(i)$, and corrected for the γ-ray detection efficiency, ϵ_γ:

$$u_{new}(i) = \frac{r(i) - u_c(i) - u_s(i - i_{511}) - u_d(i - i_{1022}) - u_a(i_{511})}{p_f(i)\epsilon_\gamma(i)}. \tag{4.10}$$

4.2 First generation γ rays

The γ decay from a highly excited state will most likely involve a cascade of γ rays. Transitions in the actinides are generally very fast (below 1 ns for the few states which lifetime was measured and generally on the order of the femtosecond), except for very

few low-lying isomeric states. It is, therefore, not possible to determine the order in which those γ rays are emitted with timing techniques. The unfolded spectrum shown in Figure 5.3 contains γ rays from all generations in the cascade.

A subtraction method was developed by the Oslo nuclear physics group to extract the first generation γ rays from the unfolded spectrum [3]. It is assumed that the γ decay from an excited energy bin is independent on how the states in the energy bin were populated, whether from γ decay from a higher excited state or from a particle induced reaction. This assumption is automatically fulfilled when the cross sections for the two different population mechanism are equal for all states.

Starting from the unfolded spectra u_i obtained from the unfolding procedure, the first generation spectra f_i is given by:

$$f_i = u_i - g_i, \tag{4.11}$$

where g_i is a weighted sum of the unfolded spectra:

$$g_i = \sum_j n_{ij} w_{ij} u_j. \tag{4.12}$$

The sum is carried over all excitation energy bins j. The unknown coefficients w_{ij} correspond to the decay probability from the excitation energy bin i to the bin j. It is equivalent to the branching ratio of each primary γ ray depopulating the excitation energy bin i. Therefore, the w_{ij} values correspond to a first generation spectrum f_i normalized to 1. The n_{ij} coefficients are correction factors for the different population cross sections of the excitation energy bin i cascading to the energy bins j. Those coefficients are determined such that $n_{ij}u_j = k$, with k being a constant independent of j, corresponding to a fixed number of γ-ray cascades. The n_{ij} coefficients can be calculated following two different normalization depending on the experimental conditions [3].

- *Singles normalization:* The number of populated states is proportional to the singles particle cross sections. Let S_i and S_j be the number of counts in the singles particle spectra at the excitation energy bin i and j. The normalization factor n_{ij} is then given by:

$$n_{ij} = \frac{S_j}{S_i}. \tag{4.13}$$

- *Multiplicity normalization:* The average γ-ray multiplicity $\langle M \rangle$ of an excited state of energy E is linked to the average γ-ray energy $\langle E_\gamma \rangle$ [108]:

$$\langle M \rangle = \frac{E}{\langle E_\gamma \rangle}. \tag{4.14}$$

  The average γ-ray multiplicity at a given excitation energy bin i can easily be calculated using Eq. 4.14. The singles particle cross section S_i is proportional to

the ratio $A(u_i)/\langle M_i \rangle$, where $A(u_i)$ corresponds to the total number of counts in the unfolded spectrum u_i. Eq. 4.13 becomes:

$$n_{ij} = \frac{A(u_i)\langle M_j \rangle}{A(u_j)\langle M_i \rangle}. \tag{4.15}$$

The experimental conditions need to be taken into account to decide between the two normalization procedures.

The first generation spectra f_i can be calculated using an iterative procedure [3]. Using the unfolded spectrum, the calculated cross section coefficients n_{ij} and a trial function w_{ij}, the first generation spectra f_i is calculated using Eq. 4.11. New weighting coefficients w_{ij} can be calculated by normalizing the area of the first generation spectra f_i to one. The procedure is repeated until the weighted function converges. A diagram of the first generation spectra extraction is shown in Figure 4.4. Tests of the convergence procedure have been performed using simulated spectra and convergence is obtained within three iterations [3]. Less than 20 iterations are needed on experimental spectra.

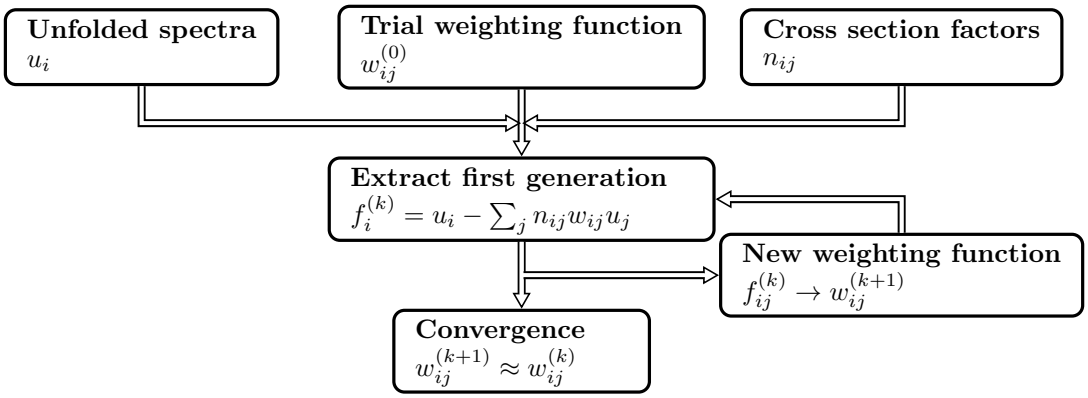

Figure 4.4: Diagram of the first generation spectra extraction.

4.3 Simultaneous extraction of the level density and γ-ray strength function

Following the particle induced reaction, the nucleus is assumed to reach a compound-like system before emitting γ rays. A compound state is created within $\approx 10^{-18}$ s while typical lifetime for states in the quasi-continuum is $\approx 10^{-15}$ s. In the compound nucleus picture, the relative decay probabilities into any particular final state is independent of the way the compound nucleus was formed, and governed by statistical rules. Therefore the decay probability of an excited state is proportional to a transmission coefficient linking the initial and final state times the level density at the final excitation energy $\rho(E_f)$.

According to the Brink-Axel hypothesis described in Sec. 2.2.5, the cross section for photoabsorption has the same energy dependence if the absorption happens on the ground state or an excited state and as long as the dipole selection rule is fulfilled, there is no dependence on the spin value of the initial and final state. Therefore, the γ-ray transmission coefficient $\mathcal{T}$ only depends on the γ ray of energy E_γ and not on the excitation energy. The decay probability $P(E_x, E_\gamma)$ from the excitation energy E_x by emitting a γ ray of energy E_γ can be written as:

$$P(E_x, E_\gamma) \propto \rho(E_f)\mathcal{T}(E_\gamma) \ . \tag{4.16}$$

An iterative procedure is used to extract the level density and the γ-ray transmission coefficient from the first generation matrix as described in Ref. [5]. The first generation matrix is obtained as described in Sec. 4.2. In order for the first generation matrix to represent the decay probability, the sum of the γ-ray emission probability for a given excitation energy bin needs to be normalized to one:

$$\sum_{E_\gamma=E_\gamma^{min}}^{E_x} P(E_x, E_\gamma) = 1, \tag{4.17}$$

where E_γ^{min} is the minimum γ-ray energy considered, and set to 900 keV. Matrix elements below this limit are discarded because of issues associated with the subtraction method used to obtain the first generation matrix. The γ rays considered should only be from the statistical excitation-energy region. From Eq. 4.16, the normalized first generation matrix can be approximated by:

$$P_{th}(E_x, E_\gamma) = \frac{\rho(E_x - E_\gamma)\mathcal{T}(E_\gamma)}{\sum_{E'_\gamma=E_\gamma^{min}}^{E_x} \rho(E_x - E'_\gamma)\mathcal{T}(\mathrm{E}'_\gamma)}, \tag{4.18}$$

where the energy of the final state is written as a function of the excitation energy and the emitted γ-ray energy: $E_f = E_x - E_\gamma$. It can be shown [5], that if ρ and $\mathcal{T}$ are solutions of Eq. 4.18, an infinite number of functions solution can be created using the transformation:

$$\widetilde{\rho}(E_x - E_\gamma) = A\exp[\alpha(E_x - E_\gamma)]\rho(E_x - E_\gamma), \tag{4.19}$$

$$\widetilde{\mathcal{T}}(E_\gamma) = B\exp(\alpha E_\gamma)\mathcal{T}(E_\gamma), \tag{4.20}$$

where A, B, and α are constant parameters. Thus, only the functional form is found by fitting the first generation matrix.

The start of the iterative method to extract the functional form for ρ and $\mathcal{T}$ consist in setting $\rho^{(0)} = 1$, the initial estimate of $\mathcal{T}$ is given by:

$$\mathcal{T}^{(0)}(E_\gamma) = \sum_{E_x=max(E_x^{min},E_\gamma)}^{E_x^{max}} P(E_x, E_\gamma). \tag{4.21}$$

The ρ and $\mathcal{T}$ solutions are found by using a least χ^2 method:

$$\chi^2 = \frac{1}{N} \sum_{E_x=E_x^{min}}^{E_x^{max}} \sum_{E_\gamma=E_\gamma^{min}}^{E_x} \left(\frac{P_{th}(E_x, E_\gamma) - P(E_x, E_\gamma)}{\Delta P(E_x, E_\gamma)} \right)^2, \tag{4.22}$$

where N is the number of degrees of freedom, and $\Delta P(E_x, E_\gamma)$ is the uncertainty in the primary γ-ray matrix. The reduced χ^2 is minimized for all E_γ and $(E_x - E_\gamma)$. The iterations take place here, where previous estimates of the level density and transmission coefficient are used to calculate the derivative of the reduced χ^2, which returns updated values. In order to achieve better convergence, the variation of the level density and transmission coefficient is limited for each iteration to a given percentage of their values:

$$\frac{i^{(n)}}{1+P} \leq i^{(n+1)} \leq i^{(n)}(1+P), \tag{4.23}$$

where $i^{(n)}$ is the n^{th} iteration of the parameter i and P limits the accessible range for i. P is decreased as function of the number of iterations from 20% to 1%.

4.3.1 Normalization of the level density

Only the functional form of the level density and the γ-ray strength function are extracted. In order to determine the parameters α and A from Eq. 4.19, the level density is normalized to the number of known discrete levels at low excitation energy and to neutron resonance data at the neutron separation energy. The known discrete levels are extracted using the NNDC website [103].

The average neutron resonance spacing D_0 corresponding to the level spacing for s-wave neutron excitation is given by Eq. (2.19). Combining Eq. (2.3), giving the spin dependent level density, and (2.19), we obtain the level density at the neutron separation energy as a function of the s-wave level spacing:

$$\rho(S_n) = \frac{2\sigma^2}{D_0} \frac{1}{(I_t+1)\exp[-(I_t+1)^2/2\sigma^2] + I_t \exp[-I_t^2/2\sigma^2]}, \tag{4.24}$$

where I_t is the target spin and σ the spin cutoff parameter.

4.3.2 Normalization of the γ-ray transmission coefficient

Similarly to the level density, an infinite number of transmission coefficient functions are solutions of the extraction procedure and given in Equation 4.20. The parameter α corresponding to the slope of the transmission coefficient is obtained while normalizing the level density. The remaining constant parameter B gives the absolute normalization. Calculation of the normalization parameter using the average total radiative width $\langle \Gamma_\gamma \rangle$

at the neutron separation energy S_n is described in Ref. [109]. The average total radiative width can be written as a function of the transmission coefficient [71]:

$$\langle \Gamma_\gamma(E_x, J, \pi) \rangle = \frac{1}{2\pi\rho(E_x, J, \pi)} \sum_{XL} \sum_{J_f, \pi_f} \int_{E_\gamma=0}^{E_x} dE_\gamma \mathcal{T}_{XL}(E_\gamma) \rho(E_x - E_\gamma, I_f, \pi_f), \quad (4.25)$$

where $\langle \Gamma_\gamma(E_x, J, \pi) \rangle$ is the average total radiative width of levels at the excitation energy E_x, with spin J and parity π. The integration is taken over γ-ray energies E_γ between 0 and the excitation energy E_x. The summation is taken over all electromagnetic character X and multipolarity L for a γ ray de-exciting to a final level of given spin J_f and parity π_f. If we assume that the main contribution to the experimental transmission coefficient $\mathcal{T}$ is from dipole radiation (L=1), we obtain:

$$B\mathcal{T}(E_\gamma) = B \sum_{XL} \mathcal{T}_{XL}(E_\gamma) \approx B[\mathcal{T}_{E1}(E_\gamma) + \mathcal{T}_{M1}(E_\gamma)]. \quad (4.26)$$

The γ-ray strength function f assuming pure dipole radiation is given by:

$$f(E_\gamma) = \frac{1}{2\pi E_\gamma^3} B\mathcal{T}(E_\gamma). \quad (4.27)$$

The average total radiative width measured for s-wave neutron capture on states with spin $I_t \pm 1/2$, where I_t is the ground state spin of the target, is given by combining Equations (4.25) and (4.26):

$$\langle \Gamma_\gamma(S_n, I_t \pm 1/2, \pi_t) \rangle = \frac{1}{2\pi\rho(S_n, I_t \pm 1/2, \pi_t)} \sum_{I_f} \int_0^{S_n} dE_\gamma B\mathcal{T}(E_\gamma) \rho(S_n - E_\gamma, I_f), \quad (4.28)$$

where π_t is the parity of the target nucleus. The summation is performed over all final levels with spin I_f that are accessible via $E1$ or $M1$ transitions with energy E_γ. The same number of accessible levels with positive and negative parity is assumed. Using the intrinsic spin distribution g given in Equation (5.2), and using Equation (2.3) to introduce D_0, we obtain:

$$\langle \Gamma_\gamma(S_n, I_t \pm 1/2, \pi_t) \rangle = \frac{D_0}{2\pi} \int_0^{S_n} dE_\gamma B\mathcal{T}(E_\gamma) \rho(S_n - E_\gamma) \sum_{J=-1}^{1} g(S_n - E_\gamma, I_t \pm 1/2 + J). \quad (4.29)$$

Chapter 5

Experimental results

The level density and γ-ray strength function of ^{243}Pu have been extracted using the Oslo method described in Chaper 4. An enhancement of the γ-ray strength function is seen in the 1.5-3.5 MeV energy range and interpreted as the scissors resonance. Its centroid and strength are compared to the sum rule estimate. Finally, the measured level density and strength function are used as input in Hauser-Feshbach calculations in order to estimate the ^{242}Pu(n,γ) cross section.

5.1 From the raw particle-γ-ray matrix to the first generation matrix

The raw particle-γ-ray matrix giving the γ-ray spectra as a function of the excitation energy of ^{243}Pu is shown in Figure 5.1. It is obtained after calibration of the NaI detectors and the SiRi array as discussed in Chapter 3, and is the starting point of the Oslo method. For ^{243}Pu, the neutron separation energy is $S_n = 5.034$ MeV, the proton separation is $S_p = 6.95$ MeV, and the fission barrier is $B_f \approx 6$ MeV. To make sure there are only γ rays from ^{243}Pu, only γ-ray spectra for excitation energies below the neutron separation energy will be used to extract the level density and γ-ray strength function. For γ rays spectra for excitation energies below the neutron separation energy, the first state of ^{17}O is populated via the (d,p) reaction and emits a 871 keV γ ray. This peak is not an issue because only γ rays above 900 keV will be taken into account to extract the level density and γ-ray strength function. The first excited state of ^{10}Be is also populated but decays back to the ground state via internal conversion only. In Figure 5.1, large contamination peaks from population of ^{17}O and ^{10}Be can be observed for excitation energies above the neutron separation energy.

The raw matrix is unfolded using the known detector response following the procedure detailed in Section 4.1. Each unfolded spectrum is calculated by iteratively folding a trial spectrum until agreement is found with the measured spectrum. Figure 5.2 shows the measured, unfolded and folded spectra for a 16 keV wide channel at the excitation energy

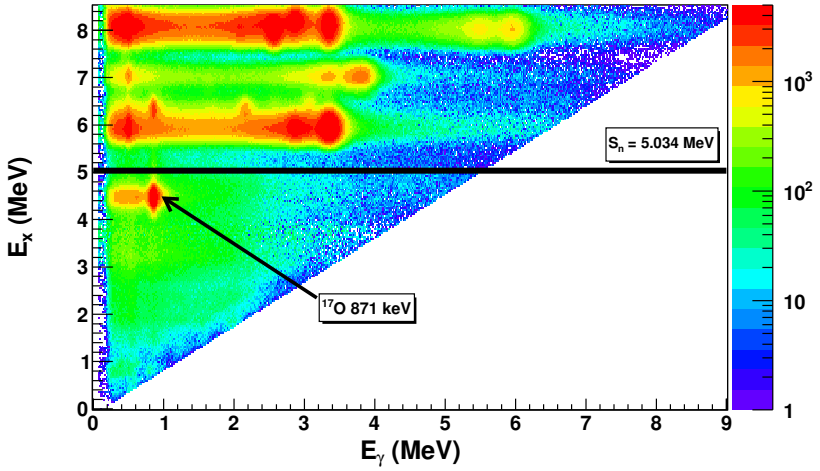

Figure 5.1: ^{243}Pu raw particle-γ-ray matrix.

$E_x = 4.1$ MeV in ^{243}Pu. The folded spectrum agrees very well with the measured one, except for the very low γ-ray energy part below 200 keV. A threshold of 400 keV is chosen to extract the first generation matrix. Figure 5.3 shows the unfolded coincident particle-γ-ray matrix for ^{243}Pu. The z-axis represents the number of counts per $E_\gamma = 16$ keV, $E_x = 41$ keV bins. For each excitation energy bin, the γ-ray spectrum has been unfolded. The massive peak centered at $(E_\gamma, E_x) = (0.87, 4.5)$ MeV comes from population of the first excited state of ^{17}O and is removed before proceeding to the extraction of the first generation spectrum.

The first generation γ-ray matrix is extracted following the procedure described in Section 4.2. The coefficient n_{ij} from Eq. (4.12) can be calculated by two different normalization procedures: using singles from the particle spectrum and Eq. (4.13), or using the γ-ray multiplicity and Eq. (4.15). The experimental conditions need to be taken into account to decide between the two normalization procedures. The ΔE vs E spectrum presented in Figure 3.7 shows contamination peaks from the (d, p) reaction on ^{9}Be and ^{16}O. Amongst the known contaminants, the only measured γ rays in the excitation energy range of interest (below the neutron separation energy), are from the decay of the first excited state of ^{17}O. The feature has been subtracted from the unfolded particle-γ ray spectrum. This feature is difficult to remove from the singles particle spectrum because of its magnitude compare to the signal of interest.

The singles normalization is sensitive to contaminants that don't emit γ rays, therefore, the multiplicity normalization is chosen. Figure 5.4 shows the first generation spectra obtained using the singles normalization (red) or the multiplicity normalization (black) for three different energies. The agreement is excellent for $E_\gamma > 1$ MeV but poor at lower γ-ray energies. The probable cause of this disagreement could be contamination in the singles spectrum, mostly (d, p) to the ground state of ^{10}Be. The other three contamination

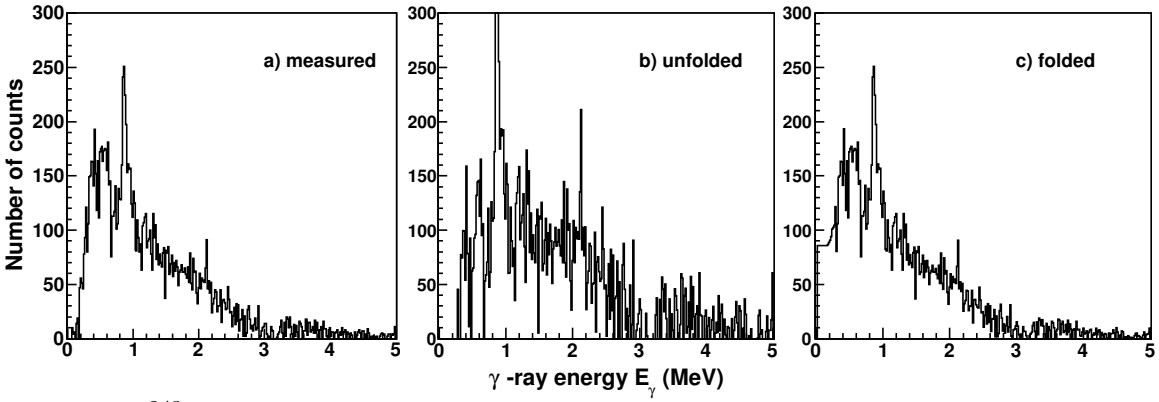

Figure 5.2: ^{243}Pu measured (a), unfolded (b), and folded (c) γ-ray spectra for a 16 keV wide energy bin at the excitation energy $E_x = 4.1$ MeV.

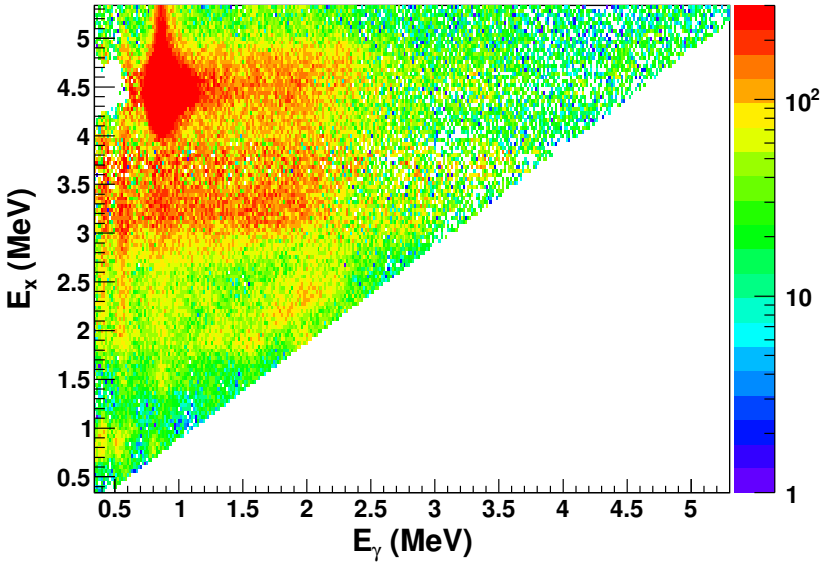

Figure 5.3: ^{243}Pu unfolded particle-γ-ray coincident matrix. The massive peak centered at $(E_\gamma, E_x) = (0.87, 4.5)$ MeV comes from population of the first excited state of ^{17}O.

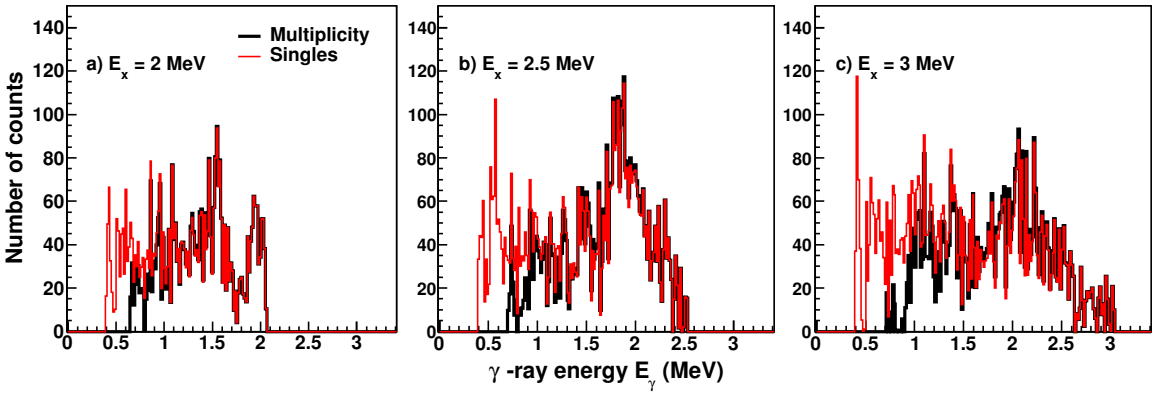

Figure 5.4: Comparison of the first generation spectra obtained using the singles normalization (red) or the multiplicity normalization (black) for a 41 keV bin in excitation energy at the following excitation energies: 2 MeV (a), 2.5 MeV (b) and 3 MeV (c).

peaks appear at higher excitation energies. Some low energy γ rays are not subtracted correctly, even with the multiplicity normalization. This could be due to some strong low energy transitions which probability to be populated through γ decay is higher than via the (d, p) reaction. For the extraction of the level density and strength function described in Sec. 4.3, only γ rays with energy $E_\gamma > 900$ keV are considered.

Figure 5.5 shows the γ-ray multiplicity as a function of the excitation energy for ^{243}Pu. Only γ-rays with energy greater than 400 keV are taken into account. Below 2 MeV, the multiplicity shows oscillations, indicating a non-statistical behavior of the decay process at low excitation energies. Above 4.5 MeV, the multiplicity fluctuates due to the opening of the fission and neutron emission channels. The extraction of the level density and γ-ray strength function is only applied for the excitation energy range $E_x = 2.6 - 4.3$ MeV. The extracted first generation spectrum for ^{243}Pu is shown in Figure 5.6. The red contour shows the limits for the extraction of the level density and γ-ray strength function.

5.2 Extraction of level density and γ-ray transmission coefficient

The level density and γ-ray transmission coefficient functional forms are simultaneously extracted from the primary γ-ray matrix using the algorithm described in Section 4.3, over the excitation energy range $E_x = 2.6 - 4.3$ MeV and for γ rays with energy $E_\gamma > 900$ keV. Figure 5.7 shows the normalized first generation matrix, $P(E_x, E_\gamma)$, and the theoretical expectation $P_{th}(E_x, E_\gamma)$. The bin size is 123 keV, both in excitation energy and γ-ray energy. Figure 5.8 shows the same comparison for given excitation energy bins, giving confidence in the extraction method.

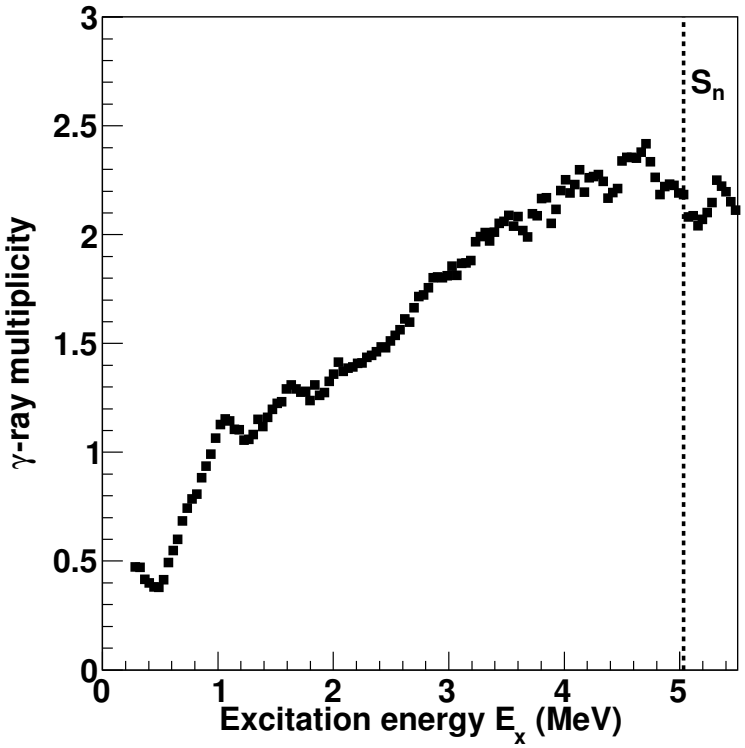

Figure 5.5: γ-ray multiplicity calculated using Eq. 4.14 as a function of the excitation energy for ^{243}Pu.

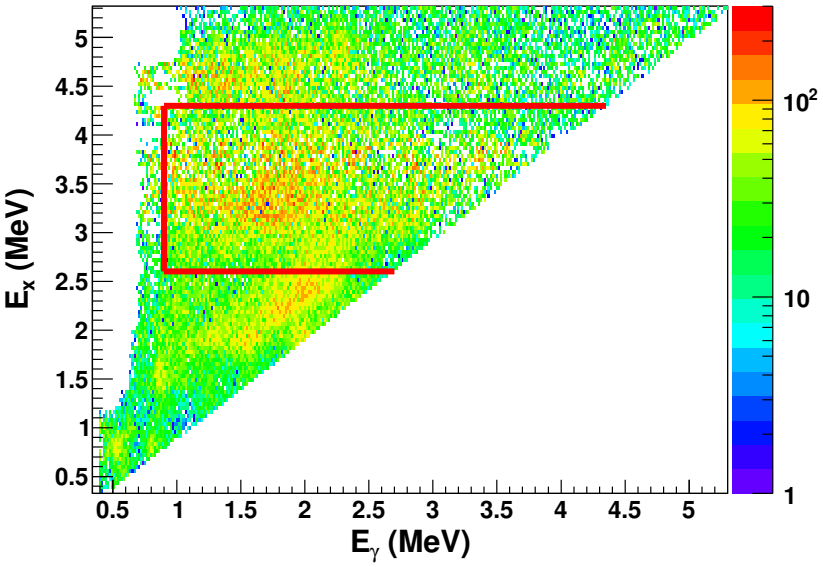

Figure 5.6: ^{243}Pu first generation matrix.

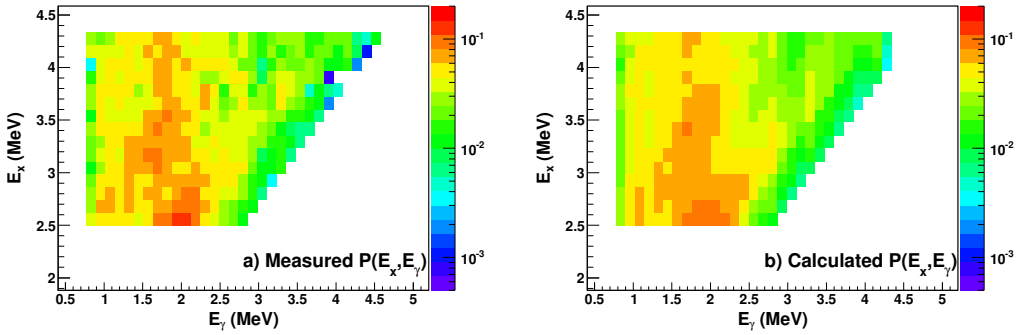

Figure 5.7: Comparison between the experimental first generation matrix $P(E_x, E_\gamma)$ (a) and the calculated one (b) using the iteration procedure from Ref. [5] for ^{243}Pu.

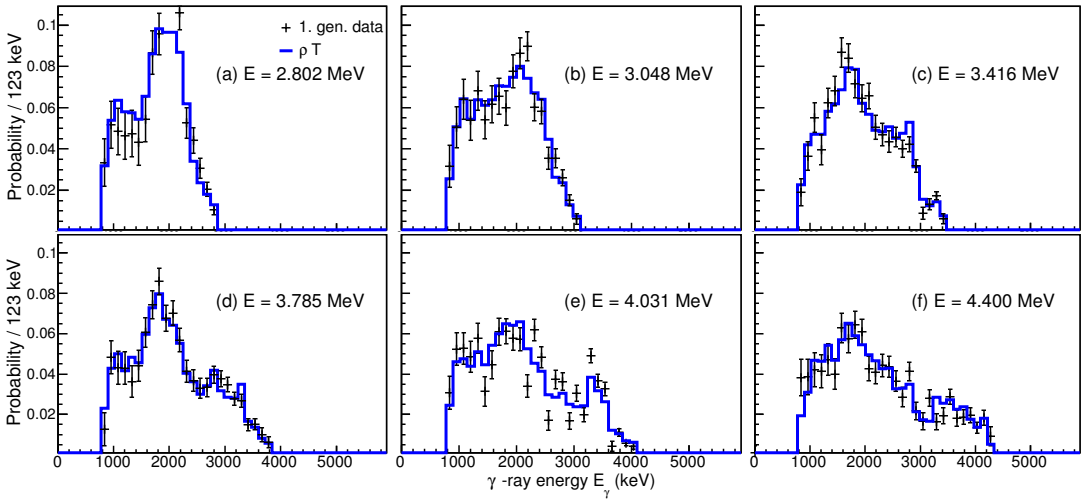

Figure 5.8: Comparison between the experimental first generation matrix (black crosses) and the calculated one (blue lines) for a given excitation energy bin.

5.3 Normalization of the level density

Only the functional form of the level density and the γ-ray strength function are extracted. The level density is normalized to the number of known discrete levels at low excitation energy and to neutron resonance data at the neutron separation energy. The normalization procedure is described in Section 4.3.1.

At the neutron separation energy, assuming that both parities contribute equally, the level density is given by Eq. (4.24). For ^{243}Pu, the target spin is $I_t(^{242}\mathrm{Pu}) = 0$ and the level density at the neutron separation energy is given by:

$$\rho(S_n, I_t = 0) = \frac{2\sigma^2}{D_0} \frac{1}{\exp[-1/2\sigma^2]}. \tag{5.1}$$

Several D_0 values are reported in the literature for ^{243}Pu. In his atlas of neutron resonances[110], Mughabghab reports $D_0 = 17(1)$ eV. In their measurement of the total and absorption neutron cross sections of ^{242}Pu, Young and Reeder [111] quote $D_0 = 16.5$ eV, without uncertainties. Rich *et al.* recently modeled reaction cross sections on several Pu isotopes [112]. Using the ESTIMA code, they obtain $D_0 = 16.8(5)$ eV. The RIPL-3 evaluation by Ignatyuk [25] gives $D_0 = 13.5(15)$ eV, which is inconsistent with the other work. In this analysis, the $D_0 = 17(1)$ eV value from Mughabghab is taken to normalize the level density.

The following spin distribution, g, of the level density is assumed [113]:

$$g(E_x, J) = \frac{2J+1}{2\sigma^2} \exp\left[-\frac{(J+1/2)^2}{2\sigma^2}\right], \tag{5.2}$$

Table 5.1: Parameters used to extract the level density of ^{243}Pu given for the two different parametrization from von Egidy and Bucurescu.

Ref.	S_n (MeV)	a (MeV^{-1})	E1 (MeV)	$\sigma(S_n)$	D_0 (eV)	$\rho(S_n)$ (10^6MeV^{-1})	T_{CT} (MeV)	E_0 (MeV)
EB06[a]	5.034	25.82[a]	-0.45[a]	8.15[a]	17(1)[c]	7.87(163)	0.40(1)	-0.95(16)
EB09[b]	5.034	23.96[b]	-0.22[b]	5.11[b]	17(1)[c]	3.13(64)	0.44(1)	-1.19(16)

[a]Estimated from systematics [18].
[b]Estimated from systematics [19].
[c]Reference [110].

where J is the spin of the different levels. The spin cutoff parameter σ is determined from the global systematic study of level density parameters by von Egidy and Bucurescu, using a rigid-body moment of inertia [18]. Another parametrization of the spin cutoff parameter by the same authors is available [19]. The second parametrization gives consistently a lower spin cutoff parameter. It is more suitable for light nuclei, while the first parametrization should be used for heavier nuclei, particularly actinides. The level density shown in Figure 5.9 is normalized using the two different parametrizations given in Table 5.1. The black squares correspond to the extraction of the level density using the spin cutoff parameter from Ref. [19] and the red squares using the spin cutoff parameter from Ref. [18]. Both normalizations extrapolate the measurements to the neutron separation energy using the constant temperature model presented in Sec. 2.1.1, represented by the dashed lines on the figure, given by the equation:

$$\rho_{CT}(E_x) = \frac{1}{T_{CT}} \exp \frac{E_x - E_0}{T_{CT}}, \tag{5.3}$$

where T_{CT} represents the slope of the level density with a shift in excitation energy E_0, and are given in Table 5.1. The spin cutoff parametrization from Ref. [18] (red squares) is more suitable for actinides and is considered to be the correct one in the following analysis. Results from Ref. [19] are given as a comparison and show the impact of the spin cutoff parameter on the level density at the neutron separation energy (more than a factor of two).

Because we only apply the Oslo method from 2.6 to 4.3 MeV of excitation energy, we need to extrapolate the level density to the normalization data point at the neutron binding energy. The Fermi-gas (FG) and constant temperature (CT) models (see Sec. 2.1.1) are the two most used semi-empirical models to describe the level density. Figure 5.10 shows the extracted level density if we assume a Fermi-gas (black squares) or a constant temperature (red squares) dependence of the level density. Comparing the reduced chi-square fit value evaluated between $E_x = 0.5$ and 3.4MeV, the constant temperature model gives a better description of the measured data. All other measurements in the actinide region [6, 114] confirm a constant temperature dependence of the level density rather than a Fermi-gas dependence. The interpretation of the constant temperature model is that the

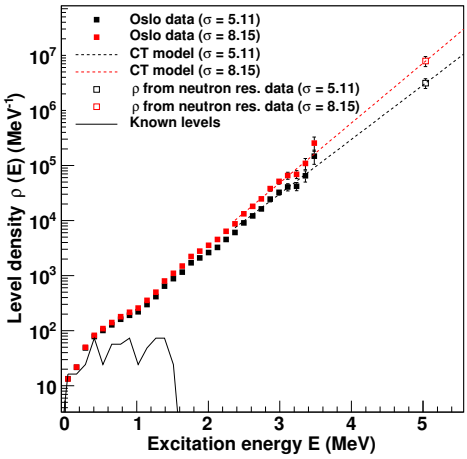

Figure 5.9: ^{243}Pu nuclear level density measured with the Oslo method (squares). The extraction has been realized normalizing to known levels at low excitation energy and to the level density calculated from neutron resonance data at the neutron separation energy (using a spin cutoff parameter $\sigma = 5.11$ for the black data points and $\sigma = 8.15$ for the red data point). Extrapolation of the data up to the neutron separation energy is done using the constant temperature model.

excitation energy goes into breaking Cooper pairs similarly to a first order phase transition in thermodynamics [115]. On the contrary, the Fermi-gas model considers the nucleus as a gas of fermions. The present results provide empirical support for the importance of pairing in the energetics of the nucleus.

5.4 Normalization of the γ-ray transmission coefficient and extraction of the γ-ray strength function

The normalization procedure for the γ-ray transmission coefficient is described in Section 4.3.2.

The constant coefficient B is calculated using the previous equation with $\left\langle \Gamma_\gamma^{^{243}\mathrm{Pu}}(S_n) \right\rangle = 22(1)$ meV [110]. Though, from the first generationγ-ray matrix, only γ rays with energy $E_\gamma > 900\,\mathrm{keV}$ are considered and the level density and transmission coefficient are only extracted up to $E_x = 4.3\,\mathrm{MeV}$. The transmission coefficient is extrapolated for $E_\gamma < 900\,\mathrm{keV}$ and $E_\gamma > 4.3$ MeV with exponential functions as shown in Figure 5.11.

The determination of B using Equation 4.29 is in general sufficient to extract a reliable γ-ray strength function [109, 116, 117] for medium-mass nuclei. For actinides, some corrections need to be taken into account otherwise this method will yield an unphysical γ-ray

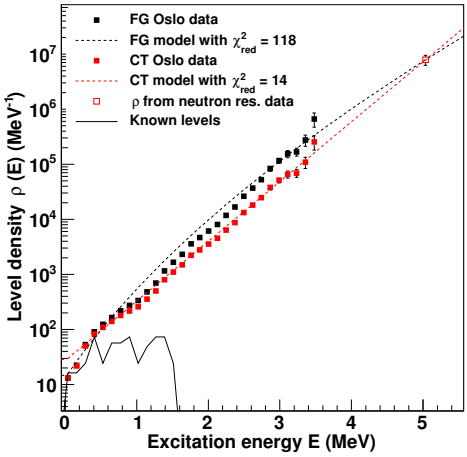

Figure 5.10: Comparison of the ^{243}Pu experimental level density with the constant temperature (CT) and Fermi-gas (FG) level density formulas.

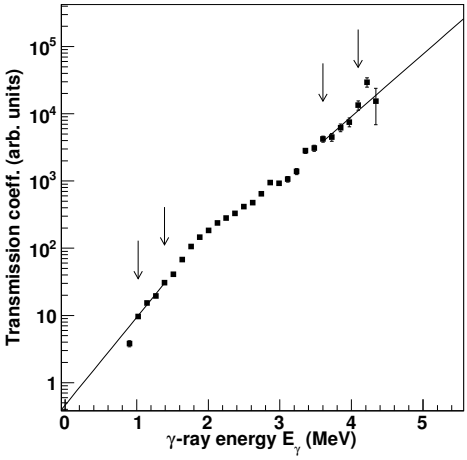

Figure 5.11: ^{243}Pu transmission coefficient. The data point between the arrows at low and high γ-ray energies is used to fit the exponential extrapolation functions.

strength function. Situated far from closed shells, the level density of actinides rapidly increases with excitation energy because of a high density of single particle orbitals. The spin distribution is broad at the neutron separation energy and the (d, p) reaction will not populate the highest spins available in the nucleus. The transmission coefficient is assumed to be independent of spin but the shape of the observed primary γ-ray matrix should be influenced by not populating all the available levels. Therefore, the primary γ-ray matrix should be fitted by the product of the transmission coefficient and a reduced level density accounting only for the levels populated by the reaction. Because the determination of the parameter B depends on the level density (see Equation 4.29), which is dependent of the spin-cutoff parameter and our estimation of the relative amount of states populated by the (d, p) reaction, it is rather uncertain. The strength function can be written as a function of the transmission coefficient as in Equation4.27, or as a function of the photonuclear cross section $\sigma(E_\gamma)$:

$$f(E_\gamma) = \frac{1}{3\pi^2\hbar^2c^2}\frac{\sigma(E_\gamma)}{E_\gamma}. \tag{5.4}$$

Strength function measurements using (γ, x) reactions are available for excitation energies greater than the neutron separation energy and fit parameters of the Giant Electric Dipole Resonance (GEDR) are available on the RIPL website [25]. Unfortunately there are no measured γ-ray strength function data for ^{243}Pu. Only measurements for the ^{239}Pu isotope exists. We assume that the $E1$ strength does not vary much from ^{239}Pu to ^{243}Pu. This assumption is supported by the classical Thomas-Reiche-Kuhn sum rule for $E1$ strength [118, 119, 120] and experimentally observed between ^{236}U and ^{238}U [8].

Figure 5.12 shows our best interpretation of the experimental γ-ray strength function. The γ-ray strength function derived from ^{239}Pu(γ, x) data from Berman *et al.* [121], Gurevitch *et al.* [79] and Moraes *et al.* [122] are shown and fitted with two enhanced generalized Lorentzians (EGLO) as defined in RIPL [25] but with a constant-temperature parameter of final states T_f suggested by the constant-temperature dependence of the level density. This temperature taken to be the same as the one describing the level density influences the slope of the low γ-ray energy part of the strength function and is used as a base line for our extracted γ-ray strength function, since the γ-ray strength function extracted via the Oslo method in this work covers γ-ray energies from 900 keV up to 4.3 MeV while the lowest energy point for (γ, x) data is 6.7 MeV.

To describe the structure around $E_\gamma = 7.5$ MeV, a resonance described by a standard Lorentzian without damping (SLO described in Section 2.2.4) is added (labeled pygmy2 in Figure 5.12). To take into account the sharp rise of our data for $E_\gamma = 3 - 4$ MeV, another resonance is postulated at $E_\gamma = 4.4$ MeV and labeled pygmy1. To match the slope determined by the constant-temperature, the γ-ray strength function data are extracted assuming a level density at the neutron separation energy reduced from 7.87 to 3.94 million levels per MeV. This correspond to only populating half of the available levels using the (d, p) reaction. A similar reduction factor of $\approx 1/2$ has been postulated for the extraction of the γ-ray strength function of ^{232}Th [8] and ^{238}Np [114]. Calculations of the

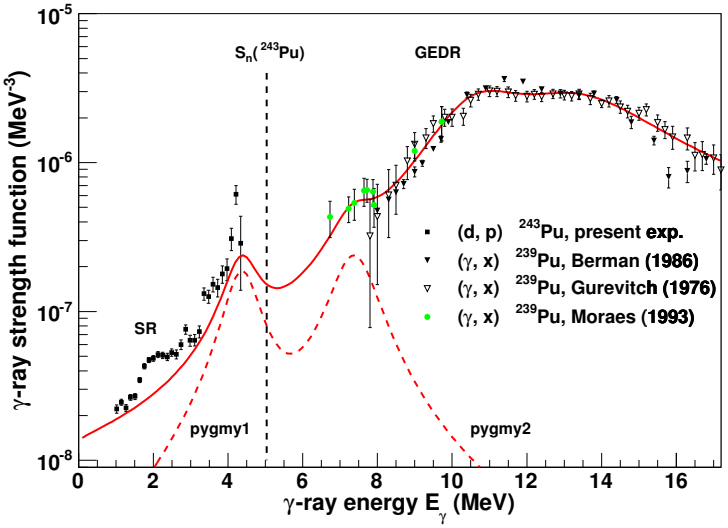

Figure 5.12: Experimental γ-ray strength function from the present $(d, p\gamma)^{243}$Pu experiment. The black filled triangles, empty triangles and green dots are ^{239}Pu(γ, x) data from respectively Berman *et al.*[121], Gurevitch *et al.*[79] and Moraes *et al.*[122]. The red curve is the estimated underlying $E1$ γ-ray strength function. The structure for $E_\gamma = 1-3.5$ MeV is interpreted as the scissors resonance. Figure taken from Ref. [123].

ratio of spins populated are presented in Appendix B. All the parameters used to obtain the estimated underlying $E1$ γ-ray strength function (red curve in Figure 5.12) are given in Table 5.2.

5.4.1 The scissors resonance

The experimental γ-ray strength function shown in Figure 5.12 exhibits extra strength from the expected base line (red curve) for $E_\gamma = 1.5-3.5$MeV. Figure 5.13 shows the extra strength when the base line is subtracted. A similar structure has been observed in all actinides measured at Oslo[8, 114] and is interpreted as the scissors resonance described in Section 2.2.3. The scissors resonance is fitted with two Lorentzian distributions. Table 5.3 lists the resonances centroid ω_i, cross section σ_i and width Γ_i. The integrated strength $B_{\mathrm{SR},i}$, for each resonance i is given by:

$$B_{\mathrm{SR},i} = \frac{9\hbar c}{32\pi^2}\left(\frac{\sigma_i \Gamma_i}{\omega_i}\right). \tag{5.5}$$

The total strength of the scissors resonance is obtained by adding the strength from the two resonances:

$$B_{\mathrm{SR}} = \sum_i B_{\mathrm{SR},i}. \tag{5.6}$$

Table 5.2: Parameters used to estimate underlying $E1\gamma$-ray strength function (red curve in Figure 5.12). The Giant electric dipole resonance (GEDR) is described by two EGLO distributions, characteristic of deformed nuclei) with constant temperature T_f obtained from the description of the level density. Pygmy1 and pygmy2 are described with standard Lorentzian distributions. ω, σ, and Γ are respectively the centroid, the cross section and the width of a given resonance.

GEDR						
$\omega_{E1,1}$ (MeV)	$\sigma_{E1,1}$ (mb)	$\Gamma_{E1,1}$ (MeV)	$\omega_{E1,2}$ (MeV)	$\sigma_{E1,2}$ (mb)	$\Gamma_{E1,2}$ (MeV)	T_f (MeV)
11.1	290	3.2	14.2	340	5.5	0.40(1)

pygmy1		
ω_{pyg1} (MeV)	σ_{pyg1} (mb)	Γ_{pyg1} (MeV)
4.4(1)	9(3)	1.0(2)

pygmy2		
ω_{pyg2} (MeV)	σ_{pyg2} (mb)	Γ_{pyg2} (MeV)
7.4(3)	20(6)	1.3(3)

The average centroid ω_{SR} is taken as the strength weighted average of the two resonances:

$$\omega_{\mathrm{SR}} = \frac{\sum_i \omega_i B_{\mathrm{SR},i}}{\sum_i B_{\mathrm{SR},i}}. \tag{5.7}$$

The total resonance strength B_{SR} and centroid ω_{SR} of the scissors resonance can be calculated using the sum rule approach presented in Section 2.2.3. The ground state moment of inertia (appropriate to describe the scissors resonance build on the ground state) was replaced by the rigid body moment of inertia Θ_{rigid} (appropriate to describe the scissors resonance in the quasi-continuum), given by:

$$\Theta_{\mathrm{rigid}} = \frac{2}{5} m_N r_0^2 A^{5/3}(1 + 0.31\delta), \tag{5.8}$$

where $m_N = 939$ MeV is the nucleon mass, $r_0 = 1.15$ fm is the nucleon radius, A is the number of nucleons and δ is the nuclear quadrupole deformation. The m_1 and m_{-1} moments are given by:

$$m_1 = \frac{3}{8\pi}\Theta_{\mathrm{rigid}}\delta^2\omega_D^2(g_p - g_n)^2\xi \quad \left[\mu_N^2\mathrm{MeV}\right], \tag{5.9}$$

$$m_{-1} = \frac{3}{16\pi}\Theta_{\mathrm{rigid}}(g_p - g_n)^2 \quad \left[\mu_N^2\mathrm{MeV}^{-1}\right], \tag{5.10}$$

where $g_p \approx 2Z/A$ and $g_n \approx 0$ are the gyromagnetic factors for respectively protons and neutrons [124]. Z is the number of protons in the nucleus. ξ is a reduction factor given by:

$$\xi = \frac{\omega_Q^2}{\omega_D^2 + \omega_Q^2}, \tag{5.11}$$

which depends on the energy centroid of the isovector giant dipole resonance ω_D and the isoscalar giant quadrupole resonance ω_Q approximated by [60]:

$$\omega_D = (31.2A^{-1/3} + 20.6A^{-1/6})(1 - 0.61\delta) \quad [\text{MeV}]\,, \tag{5.12}$$

$$\omega_Q = 64.7A^{-1/3}(1 - 0.3\delta)) \quad [\text{MeV}]\,. \tag{5.13}$$

The sum rule gives:

$$\omega_{\text{SR}} = \sqrt{\frac{m_1}{m_{-1}}} = \delta\omega_D\sqrt{2\xi}, \tag{5.14}$$

$$B_{\text{SR}} = \sqrt{m_1 m_{-1}} = \frac{3}{4\pi}\left(\frac{Z}{A}\right)^2 \Theta_{\text{rigid}}\delta\omega_D\sqrt{2\xi}. \tag{5.15}$$

The nuclear quadrupole deformation parameter δ is calculated using ground state deformation parameter, β_2. The two quantities are to lowest order proportional [124]:

$$\delta \approx \beta_2\sqrt{\frac{45}{16\pi}}. \tag{5.16}$$

In order to calculate the centroid and the strength using the sum rule estimate, the ground state deformation value is taken as the average of the RIPL-3 [25] tabulated value for ^{242}Pu and ^{244}Pu ($\beta_2 = 0.29$) and from results of a Hartree-Fock-Bogoliubov calculation [125] ($\beta_2 = 0.28$). The centroid of the isovector dipole resonance calculated using the empirical equation (5.12) gives $\omega_D = 11.06$ MeV. Using the GEDR parameters from Table 5.2, the strength weighted average gives $\omega_D = 13.00$ MeV. Table 5.3 gives the experimental scissors resonance strength and centroid as well as the ones calculated using the sum rule. The agreement between our measurement and the sum rule estimate is within the uncertainty range.

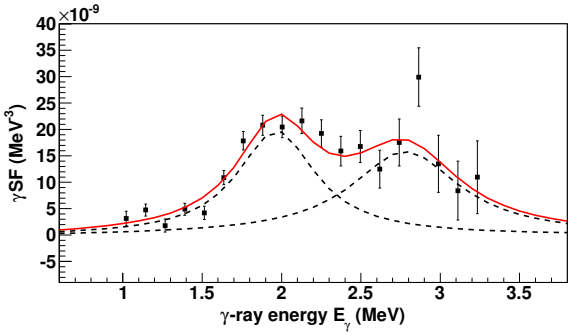

Figure 5.13: The observed scissors resonance for ^{243}Pu. The strength is obtained by subtracting the underlying tail of the GEDR and the two pygmy resonances from Figure 5.12. The scissors resonance is described by two standard Lorentzian distributions whose parameters are given in Table 5.3.

Table 5.3: Parameters used to estimate the centroid and strength of the scissors resonance. The extra strength was fit with two standard Lorentzian distributions. ω, σ, and Γ are respectively the centroid, the cross section and the width of a given resonance. Parameters used for the sum rule estimate are given in the bottom table.

Experimental							
$\omega_{\mathrm{SR},1}$ (MeV)	$\sigma_{\mathrm{SR},1}$ (mb)	$\Gamma_{\mathrm{SR},1}$ (MeV)	$\omega_{\mathrm{SR},2}$ (MeV)	$\sigma_{\mathrm{SR},2}$ (mb)	$\Gamma_{\mathrm{SR},2}$ (MeV)	$\omega_{\mathrm{SR}}^{\mathrm{exp}}$ (MeV)	$B_{\mathrm{SR}}^{\mathrm{exp}}$ (μ_N^2)
1.99(4)	0.45(6)	0.60(8)	2.81(5)	0.51(8)	0.83(14)	2.42(5)	10.1(15)

Sum rule estimate						
δ	ω_D (MeV)	ω_Q (MeV)	ξ	Θ_{rigid} (μ_N^2.MeV^{-1})	ω_{SR} (MeV)	B_{SR} (μ_N^2)
0.27	13.0	9.5	0.21	131	2.3	10.6

5.5 Influence of the spin population from the (d, p) reaction

As mentioned in Section 4.3.2, not all available spins in ^{243}Pu are populated by the (d, p) reaction. Because the γ-ray strength function is simultaneously extracted along with the level density, the level density should be normalized to the populated level density and not to the intrinsic level density of ^{243}Pu. Our data covers the γ rays with energies from 900 keV up to 4.3 MeV while the lowest energy point for (γ, x) data is 6.7 MeV. It is, therefore, difficult to correctly interpolate between those two points. In the case of ^{238}Np, (γ, x) data are available for energies above the neutron separation energy while the γ-ray strength function in Ref. [114] is extracted for energies up to the neutron separation energy. No interpolation was needed and the level density was reduced by a factor of $\approx 1/2$. In our best estimate presented in Figure 5.12.

Appendix B presents a calculation using the EMPIRE code [126] used to estimate the relative amount of levels populated. Table B.2 suggests that only 29% of the levels in ^{243}Pu are populated by the (d, p) reaction. Figure 5.14 shows the extracted γ-ray strength function and estimated underlying $E1$ γ-ray strength function when we assume that all levels (black), half the levels (red) or 29% of the levels (blue) are populated by the (d, p) reaction. The parameters used for the resonance postulated at 4.4 MeV are given in Table 5.4 along with the temperature responsible for the slope of the low energy tail of the GEDR.

Table 5.4: Parameters used to describe the resonance at $E_\gamma = 4.4$ MeV and the temperature of final state giving the slope of the low energy tail of the GEDR when the γ-ray strength function is extracted assuming different amount of levels populated.

Levels populated (%)	ω_{pyg1} (MeV)	σ_{pyg1} (mb)	Γ_{pyg1} (MeV)	T_f (MeV)
100	4.4	12.5	1.05	0.33
50	4.4	9	1.0	0.40
29	4.4	7	1.0	0.44

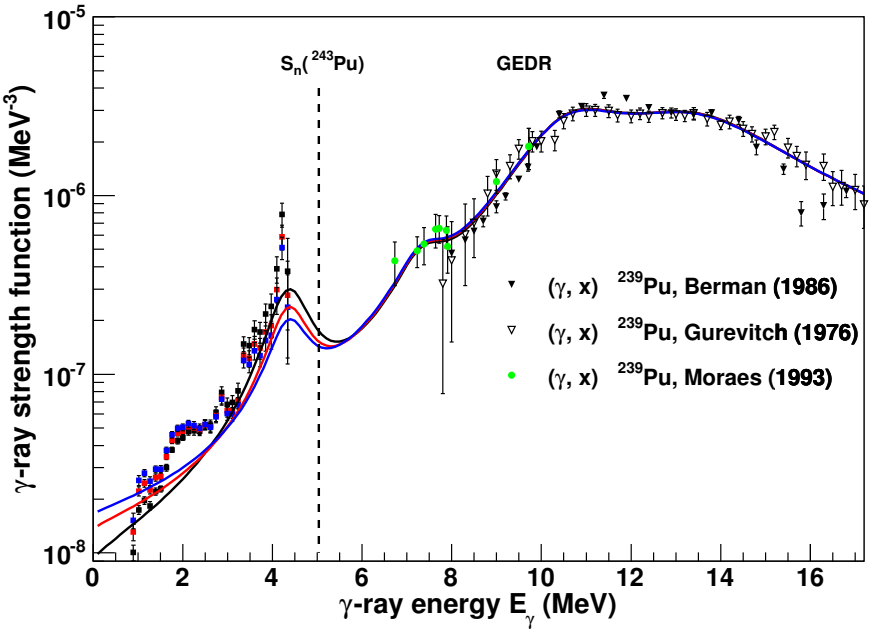

Figure 5.14: The γ-ray strength function is extracted assuming all levels are populated (black squares), half the levels are populated (red squares) or 29% of the levels are populated (blue squares). The curves represent the estimated underlying $E1\gamma$-ray strength function.

As shown in Figure 5.15, independently of the amount of levels populated, some extra strength is present in the γ-ray energy range 1.5-3.5 MeV and is interpreted as the scissors resonance. The absolute strength is slightly smaller when all levels or only 29% of the levels are assumed to be populated than when 50% of the levels are populated, but within the uncertainty range.

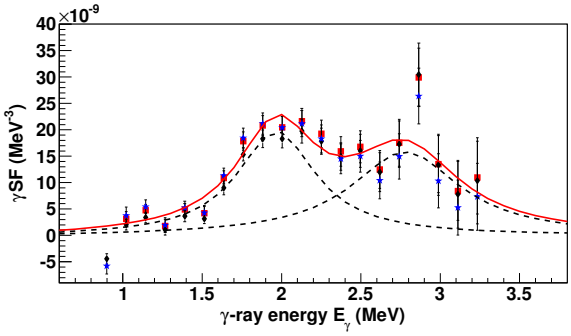

Figure 5.15: Extra strength function above the estimated underlying $E1\gamma$-ray strength function and interpreted as the scissors resonance assuming all levels are populated (black diamonds), half the levels are populated (red squares) or 29% of the levels are populated (blue stars). The red curve is the estimated scissors resonance when half the levels are populated.

5.6 Estimation of the ^{242}Pu(n,γ) cross section

Neutron capture cross sections are well reproduced by Hauser-Feshbach calculations using the level density and γ-ray strength function measured using the Oslo method as inputs [102, 114, 127]. Thus, this technique represents a true alternative to the extraction of neutron capture cross sections with the traditional surrogate method that overestimates the cross section by several times due to spin hindrance [128].

The nuclear reaction code TALYS-1.6 [26] is used to calculate the ^{242}Pu(n,γ) cross section. The level density and γ-ray strength function of ^{243}Pu measured in this work have been used as input parameters. In this section, a brief overview of TALYS is given and results of a TALYS calculation from Ref. [114] are shown and serve as a validation case for the TALYS code ability to calculate neutron capture cross sections in actinides. The level densities and γ-ray strength functions of ^{243}Pu used in the evaluations of the ^{242}Pu neutron capture cross section by major databases are compared to our measurements, followed by a comparison of the ^{242}Pu(n,γ) cross section.

5.6.1 TALYS-1.6

TALYS is a nuclear reaction simulation computer code system. It is intended to simulate nuclear reactions induced by photons, neutrons, protons, deuterons, ^{3}He and α particles in the 1 keV to 200 MeV energy range, and for target nuclides of at least mass 12. It can be used as a tool for analysis of nuclear reaction experiments. Using experimental results, the nuclear models used were constrained, therefore allowing better predicting power. It remains a work in progress as more experimental data will allow to constrain the models further. TALYS can also be used as a tool to predict nuclear data when no

measurements are available. This is crucial for a broad range of applications, in areas like nuclear power reactors, fusion reactors, transmutation of radioactive waste, medical applications, homeland security, and astrophysics.

Figure 5.16 shows a schematic of the different reactions mechanism that can occur during an arbitrary nucleon-induced reaction. Despite the simplicity of the schematic, TALYS does not only calculate the outcome of a particular reaction; the decay of all residual nuclei created during the reaction are calculated following the same model. Figure 5.17 gives an overview of the nuclear models present in TALYS, associated with the different reaction mechanisms.

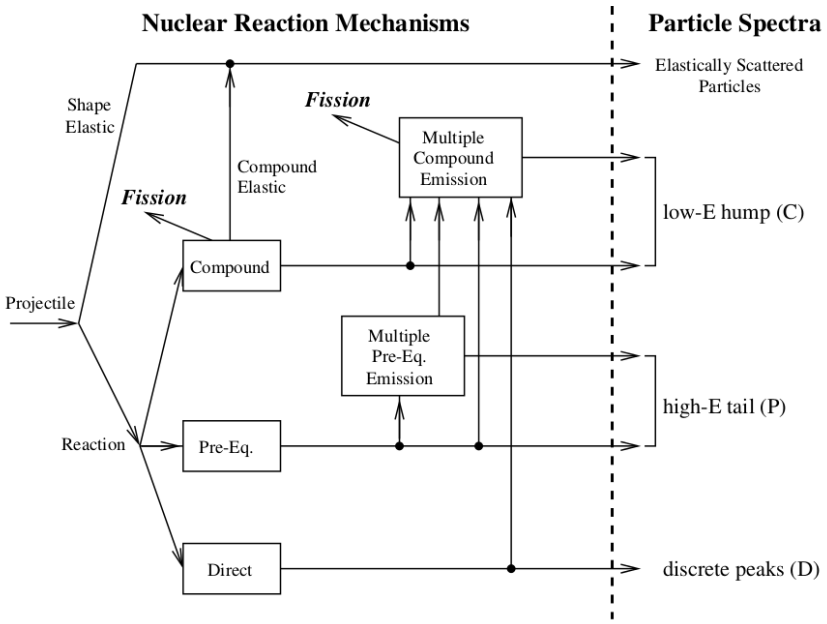

Figure 5.16: Schematic of the different nuclear reaction mechanism included in TALYS; taken from the TALYS-1.6 manual, Figure 3.1.

5.6.2 ^{237}Np(n,γ) cross section calculation

The level density and γ-ray strength function of ^{238}Np have been measured using the Oslo method [114]. Experimental data of the ^{237}Np neutron capture cross section exist up to 1 MeV, making it a good validation case of the TALYS calculation. The observed level density and γ-ray strength function are used as input to the TALYS calculation. Figure 5.18, taken from Ref. [114], shows the calculated ^{237}Np(n,γ) cross section. The agreement with available experimental data is excellent. The impact of the scissors resonance is shown and reaches a maximum of $\approx 25\%$ for neutron energies of ≈ 1 MeV.

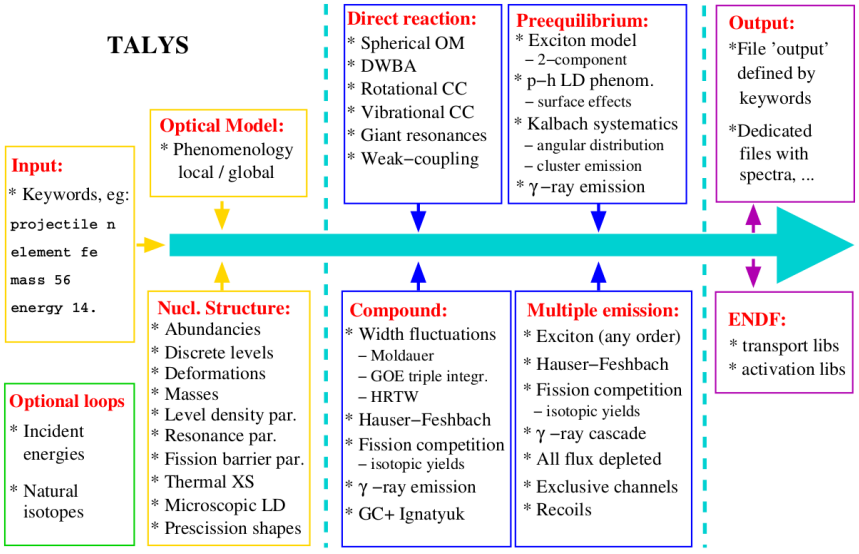

Figure 5.17: Nuclear models used in TALYS; taken from the TALYS-1.6 manual, Figure 4.1.

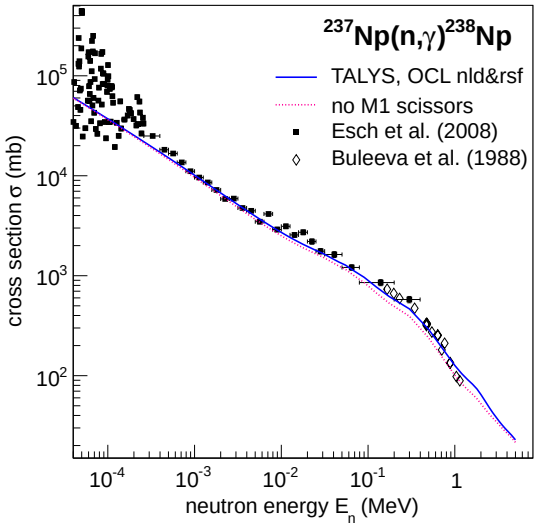

Figure 5.18: Calculation of the ^{237}Np neutron capture cross section using TALYS. Excellent agreement is found with experimental data; taken from Ref. [114], Figure 7.

5.6.3 Comparison of the ^{242}Pu(n,γ) cross section calculated with TALYS with databases

Unfortunately, there are no measurements of the ^{242}Pu(n,γ) for neutron energies above 200 keV. Our TALYS calculation will therefore be compared to cross sections available in the ENDF/B-VII.1 [11], JENDL-4-0 [44] and TENDL2014 [46], as well as a TALYS calculation with default parameters. The three main inputs of the neutron capture cross section calculation are the level density, the γ-ray strength function and the optical model potential. In this work, we only focus on the level density and γ-ray strength function that we measured. The default optical model potential for actinides is taken. The ENDF/B-VII.1 evaluation adopts some of the results from JENDL4.0 but no details are given about changes made to the level density or γ-ray strength function. JENDL-4.0 on the contrary lists all the parameters used in their calculations.

Level densities

Figure 5.19(a) shows the ^{243}Pu level density measured in this work along with the level density used by JENDL-4.0, TENDL2014 in their evaluations and the default TALYS input. All use the constant temperature model. Figure 5.19(b) shows the ratio of respectively the JENDL-4.0, TENDL2014 and the default TALYS level densities to the one measured in this work. TENDL2014 shows the largest discrepancy, being a factor 2-3 smaller than the measured level density. JENDL-4.0 and the default TALYS level density are more in agreement with our measurement, but discrepancies reach a factor of 2.

Strength functions

Figure 5.20 shows the comparison between the ^{243}Pu γ-ray strength function extracted in the present work (red curve) from measured data (black squares) and the one used in JENDL-4.0 (dashed black curve), and TENDL2014 (blue dashed-dotted curve). TENDL2014 uses the default input from TALYS. The strength function extracted from the present work is in very good agreement with the one used by JENDL-4.0 above 8 MeV, reproducing measured ^{239}Pu(γ,x) data from Berman *et al.* [121], Gurevitch *et al.* [79], and Moraes *et al.* [122]. The lowest energy measured by Moraes is 6.7 MeV. No measurements were available at lower energies before the present one. The main discrepancy is the addition of the resonance at 4.4 MeV and the low energy tail from the EGLO parametrization used by JENDL-4.0. The γ-ray strength function from the present work assumes also an EGLO parametrization for the giant electric dipole resonances at $E_\gamma = 11.1$ MeV and $E_\gamma = 14.2$ MeV, but with a constant temperature $T = 0.40$ MeV. The other resonances are modeled with a SLO parametrization. The TENDL2014 parametrization is completely off. There are no available suggested parameters for the ^{243}Pu γ-ray strength function in RIPL-3 [25]. TALYS uses empirical formulations of the γ-ray strength function. In the present work, as well as in the JENDL-4.0 calculation, it was assumed that the γ-ray strength function does not vary much from ^{239}Pu to ^{243}Pu.

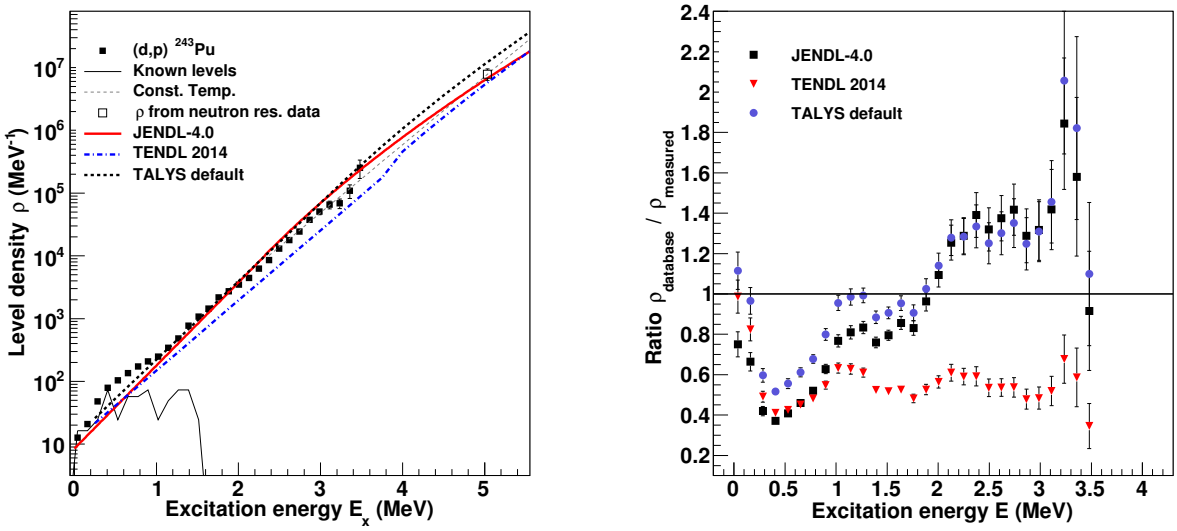

(a) (b)

Figure 5.19: (a) Measured ^{243}Pu level density (black filled squares) compare to the level density used in JENDL-4.0 [44] (red continuous curve), TENDL2014 [46] (blue dotted-dashed curve), and TALYS default (black dashed curve) calculations. The measured level density was normalized to the know levels (thin black line) and to the level density extracted from known neutron resonance spacings D_0 (empty square). (b) Ratio of the ^{243}Pu level density from respectively JENDL-4.0, TENDL2014 and the default one from TALYS to the level density measured in this work. Out of the three databases, TENDL2014 shows the largest discrepancy and is constantly about a factor of two lower than the level density measured in this work.

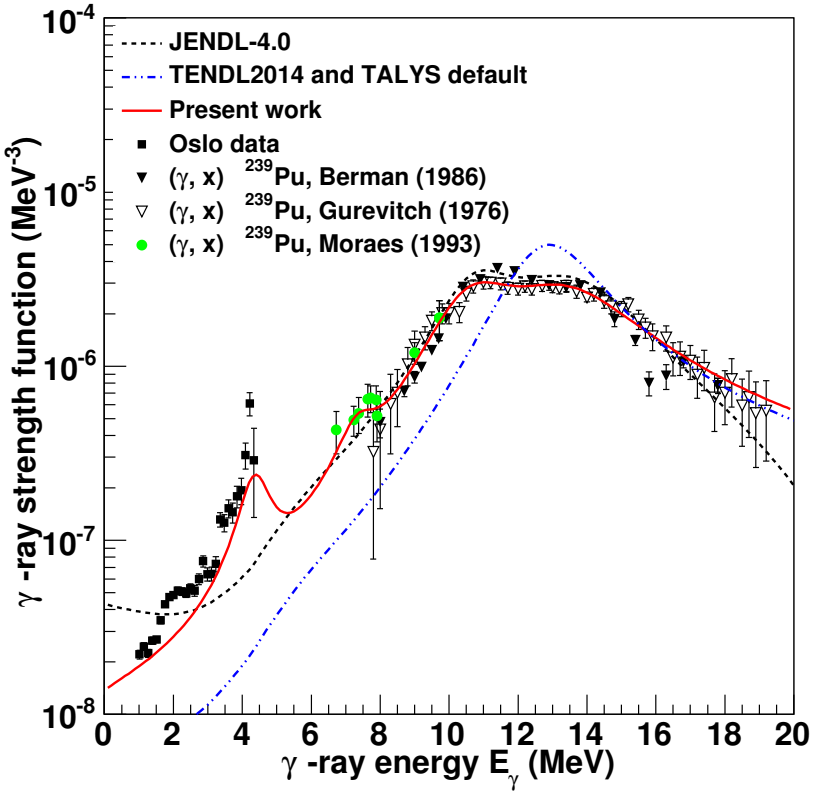

Figure 5.20: Comparison between the ^{243}Pu γ-ray strength function extracted in the present work (red curve) from measured data (black squares) and the one used in JENDL-4.0 (dashed black curve), and TENDL2014 (blue dashed-dotted curve). TENDL2014 uses the default input from TALYS. The (γ, x) data (black filled traingles, empty triangles and green dots) are taken, respectively, from Berman *et al.* [121], Gurevitch *et al.* [79], and Moraes *et al.* [122].

In TALYS and for the TENDL2014 evaluation, a normalization factor is introduced in order to reproduce observables. The average radiative capture width Γ_γ is due entirely to the s-wave interaction. Using the known Γ_γ value at the neutron separation energy, the normalization factor $G_{\rm norm}$ is obtained by equaling the s-wave radiation width to the integral of the γ-ray transmission coefficients over the density of final states that may be reached by primary γ-rays [26]:

$$\frac{2\pi\Gamma_\gamma}{D_0} = G_{\rm norm} \sum_{J,\Pi,Xl} \sum_{I'=|J-l|}^{J+l} \sum_{\Pi'} \int_0^{S_n} dE_\gamma T_{Xl}(E_\gamma) \rho(S_n - E_\gamma, I', \Pi') g(X, l, \Pi'), \qquad (5.17)$$

where D_0 is the average s-wave resonance spacing and ρ is the level density. J, Π correspond to the compound nuclear states spin and parity that can be formed with s-wave incident neutrons. I' and Π' correspond to the spin and parity of the final state after the primary γ-ray is emitted. X and l correspond to the different γ-radiation types and multipolarities. The function $g(X, l, \Pi')$ is equal to 1 is the multipole selection rule is satisfied and 0 if not.

For the TENDL2014 evaluation, $G_{\rm norm} = 5.26$. The default TALYS calculation uses $G_{\rm norm} = 3.22$.

The ^{242}Pu(n,γ) cross section

The ^{242}Pu(n,γ) cross section is calculated using TALYS and the experimentally measured level density and γ-ray strength function. The average neutron resonance spacing parameter D_0 and the average radiative capture width Γ_γ are reproduced. The entire procedure is detailed in Appendix C, only the main results are given in the present section.

The experimentally measured level density is parsed through TALYS in energy and spin dependent tables. Values are calculated using the constant temperature formula from Eq. (2.7). The spin distribution is given by the Eq. (B.3) with the spin cutoff parameter calculated using the parametrization from Egidy and Bucurescu [18, 17] given in Eq. (B.6). In order for the TALYS calculation to reproduce the experimentally measured $D_0 = 17$ eV parameter, the constant temperature of the level density is taken to be $T_{\rm CT} = 0.3833$ MeV.

The γ-ray strength function is implemented using the **fstrength.f** source file. The constant temperature of the EGLO tail of the GEDR is modified in order to match the experimental average radiative capture width $\langle\Gamma_\gamma\rangle = 22$ eV. Matching results are obtained for $T = 0.3860$ MeV. The cross section has been calculated with and without the scissors resonance.

Figure 5.21 shows the results of the TALYS calculated cross section with the scissors resonance (continuous red curve with blue error-band) and without (dashed red curve with red dots error band). The error bands are generated by taking into account the uncertainty in the two pygmy resonances described in Table 5.2 and the average radiative width $\langle\Gamma_\gamma\rangle = 22(1)$ meV. Including the scissors resonance in the calculation leads to an increase in the capture cross section (up to $\approx 10\%$ for incident neutron energy $E_n = 1.7$MeV). The

scissors resonance has a smaller effect for this calculation than for the ^{237}Np(n,γ) calculation (up to $\approx 25\%$ for a comparable scissors resonance strength) [114]. Our calculated cross section agrees with experimental data from Refs. [129, 130]. Unfortunately, there are no experimental data available above 200 keV. The calculation is also compared to the ENDF/B-VII.1 (black curve), JENDL-4.0 (dashed brown curve), TENDL2014 (dashed blue curve) evaluations, and the default TALYS calculation (magenta). The present calculation is in great agreement with the ENDF/B-VII.1 and JENDL-4.0 evaluations below 200 keV but not above. The TENDL2014 evaluation underestimates experimental data while the default TALYS calculation overestimates them. Large discrepancies are observed in the 1 MeV region as can be expected due to the discrepancies in level densities and γ-ray strength function. Experimental measurements of the ^{242}Pu(n,γ) cross section are needed to solve the discrepancies.

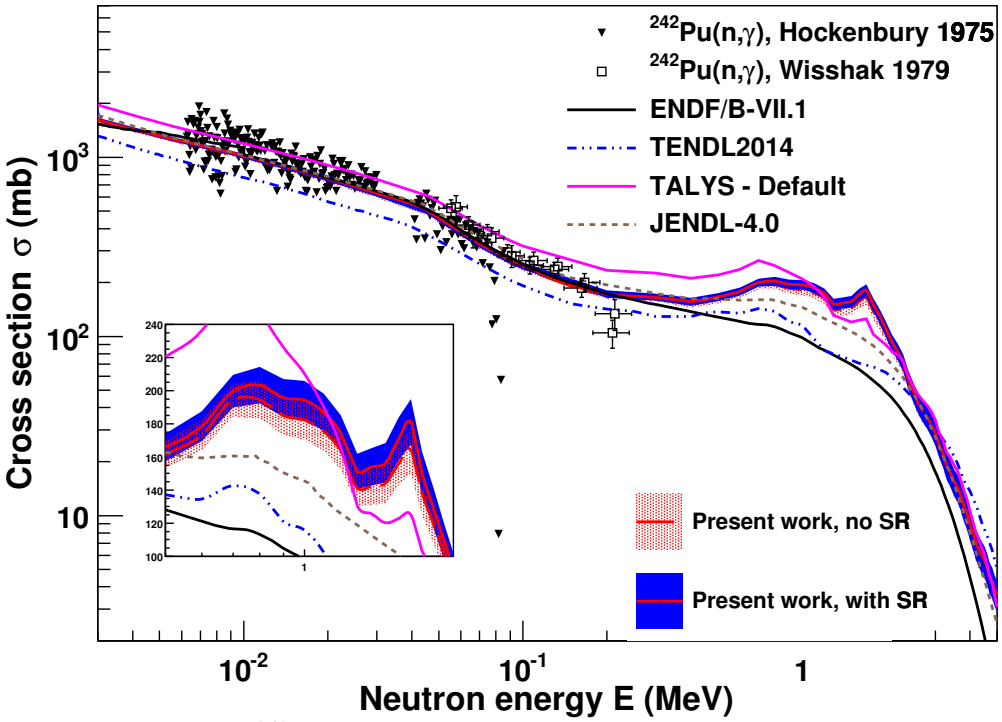

Figure 5.21: Calculated ^{242}Pu(n,γ) cross section using level density and γ-ray strength function parameters extracted from the experimental results. The calculation is done with the M1 scissors mode (continuous red curve with blue error-band) and without it (dashed red curve with red dots error-band). A zoom in the energy region 0.5 to 2 MeV, where the impact of the scissors resonance is the most important, is shown in the inset. The predictions are compared at low energy with measured data from Hockenbury *et al.* [129] (black triangles), Wisshak and Käppeler [130] (empty squares), and evaluations from ENDF/B-VII.1 (black curve), JENDL-4.0 (dashed grey curve), TENDL2014 (blue dotted-dashed curve) and the default TALYS calculation (magenta curve).

Chapter 6

Conclusion

6.1 Summary

Statistical properties of ^{243}Pu have been investigated using the Oslo method. Nuclear states in the quasi-continuum of ^{243}Pu were populated using the ^{242}Pu(d,p) reaction. From the primary γ-ray spectra, the level density and γ-ray strength function have been extracted for initial excitation energies ranging from 2.6 MeV to 4.3 MeV and for γ rays with energy $E_\gamma > 900$ keV.

The level density has been normalized to known levels at low excitation energy and to neutron resonance spacing data at the neutron separation energy. It follows closely a constant-temperature level density formula as seen in investigations on other actinides using the same method [6, 114]. The extracted nuclear temperature is $T = 0.40(1)$ MeV, in agreement with the other measured actinides, but lower than the temperature observed in rare-earth nuclei ($T \approx 0.5 - 0.6$ MeV) [35].

The γ-ray transmission coefficient has been normalized to the average total radiative width and extracted assuming that only half of the available nuclear levels at the neutron separation energy are populated by the (d,p) reaction. The γ-ray strength function is then calculated from the transmission coefficient assuming pure dipole radiation.

The γ-ray strength function exhibits two pygmy resonances, characteristic of neutron rich nuclei. Between 1.5 MeV and 3.5 MeV, the enhancement of the strength function is interpreted as the $M1$ scissors resonance. Similarly to the other actinides measured at Oslo, the measured centroid and strength of the scissors resonance are in very good agreement with the sum rule estimate from Ref. [60].

Using the measured level density and γ-ray strength function, the ^{242}Pu(n,γ) cross section is calculated with the TALYS code. Similarly to the calculation of the ^{237}Np(n,γ) cross section, the scissors resonance leads to an increase in the cross section. The increase reaches a maximum for incoming neutron energies around 1 MeV. For the ^{242}Pu(n,γ) cross section, the maximum increase is $\approx 10\%$, while it reaches $\approx 25\%$ for the ^{237}Np(n,γ) cross section. Large disagreement exists between the present calculation, the ENDF/B-VII.1 database, the JENDL-4.0 database, and the TENDL2014 database for the ^{242}Pu(n,γ)

cross section in the 1 MeV region, where no measured data is available. Very few measurements of the neutron capture cross section are available for actinides in this energy range, where the scissors resonance has the strongest influence. Reliable cross sections up to neutron energies of a few MeVs are crucial for the development of fast neutron spectrum nuclear reactors and nuclear waste management.

6.2 Outlook

Plutonium offers the possibility of measuring the pygmy and scissors resonances over a large mass region since $^{238-242,244}$Pu have long enough half lives (from 14 years for ^{241}Pu to 80 million years for ^{244}Pu) that targets of those isotopes can be fabricated. A measurement of the ^{240}Pu level density and γ-ray strength function has been realized and shows the same constant temperature dependence of the level density [131]. The scissors resonance is also observed in the γ-ray strength function of ^{240}Pu and the measured strength agrees within uncertainties.

A ^{244}Pu target has recently been made at Lawrence Livermore National Laboratory and will allow population of the ^{243}Pu compound nucleus using the $(^3\mathrm{He}, \alpha)$ reaction with a broader spin than with the (d, p) reaction on ^{242}Pu. The effect of the spin distribution on the extraction of the level density and γ-ray strength function remains an open question. The ^{245}Pu isotope can also be populated using the (d, p) reaction.

Appendix A

Qkinz calculations of the energy deposited in the particle detectors

Predictions of the energy deposited in the ΔE and E detectors are made using the Qkinz[1] software developed at University of Oslo. This software does the kinematic calculations, including the mean energy loss for the particle going through the target, the target backing and the Al layer on top of the ΔE detectors. The output is a calculated $\Delta E - E$ spectrum for the Siri detector and a table of the energy deposited in the particle telescope as a function of the excitation energy in the residual nucleus. Those results are used to calibrate the particle detectors and, later in the analysis, to translate the energy deposited in the detector to the excitation energy left in the residual nucleus.

The excitation energy, E_x, is approximated to a second order polynomial function of the total energy deposited in the particle telescope, $\Delta E + E$:

$$E_x = a_0 + a_1(\Delta E + E) + a_2(\Delta E + E)^2, \tag{A.1}$$

where a_0, a_1 and a_2 are free parameters. The a_2 parameter describing the non-linearity and remains small. The tables of corresponding E_x, ΔE and E are given below.

[1]The software can be downloaded at https://github.com/oslocyclotronlab/Qkinz

Table A.1: Ring 0, for $\theta \in [139°, 141°]$, where θ is the angle between the beam direction and the detector ring.

E_x [keV]	ΔE [keV]	E [KeV]	$\Delta E + E$ [keV]
0	851.01 ± 0.41	13426.93 ± 8.97	14277.94 ± 8.98
287.4	865.15 ± 0.43	13125.35 ± 9.04	13990.51 ± 9.05
333.2	867.46 ± 0.43	13077.24 ± 9.05	13944.69 ± 9.06
383.6	870.01 ± 0.44	13024.27 ± 9.06	13894.28 ± 9.07
402.6	870.98 ± 0.44	13004.30 ± 9.07	13875.27 ± 9.08
625.6	882.51 ± 0.46	12769.66 ± 9.13	13652.17 ± 9.14
653.8	884.00 ± 0.46	12739.95 ± 9.14	13623.95 ± 9.15
677.2	885.23 ± 0.46	12715.30 ± 9.14	13600.54 ± 9.15
703.9	886.65 ± 0.46	12687.17 ± 9.15	13573.82 ± 9.16
790.7	891.29 ± 0.47	12595.67 ± 9.17	13486.96 ± 9.18
809.5	892.30 ± 0.47	12575.85 ± 9.18	13468.15 ± 9.19
813.8	892.53 ± 0.47	12571.31 ± 9.18	13463.84 ± 9.19
845.4	894.24 ± 0.47	12537.98 ± 9.19	13432.22 ± 9.20
873.7	895.78 ± 0.47	12508.12 ± 9.20	13403.90 ± 9.21
905.7	897.52 ± 0.48	12474.35 ± 9.21	13371.87 ± 9.22
948.0	899.84 ± 0.48	12429.69 ± 9.22	13329.53 ± 9.23
981.0	901.66 ± 0.48	12394.84 ± 9.23	13296.50 ± 9.24
1130.1	909.98 ± 0.49	12237.27 ± 9.27	13147.25 ± 9.28
1176.5	912.61 ± 0.50	12188.19 ± 9.28	13100.80 ± 9.30
1213.0	914.69 ± 0.50	12149.57 ± 9.29	13064.25 ± 9.31
1301.6	919.78 ± 0.51	12055.76 ± 9.32	12975.54 ± 9.33
1367.8	923.63 ± 0.51	11985.63 ± 9.34	12909.26 ± 9.36
1387.4	924.78 ± 0.52	11964.85 ± 9.35	12889.63 ± 9.36
1420.5	926.72 ± 0.52	11929.76 ± 9.36	12856.48 ± 9.37
1434.7	927.56 ± 0.52	11914.70 ± 9.36	12842.26 ± 9.38
1516.6	932.42 ± 0.53	11827.82 ± 9.39	12760.24 ± 9.40
Fit	$a_0 = 13.986927$ MeV	$a_1 = -0.951438$	$a_2 = -2.019 \times 10^{-3}$ MeV^{-1}

Table A.2: Ring 1, for $\theta \in [137°, 139°]$.

E_x [keV]	ΔE [keV]	E [KeV]	$\Delta E + E$ [keV]
0	847.74 ± 0.42	13431.78 ± 9.08	14279.52 ± 9.09
287.4	861.83 ± 0.44	13130.19 ± 9.16	13992.02 ± 9.17
333.2	864.12 ± 0.44	13082.07 ± 9.17	13946.19 ± 9.18
383.6	866.67 ± 0.44	13029.10 ± 9.18	13895.77 ± 9.19
402.6	867.63 ± 0.44	13009.13 ± 9.19	13876.76 ± 9.20
625.6	879.12 ± 0.46	12774.48 ± 9.25	13653.60 ± 9.26
653.8	880.60 ± 0.46	12744.77 ± 9.26	13625.37 ± 9.27
677.2	881.83 ± 0.46	12720.12 ± 9.26	13601.95 ± 9.28
703.9	883.24 ± 0.47	12691.99 ± 9.27	13575.23 ± 9.28
790.7	887.86 ± 0.47	12600.49 ± 9.30	13488.35 ± 9.31
809.5	888.87 ± 0.47	12580.66 ± 9.30	13469.53 ± 9.31
813.8	889.10 ± 0.47	12576.13 ± 9.30	13465.23 ± 9.31
845.4	890.80 ± 0.48	12542.79 ± 9.31	13433.59 ± 9.32
873.7	892.33 ± 0.48	12512.93 ± 9.32	13405.26 ± 9.33
905.7	894.07 ± 0.48	12479.16 ± 9.33	13373.23 ± 9.34
948.0	896.38 ± 0.48	12434.50 ± 9.34	13330.88 ± 9.35
981.0	898.19 ± 0.49	12399.65 ± 9.35	13297.84 ± 9.36
1130.1	906.48 ± 0.50	12242.07 ± 9.40	13148.55 ± 9.41
1176.5	909.10 ± 0.50	12192.99 ± 9.41	13102.09 ± 9.42
1213.0	911.17 ± 0.51	12154.37 ± 9.42	13065.54 ± 9.43
1301.6	916.24 ± 0.51	12060.56 ± 9.45	12976.80 ± 9.46
1367.8	920.08 ± 0.52	11990.42 ± 9.47	12910.50 ± 9.48
1387.4	921.22 ± 0.52	11969.65 ± 9.47	12890.87 ± 9.49
1420.5	923.16 ± 0.52	11934.56 ± 9.48	12857.71 ± 9.50
1434.7	923.99 ± 0.53	11919.50 ± 9.49	12843.49 ± 9.50
1516.6	928.83 ± 0.53	11832.61 ± 9.52	12761.44 ± 9.53
Fit	$a_0 = 13.980141$ MeV	$a_1 = -0.950380$	$a_2 = -2.053 \times 10^{-3}$ MeV^{-1}

Table A.3: Ring 2, for $\theta \in [135°, 137°]$.

E_x [keV]	ΔE [keV]	E [KeV]	$\Delta E + E$ [keV]
0	845.56 ± 0.42	13435.35 ± 9.21	14280.91 ± 9.22
287.4	859.61 ± 0.44	13133.73 ± 9.29	13993.34 ± 9.30
333.2	861.90 ± 0.44	13085.60 ± 9.30	13947.50 ± 9.31
383.6	864.43 ± 0.45	13032.63 ± 9.32	13897.06 ± 9.33
402.6	865.40 ± 0.45	13012.65 ± 9.32	13878.05 ± 9.33
625.6	876.86 ± 0.47	12777.97 ± 9.39	13654.83 ± 9.40
653.8	878.33 ± 0.47	12748.26 ± 9.39	13626.60 ± 9.41
677.2	879.56 ± 0.47	12723.61 ± 9.40	13603.17 ± 9.41
703.9	880.97 ± 0.47	12695.47 ± 9.41	13576.44 ± 9.42
790.7	885.58 ± 0.48	12603.96 ± 9.43	13489.54 ± 9.45
809.5	886.58 ± 0.48	12584.13 ± 9.44	13470.71 ± 9.45
813.8	886.81 ± 0.48	12579.59 ± 9.44	13466.41 ± 9.45
845.4	888.51 ± 0.48	12546.26 ± 9.45	13434.76 ± 9.46
873.7	890.03 ± 0.48	12516.39 ± 9.46	13406.43 ± 9.47
905.7	891.77 ± 0.49	12482.62 ± 9.47	13374.38 ± 9.48
948.0	894.07 ± 0.49	12437.95 ± 9.48	13332.02 ± 9.49
981.0	895.88 ± 0.49	12403.10 ± 9.49	13298.98 ± 9.50
1130.1	904.15 ± 0.51	12245.50 ± 9.54	13149.64 ± 9.55
1176.5	906.76 ± 0.51	12196.41 ± 9.55	13103.17 ± 9.56
1213.0	908.82 ± 0.51	12157.78 ± 9.56	13066.60 ± 9.57
1301.6	913.88 ± 0.52	12063.96 ± 9.59	12977.85 ± 9.60
1367.8	917.71 ± 0.53	11993.81 ± 9.61	12911.52 ± 9.62
1387.4	918.85 ± 0.53	11973.04 ± 9.62	12891.88 ± 9.63
1420.5	920.78 ± 0.53	11937.94 ± 9.63	12858.72 ± 9.64
1434.7	921.61 ± 0.53	11922.88 ± 9.63	12844.49 ± 9.65
1516.6	926.44 ± 0.54	11835.98 ± 9.66	12762.42 ± 9.67
	$a_0 = 13.972100\,\text{MeV}$	$a_1 = -0.949176$	$a_2 = -2.092 \times 10^{-3}\,\text{MeV}^{-1}$

Table A.4: Ring 3, for $\theta \in [133°, 135°]$.

E_x [keV]	ΔE [keV]	E [KeV]	$\Delta E + E$ [keV]
0	844.45 ± 0.43	13437.64 ± 9.36	14282.09 ± 9.37
287.4	858.48 ± 0.45	13135.95 ± 9.44	13994.43 ± 9.45
333.2	860.77 ± 0.45	13087.82 ± 9.45	13948.58 ± 9.46
383.6	863.30 ± 0.45	13034.83 ± 9.47	13898.13 ± 9.48
402.6	864.26 ± 0.46	13014.85 ± 9.47	13879.11 ± 9.48
625.6	875.71 ± 0.47	12780.11 ± 9.54	13655.82 ± 9.55
653.8	877.18 ± 0.47	12750.40 ± 9.55	13627.58 ± 9.56
677.2	878.41 ± 0.48	12725.74 ± 9.55	13604.15 ± 9.56
703.9	879.81 ± 0.48	12697.60 ± 9.56	13577.41 ± 9.57
790.7	884.42 ± 0.48	12606.06 ± 9.59	13490.48 ± 9.60
809.5	885.42 ± 0.49	12586.23 ± 9.59	13471.65 ± 9.60
813.8	885.65 ± 0.49	12581.69 ± 9.59	13467.35 ± 9.61
845.4	887.35 ± 0.49	12548.35 ± 9.60	13435.69 ± 9.61
873.7	888.87 ± 0.49	12518.48 ± 9.61	13407.35 ± 9.62
905.7	890.60 ± 0.49	12484.69 ± 9.62	13375.29 ± 9.63
948.0	892.90 ± 0.50	12440.02 ± 9.63	13332.92 ± 9.65
981.0	894.71 ± 0.50	12405.16 ± 9.64	13299.86 ± 9.66
1130.1	902.97 ± 0.51	12247.52 ± 9.69	13150.49 ± 9.70
1176.5	905.58 ± 0.52	12198.42 ± 9.71	13103.99 ± 9.72
1213.0	907.64 ± 0.52	12159.78 ± 9.72	13067.42 ± 9.73
1301.6	912.69 ± 0.53	12065.94 ± 9.75	12978.63 ± 9.76
1367.8	916.51 ± 0.53	11995.78 ± 9.77	12912.29 ± 9.78
1387.4	917.65 ± 0.54	11974.99 ± 9.77	12892.65 ± 9.79
1420.5	919.58 ± 0.54	11939.89 ± 9.79	12859.47 ± 9.80
1434.7	920.41 ± 0.54	11924.82 ± 9.79	12845.24 ± 9.81
1516.6	925.24 ± 0.55	11837.90 ± 9.82	12763.14 ± 9.83
	$a_0 = 13.962684\,\text{MeV}$	$a_1 = -0.947812$	$a_2 = -2.136 \times 10^{-3}\,\text{MeV}^{-1}$

Table A.5: Ring 4, for $\theta \in [131°, 133°]$.

E_x [keV]	ΔE [keV]	E [KeV]	$\Delta E + E$ [keV]
0	844.40 ± 0.44	13438.60 ± 9.52	14283.01 ± 9.53
287.4	858.44 ± 0.45	13136.82 ± 9.61	13995.26 ± 9.62
333.2	860.73 ± 0.46	13088.67 ± 9.62	13949.40 ± 9.63
383.6	863.26 ± 0.46	13035.67 ± 9.63	13898.93 ± 9.64
402.6	864.22 ± 0.46	13015.68 ± 9.64	13879.90 ± 9.65
625.6	875.67 ± 0.48	12780.87 ± 9.71	13656.54 ± 9.72
653.8	877.15 ± 0.48	12751.15 ± 9.71	13628.30 ± 9.73
677.2	878.37 ± 0.48	12726.48 ± 9.72	13604.85 ± 9.73
703.9	879.78 ± 0.49	12698.33 ± 9.73	13578.11 ± 9.74
790.7	884.38 ± 0.49	12606.77 ± 9.76	13491.15 ± 9.77
809.5	885.39 ± 0.49	12586.93 ± 9.76	13472.31 ± 9.78
813.8	885.62 ± 0.50	12582.39 ± 9.76	13468.00 ± 9.78
845.4	887.31 ± 0.50	12549.03 ± 9.77	13436.34 ± 9.79
873.7	888.84 ± 0.50	12519.15 ± 9.78	13407.99 ± 9.80
905.7	890.57 ± 0.50	12485.35 ± 9.79	13375.92 ± 9.81
948.0	892.87 ± 0.51	12440.67 ± 9.81	13333.54 ± 9.82
981.0	894.67 ± 0.51	12405.79 ± 9.82	13300.47 ± 9.83
1130.1	902.94 ± 0.52	12248.10 ± 9.87	13151.04 ± 9.88
1176.5	905.55 ± 0.53	12198.98 ± 9.88	13104.53 ± 9.89
1213.0	907.61 ± 0.53	12160.33 ± 9.89	13067.94 ± 9.91
1301.6	912.67 ± 0.54	12066.46 ± 9.92	12979.13 ± 9.94
1367.8	916.49 ± 0.54	11996.27 ± 9.95	12912.76 ± 9.96
1387.4	917.63 ± 0.55	11975.48 ± 9.95	12893.11 ± 9.97
1420.5	919.56 ± 0.55	11940.36 ± 9.96	12859.92 ± 9.98
1434.7	920.39 ± 0.55	11925.30 ± 9.97	12845.68 ± 9.98
1516.6	925.21 ± 0.56	11838.35 ± 10.00	12763.56 ± 10.01
	$a_0 = 13.951749$ MeV	$a_1 = -0.946275$	$a_2 = -2.187 \times 10^{-3}$ MeV^{-1}

Table A.6: Ring 5, for $\theta \in [129°, 131°]$.

E_x [keV]	ΔE [keV]	E [KeV]	$\Delta E + E$ [keV]
0	845.43 ± 0.44	13438.19 ± 9.71	14283.62 ± 9.72
287.4	859.49 ± 0.46	13136.29 ± 9.79	13995.77 ± 9.80
333.2	861.78 ± 0.47	13088.12 ± 9.80	13949.90 ± 9.82
383.6	864.32 ± 0.47	13035.09 ± 9.82	13899.41 ± 9.83
402.6	865.28 ± 0.47	13015.09 ± 9.83	13880.37 ± 9.84
625.6	876.75 ± 0.49	12780.19 ± 9.89	13656.94 ± 9.91
653.8	878.22 ± 0.49	12750.46 ± 9.90	13628.68 ± 9.92
677.2	879.45 ± 0.49	12725.78 ± 9.91	13605.23 ± 9.92
703.9	880.86 ± 0.50	12697.61 ± 9.92	13578.47 ± 9.93
790.7	885.47 ± 0.50	12606.01 ± 9.95	13491.48 ± 9.96
809.5	886.48 ± 0.51	12586.16 ± 9.95	13472.64 ± 9.97
813.8	886.71 ± 0.51	12581.62 ± 9.96	13468.33 ± 9.97
845.4	888.41 ± 0.51	12548.25 ± 9.97	13436.66 ± 9.98
873.7	889.93 ± 0.51	12518.36 ± 9.97	13408.29 ± 9.99
905.7	891.67 ± 0.51	12484.55 ± 9.99	13376.21 ± 10.00
948.0	893.97 ± 0.52	12439.84 ± 10.00	13333.81 ± 10.01
981.0	895.78 ± 0.52	12404.95 ± 10.01	13300.73 ± 10.02
1130.1	904.06 ± 0.53	12247.19 ± 10.06	13151.25 ± 10.07
1176.5	906.67 ± 0.54	12198.05 ± 10.08	13104.72 ± 10.09
1213.0	908.74 ± 0.54	12159.38 ± 10.09	13068.12 ± 10.10
1301.6	913.80 ± 0.55	12065.47 ± 10.12	12979.27 ± 10.13
1367.8	917.63 ± 0.56	11995.25 ± 10.14	12912.88 ± 10.16
1387.4	918.77 ± 0.56	11974.45 ± 10.15	12893.22 ± 10.17
1420.5	920.70 ± 0.56	11939.31 ± 10.16	12860.02 ± 10.18
1434.7	921.54 ± 0.56	11924.24 ± 10.17	12845.78 ± 10.18
1516.6	926.37 ± 0.57	11837.25 ± 10.20	12763.62 ± 10.21
	$a_0 = 13.939883$ MeV	$a_1 = -0.944707$	$a_2 = -2.236 \times 10^{-3}$ MeV^{-1}

Table A.7: Ring 6, for $\theta \in [127°, 129°]$.

E_x [keV]	ΔE [keV]	E [KeV]	$\Delta E + E$ [keV]
0	847.53 ± 0.45	13436.33 ± 9.91	14283.87 ± 9.92
287.4	861.63 ± 0.48	13134.28 ± 10.00	13995.91 ± 10.01
333.2	863.93 ± 0.48	13086.08 ± 10.01	13950.02 ± 10.03
383.6	866.48 ± 0.48	13033.03 ± 10.03	13899.51 ± 10.04
402.6	867.44 ± 0.48	13013.02 ± 10.04	13880.47 ± 10.05
625.6	878.95 ± 0.50	12778.00 ± 10.11	13656.95 ± 10.12
653.8	880.43 ± 0.50	12748.25 ± 10.12	13628.68 ± 10.13
677.2	881.66 ± 0.51	12723.56 ± 10.12	13605.22 ± 10.14
703.9	883.07 ± 0.51	12695.38 ± 10.13	13578.45 ± 10.15
790.7	887.70 ± 0.52	12603.73 ± 10.16	13491.42 ± 10.18
809.5	888.71 ± 0.52	12583.87 ± 10.17	13472.57 ± 10.18
813.8	888.94 ± 0.52	12579.33 ± 10.17	13468.26 ± 10.18
845.4	890.64 ± 0.52	12545.94 ± 10.18	13436.58 ± 10.19
873.7	892.17 ± 0.52	12516.03 ± 10.19	13408.20 ± 10.20
905.7	893.91 ± 0.53	12482.20 ± 10.20	13376.11 ± 10.21
948.0	896.23 ± 0.53	12437.47 ± 10.22	13333.69 ± 10.23
981.0	898.04 ± 0.53	12402.56 ± 10.23	13300.60 ± 10.24
1130.1	906.34 ± 0.55	12244.71 ± 10.28	13151.05 ± 10.29
1176.5	908.96 ± 0.55	12195.55 ± 10.30	13104.51 ± 10.31
1213.0	911.04 ± 0.55	12156.86 ± 10.31	13067.89 ± 10.32
1301.6	916.12 ± 0.56	12062.89 ± 10.34	12979.00 ± 10.36
1367.8	919.96 ± 0.57	11992.63 ± 10.37	12912.58 ± 10.38
1387.4	921.10 ± 0.57	11971.82 ± 10.37	12892.92 ± 10.39
1420.5	923.04 ± 0.57	11936.66 ± 10.38	12859.70 ± 10.40
1434.7	923.87 ± 0.58	11921.58 ± 10.39	12845.45 ± 10.41
1516.6	928.73 ± 0.58	11834.54 ± 10.42	12763.26 ± 10.44
	$a_0 = 13.926142$ MeV	$a_1 = -0.942932$	$a_2 = -2.293 \times 10^{-3}$ MeV^{-1}

Table A.8: Ring 7, for $\theta \in [125°, 127°]$.

E_x [keV]	ΔE [keV]	E [KeV]	$\Delta E + E$ [keV]
0	850.73 ± 0.47	13432.94 ± 10.14	14283.68 ± 10.15
287.4	864.90 ± 0.49	13130.71 ± 10.23	13995.60 ± 10.25
333.2	867.20 ± 0.49	13082.48 ± 10.25	13949.69 ± 10.26
383.6	869.76 ± 0.50	13029.40 ± 10.27	13899.16 ± 10.28
402.6	870.73 ± 0.50	13009.38 ± 10.27	13880.11 ± 10.28
625.6	882.29 ± 0.52	12774.21 ± 10.35	13656.49 ± 10.36
653.8	883.77 ± 0.52	12744.44 ± 10.36	13628.21 ± 10.37
677.2	885.01 ± 0.52	12719.73 ± 10.36	13604.74 ± 10.38
703.9	886.43 ± 0.52	12691.53 ± 10.37	13577.96 ± 10.39
790.7	891.08 ± 0.53	12599.82 ± 10.40	13490.90 ± 10.42
809.5	892.09 ± 0.53	12579.95 ± 10.41	13472.04 ± 10.42
813.8	892.32 ± 0.53	12575.41 ± 10.41	13467.73 ± 10.43
845.4	894.03 ± 0.54	12542.00 ± 10.42	13436.03 ± 10.44
873.7	895.57 ± 0.54	12512.07 ± 10.43	13407.64 ± 10.45
905.7	897.32 ± 0.54	12478.22 ± 10.44	13375.54 ± 10.46
948.0	899.64 ± 0.54	12433.46 ± 10.46	13333.10 ± 10.47
981.0	901.46 ± 0.55	12398.52 ± 10.47	13299.99 ± 10.49
1130.1	909.80 ± 0.56	12240.57 ± 10.53	13150.38 ± 10.54
1176.5	912.44 ± 0.57	12191.37 ± 10.54	13103.81 ± 10.56
1213.0	914.52 ± 0.57	12152.66 ± 10.56	13067.18 ± 10.57
1301.6	919.62 ± 0.58	12058.63 ± 10.59	12978.25 ± 10.61
1367.8	923.48 ± 0.59	11988.32 ± 10.62	12911.80 ± 10.63
1387.4	924.63 ± 0.59	11967.49 ± 10.62	12892.12 ± 10.64
1420.5	926.58 ± 0.59	11932.31 ± 10.64	12858.89 ± 10.65
1434.7	927.42 ± 0.59	11917.22 ± 10.64	12844.64 ± 10.66
1516.6	932.29 ± 0.60	11830.11 ± 10.67	12762.41 ± 10.69
	$a_0 = 13.910267$ MeV	$a_1 = -0.940922$	$a_2 = -2.358 \times 10^{-3}$ MeV^{-1}

Appendix B

EMPIRE estimation of the relative amount of levels populated by nuclear reaction

EMPIRE[126] is a "modular system of nuclear reaction codes for advanced modeling of nuclear reactions using various theoretical models. It consists of a number of FORTRAN codes, input parameter libraries, and experimental data library (EXFOR/CSISRS)"[1].

Simultaneous extraction of the level density and γ-ray strength function is performed by analyzing coincident particle-γ data from charged particle reaction using the Oslo method [5, 132]. Recent measurements in the actinides revealed normalization issues when the (d, p) reaction is used [8, 114, 123]. The γ-ray strength function extracted below the neutron separation energy, supposing that all spins are populated in the residual nucleus, is not realistic and cannot match previously measured values above the neutron separation energy. More realistic results are obtained assuming that not all spins are populated and extracting the γ-ray strength function using a reduced level density.

In order to estimate the relative level population, the EMPIRE code is used to estimate the spin distribution left in the residual nucleus after charged particle reactions. The EMPIRE code has been modified by incorporating the spin dependent level density from Ref. [17] and Ref. [19]. Population of residual nuclei are compared to their intrinsic spin distribution to extract the ratio of level populated for some La isotopes and actinides. No effort was put into reproducing experimental cross section data.

B.1 Spin dependent level density

A phenomenological model is used to describe the level density ρ as a function of the excitation energy, E_x, the nuclear spin, J, and parity, π, assuming that the following

[1] http://www.nndc.bnl.gov/empire/main.html

separable form holds:

$$\rho(E_x, J, \pi) = \frac{1}{2}\rho(E_x)f(J). \tag{B.1}$$

The parity dependence is neglected. Our main focus is the population at the neutron separation energy where the parity dependence should be small. The distribution of different magnetic states is given by Ref. [14]:

$$\rho(E_x, M) = \rho(E_x)\frac{\exp\left(-M^2/2\sigma^2\right)}{\sigma\sqrt{2\pi}}, \tag{B.2}$$

where σ is the spin cutoff parameter.

In the absence of an external field, only levels of different spin J can be observed. The magnetic states of quantum number, M, are degenerate. As suggested by Refs. [14, 20], states like $|J+1, M=J+1\rangle$ and $|J+1, M=J\rangle$ are degenerate. To avoid double counting, we notice that the expression $\rho(M=J) - \rho(M=J+1)$ give the number of states $|J, M=J\rangle$, which corresponds to $f(J)$. Using a Taylor expansion, the following expression is used for $f(J)$:

$$f(J) = \exp\left(-{}^{J^2}\!/_{2\sigma^2}\right) - \exp\left(-{}^{(J+1)^2}\!/_{2\sigma^2}\right) \approx \frac{2J+1}{2\sigma^2}\exp\left(-{}^{\left(J+\frac{1}{2}\right)^2}\!/_{2\sigma^2}\right). \tag{B.3}$$

The Back-Shifted Fermi Gas (BSFG) model [20] gives the energy dependence of the level density:

$$\rho(E_x) = \frac{\exp\left(2\sqrt{a\left[E_x - E_1\right]}\right)}{12\sqrt{2}\sigma a^{1/4}\left(E_x - E_1\right)^{5/4}}, \tag{B.4}$$

where a is the level density parameter and E_1 the energy back-shift. Egidy and Bucurescu published systematics of the level density parameters for nuclei between ^{18}F and ^{251}Cf[17, 18, 19].

B.2 Additions to the EMPIRE code

Two new spin dependent level density distributions have been added to the Empire[2] code [126]. Following the parametrization from Refs. [17, 18], the energy dependent level density parameter is given by:

$$a(E_x) = \widetilde{a}\left[1 + \frac{S(Z,N) - \Delta}{E_x - E_1}\left(1 - \exp\left\{-\gamma(E_x - E_1)\right\}\right)\right], \tag{B.5}$$

where $\widetilde{a}$ is the asymptotic level density parameter, $S(Z,N)$ is a shell correction term, Δ is a pairing term and γ is set to $0.06\,\mathrm{MeV}^{-1}$. The spin cutoff parameter is given by the

[2]Modifications have been made from the version 3.2 (Malta).

following parametrization:

$$\sigma^2 = 0.0146A^{5/3}\frac{1+\sqrt{1+4a(E_x-E_1)}}{2a}, \tag{B.6}$$

where A is the mass number.

The second parametrization used is taken from Ref. [19]. The level density parameter is not energy dependent and the spin cutoff parameter is given by:

$$\sigma^2 = 0.391A^{0.675}(E_x - E_1 - 0.381)^{0.312}. \tag{B.7}$$

The two parametrizations can be called chosen the keyword LEVDEN (5 and 6 respectively). The second parametrization gives consistently a lower spin cutoff parameter. It is more suitable for light nuclei, while the first parametrization should be used for heavier nuclei, especially actinides.

The following changes have been made to the EMPIRE code:

- The data files mass.mas03, rct2.mas03 and rct7.mas03 available in the Oslo software package have to be added to $EMPIRE/data/egidy03
- main.f: The subroutine ReadEgidy is called. It will load the data files mass.mas03, rct2.mas03 and rct7.mas03 into matrices that will be used to calculate the different level density parameters.
- input.f: Modifications allowing to call for the two parametrizations above using the LEVDEN keyword.
- Egidy.f: contains the subroutines ReadEgidy, reading the data tables, RO_EGIDY calculating the spin dependent level density for the parametrization from Refs. [17, 18] and RO_EGIDY2009 calculating the spin dependent level density using the parametrization from Ref. [19]. Both RO_EGIDY and RO_EGIDY2009 fill the level density matrix RO$(E_x, J, \pi, Nnuc)$ used later by EMPIRE to calculate the population in the residual nucleus. $Nnuc$ represents the nucleus id number.

B.3 Spin population following charged particle reaction

Measurement of the statistical properties of the nuclei, such as the nuclear level density and γ-ray strength function are key inputs for calculations of nuclear cross sections within the framework of the statistical model. The Oslo method [5, 132] allows extraction of the functional form of the level density and γ-ray strength function. The level density is normalized by matching the data points to known discrete levels at low energy and

estimated level density at the neutron separation energy from neutron-resonance spacing data using the formula[5]:

$$\rho(S_n) = \frac{2\sigma^2}{D_0} \cdot \frac{1}{(I_t+1)\exp\left[-(I_t+1)^2/2\sigma^2\right] + I_t \exp\left[-I_t^2/2\sigma^2\right]}, \tag{B.8}$$

where σ is the spin-cutoff parameter, D_0 is the neutron resonance spacing, and I_t is the spin of the target nucleus. The following intrinsic spin distribution is assumed [113]:

$$g(E_x, J) = \frac{2J+1}{2\sigma^2(E_x)} \exp\left[-(J+1/2)^2/2\sigma^2(E_x)\right], \tag{B.9}$$

where J is the spin of the nucleus considered. Recent measurements in the actinides revealed normalization issues when the (d,p) reaction is used [8, 114, 123]. The γ-ray strength function extracted below the neutron separation energy, assuming that all spins are populated in the residual nucleus, is not realistic and cannot match previously measured values above the neutron separation energy. More realistic results are obtained assuming that not all spins are populated and extracting the γ-ray strength function using a reduced level density. The EMPIRE code [126] is used to estimate the spin distribution populated in the residual nucleus after charged particle reaction. EMPIRE outputs the cross section to populate each spin as a function of the excitation energy of the residual nucleus following a charged particle induced reaction. This distribution is normalized to the intrinsic spin distribution from Eq. (B.9). The reduction factor, i.e. the fraction of the intrinsic spin populated is calculated assuming that there is at least one spin for which all levels are populated by the reaction. In the following, the reduction factor, f_{red}, is estimated for the two parametrizations presented above.

No effort has been made in reproducing reaction cross sections. The only changes from a default run is the changes in the level density calculation including the spin distribution.

B.3.1 Reactions on ^{139}La

The following reactions: (d,p), (^{3}He,^{3}He), and (^{3}He,α), on a ^{139}La target, were measured at the Oslo Cyclotron Laboratory [133]. The beam energy was 13.5 MeV for deuterium and 38 MeV for the ^{3}He beam.

Figures B.1, B.2, and B.3 show the intrinsic spin distribution at the neutron separation energy (black squares) and the populated spin distribution calculated with EMPIRE (red crosses). The calculated population is normalized to the intrinsic population by supposing that there is one spin for which all levels are populated. Calculations are run for the two different parametrizations proposed by Egidy and Bucurescu. The parametrization from Ref. [17] has a spin cutoff parameter that is systematically higher than the parametrization from Ref. [19], and should be more appropriate for heavier nuclei for actinide and lanthanide. The parametrization from Ref. [19] is used here as a lower limit for the spin cutoff parameter. While the reduction factor is very similar for the (d,p) reaction, ^{3}He

induced reactions populates higher spins and the intrinsic spin distribution from Ref. [19] is too narrow. The normalization point is then situated on the high spin tail of the spin distribution which increases the sensitivity of the reduction factor.

Table B.1 gives the reduction factors for the different reactions. No estimation is given for ^{3}He induced reactions using the parametrization from Ref [19] because no proper normalization is possible.

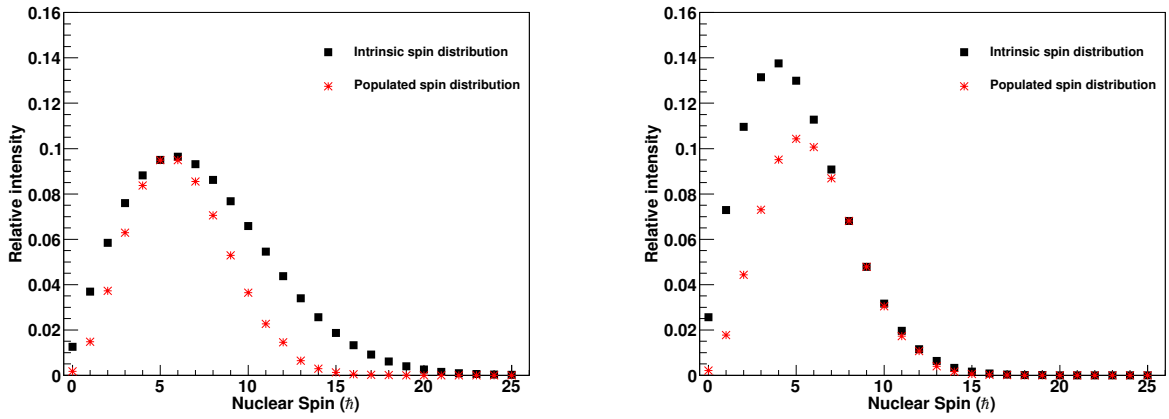

(a) Ref. [17] parametrization.

(b) Ref. [19] parametrization.

Figure B.1: ^{140}La intrinsic spin distribution at the neutron separation energy (black squares) for the two different parametrizations presented above. The populated spin distribution following a (d, p) reaction at $E_x = S_n$ is calculated with the EMPIRE code [126] and normalized to the intrinsic spin distribution.

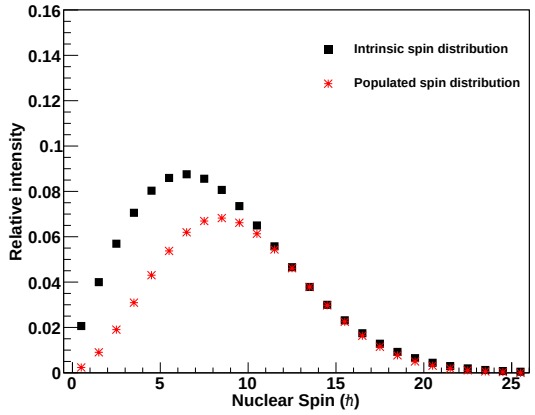

(a) Ref. [17] parametrization.

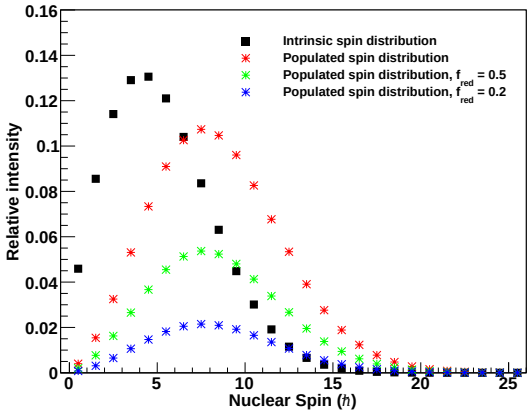

(b) Ref. [19] parametrization.

Figure B.2: ^{139}La intrinsic spin distribution at the neutron separation energy (black squares) for the two different parametrizations presented above. The populated spin distribution following a (^{3}He,^{3}He) reaction at $E_x = S_n$ is calculated with the EMPIRE code [126] and normalized to the intrinsic spin distribution. Using the parametrization from Ref. [19], the spin cutoff parameter for the intrinsic spin distribution is too small. The EMPIRE output suggests that the intrinsic spin distribution is not broad enough, or that only very few levels are populated.

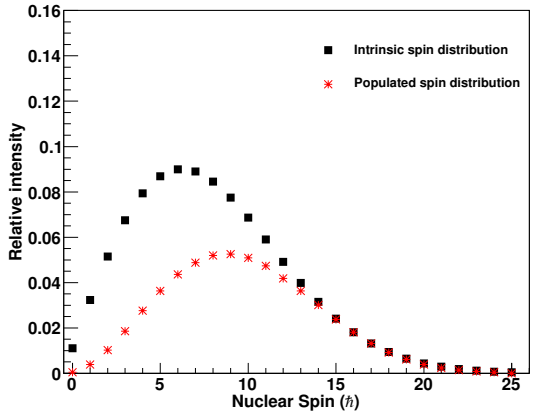

(a) Ref. [17] parametrization.

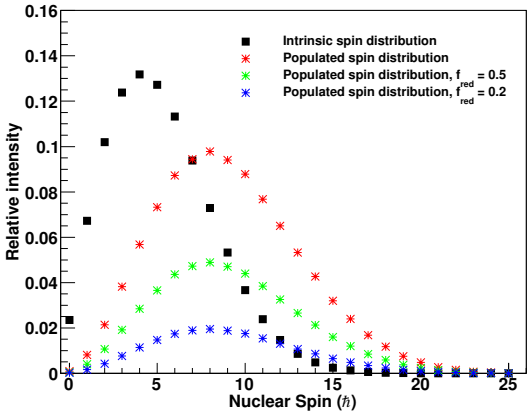

(b) Ref. [19] parametrization.

Figure B.3: ^{138}La intrinsic spin distribution at the neutron separation energy (black squares) for the two different parametrizations presented above. The populated spin distribution following a (^{3}He,α) reaction at $E_x = S_n$ is calculated with the EMPIRE code [126] and normalized to the intrinsic spin distribution. Using the parametrization from Ref. [19], the spin cutoff parameter for the intrinsic spin distribution is too small. The EMPIRE output suggests that the intrinsic spin distribution is not broad enough, or that only very few levels are populated.

Table B.1: Reduction factors calculated using EMPIRE for the different reaction on the ^{139}La target.

Residual nucleus	Reaction	S_n	$f_{red}{}^a$	$f_{red}{}^b$
^{140}La	(d,p)	5.16	0.68	0.71
^{139}La	(^{3}He,^{3}He)	8.78	0.73	/
^{138}La	(^{3}He,α)	7.45	0.58	/

[a] from Ref [17]
[b] from Ref [19]

B.3.2 Reactions on actinides

Several actinides have recently been studied [6, 8, 123, 114]. Figures B.4 and B.5 show the intrinsic spin distribution and the population following a (d,p) reaction on several actinides. The relative number of populated states using the spin cutoff parameter from Ref. [19] is systematically higher than using Ref. [17]. The reduction factors used to extract the γ-ray strength function of ^{233}Th, ^{239}U and ^{238}Np in Ref. [8, 114] are between the minimum value set by Ref. [17] and Ref. [19], which could be used as higher and lower limits for the calculated reduction factors.

FigureB.6 compares population following (d,d') and (^{3}He,^{3}He$'$) reactions. The (^{3}He,^{3}He$'$) reaction populates a broader range of spin and therefore has a higher ratio of populated states. The published estimated reduction factor are in better agreement with Ref. [19] but systematically higher than the calculated population. Calculated populations on U isotopes following (d,d') and (d,t) reactions, shown in FigureB.7, are also lower than published results from Ref. [8]. In Ref. B.8, ^{3}He induced reactions were assumed to populate all available levels. Calculated values suggests that at least 57 of the levels are populated.

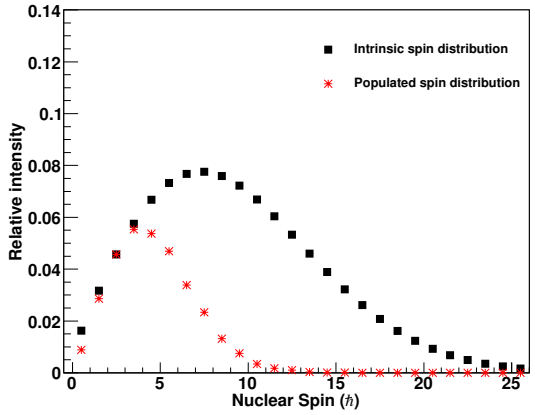

(a) $^{233}\mathrm{Th}^{(a)}$.

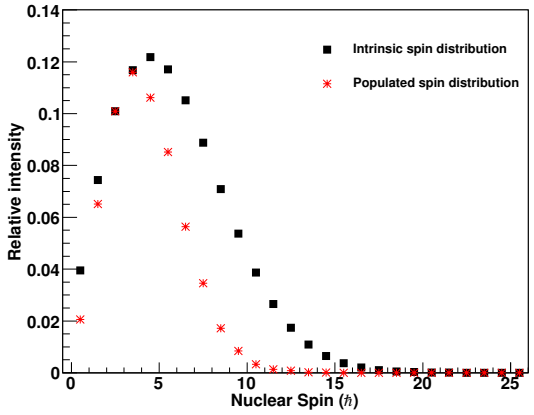

(b) $^{233}\mathrm{Th}^{(b)}$.

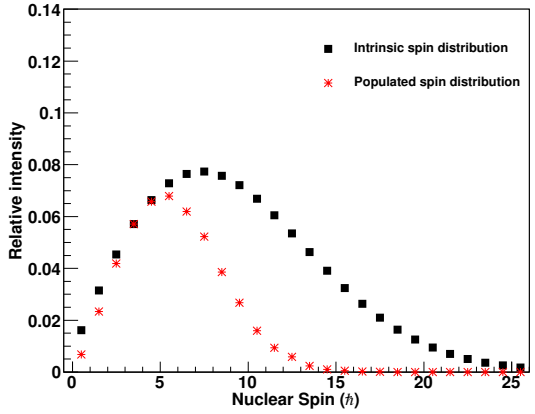

(c) $^{239}\mathrm{U}^{(a)}$.

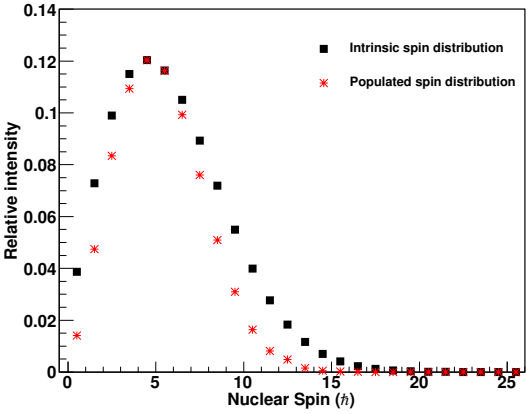

(d) $^{239}\mathrm{U}^{(b)}$.

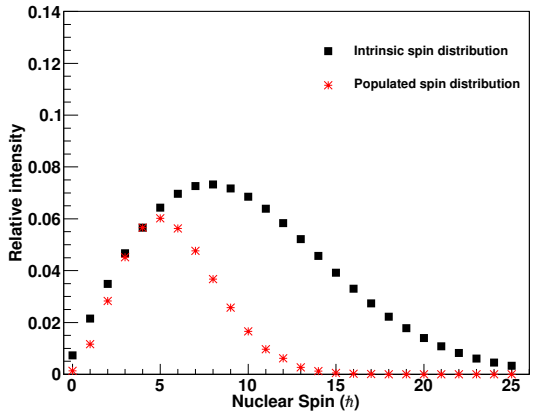

(e) $^{237}\mathrm{Np}^{(a)}$.

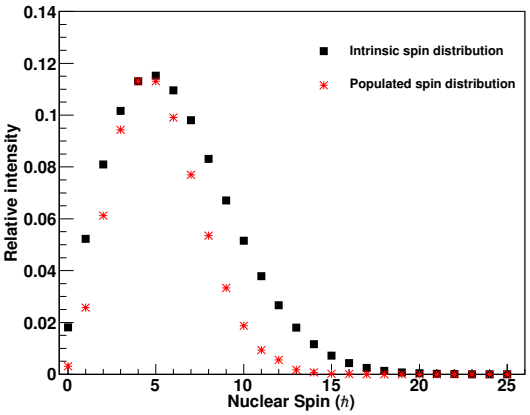

(f) $^{237}\mathrm{Np}^{(b)}$.

Figure B.4: Comparison of the intrinsic spin distribution at the neutron separation energy (black squares) to the calculated population following (d, p) reactions (red stars), for two spin-cutoff parameters from Ref. [17] (a) and Ref. [19] (b).

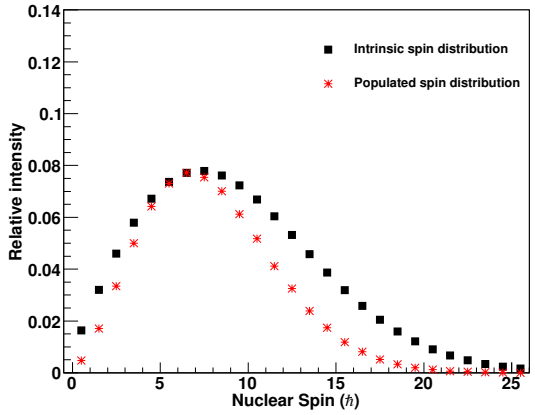

(a) $(^3\mathrm{He},\alpha)^{231}\mathrm{Th}^{(a)}$.

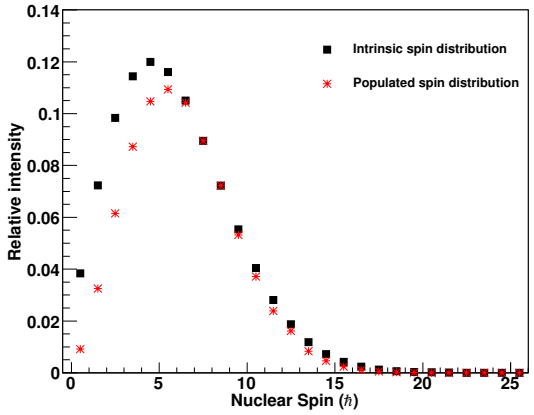

(b) $(^3\mathrm{He},\alpha)^{231}\mathrm{Th}^{(b)}$.

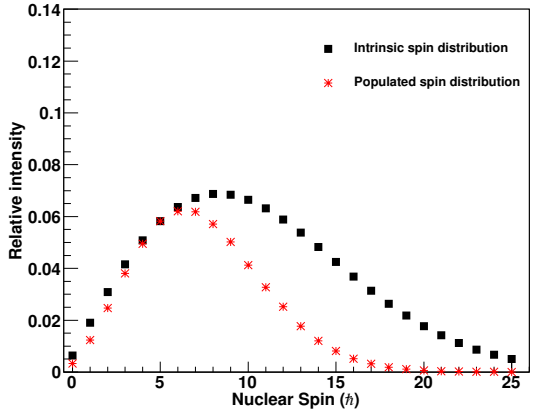

(c) $(^3\mathrm{He},d)^{233}\mathrm{Pa}^{(a)}$.

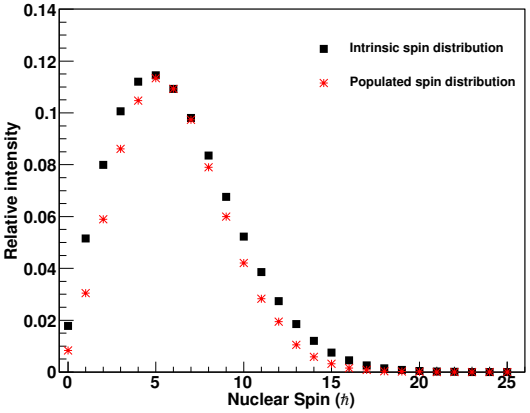

(d) $(^3\mathrm{He},d)^{233}\mathrm{Pa}^{(b)}$.

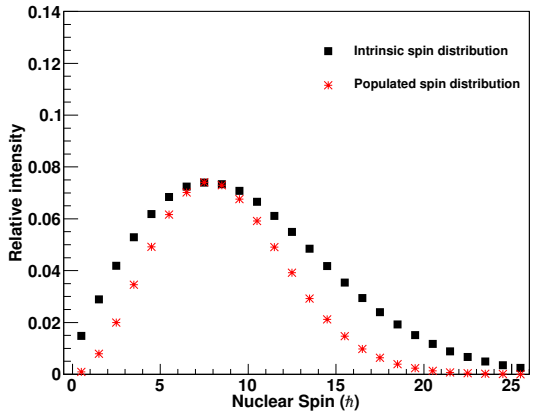

(e) $(^3\mathrm{He},t)^{232}\mathrm{Pa}^{(a)}$.

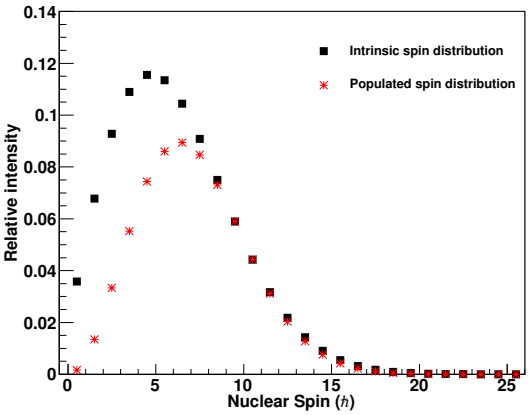

(f) $(^3\mathrm{He},t)^{232}\mathrm{Pa}^{(b)}$.

Figure B.8: Comparison of the intrinsic spin distribution at the neutron separation energy (black squares) to the calculated population following ^{3}He induced reactions on ^{232}Th, for two spin-cutoff parameters from Ref. [17] (a) and Ref. [19] (b).

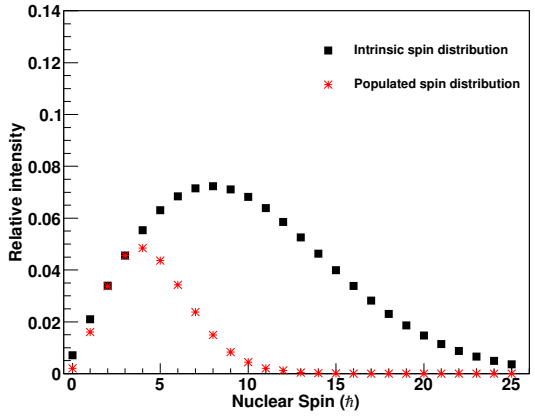

(a) $^{240}\mathrm{Pu}^{(a)}$.

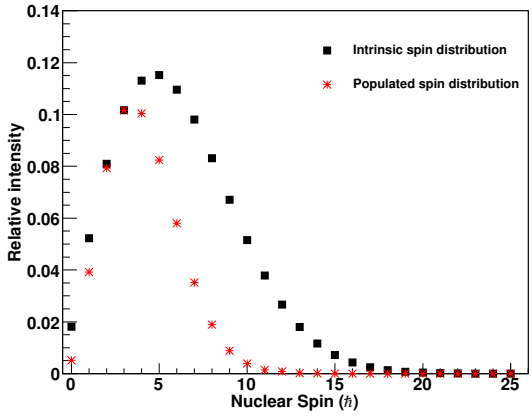

(b) $^{240}\mathrm{Pu}^{(b)}$.

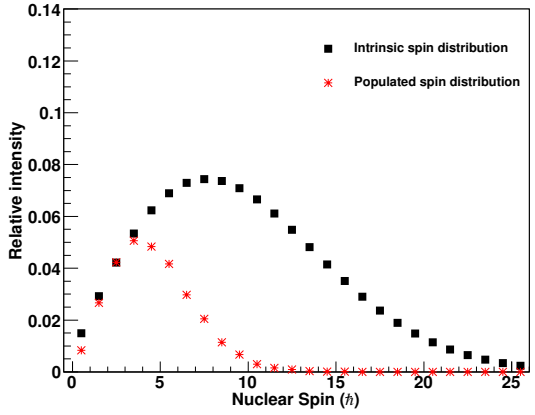

(c) $^{243}\mathrm{Pu}^{(a)}$.

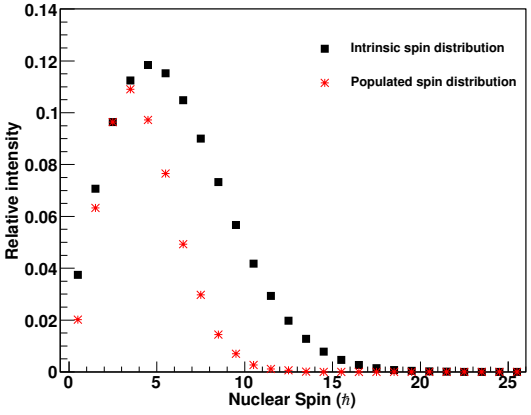

(d) $^{243}\mathrm{Pu}^{(b)}$.

Figure B.5: Comparison of the intrinsic spin distribution at the neutron separation energy (black squares) to the calculated population following (d, p) reactions (red stars), for two spin-cutoff parameters from Ref. [17] (a) and Ref. [19] (b), for ^{240}Pu and ^{243}Pu.

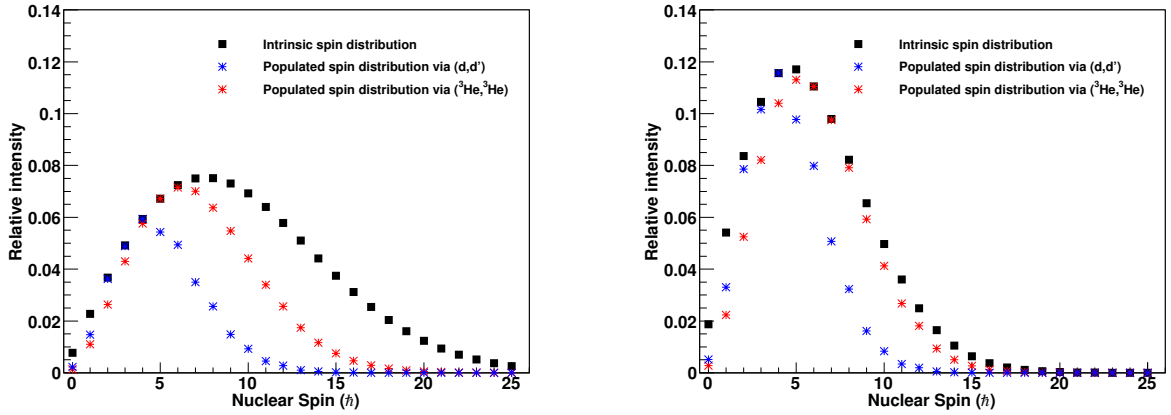

(a) $^{232}\mathrm{Th}^{(a)}$. (b) $^{232}\mathrm{Th}^{(b)}$.

Figure B.6: Comparison of the intrinsic spin distribution at the neutron separation energy (black squares) to the calculated population following (d, d') (red stars) and (^{3}He,^{3}He') (blue stars) reactions on ^{232}Th, for two spin-cutoff parameters from Ref. [17] (a) and Ref. [19] (b).

Variation of the population ratio as a function of the spin cutoff parameters

The difference of spin cutoff parameters between Ref. [17] and Ref. [19] is important. Calculations have been made by reducing the spin cutoff parameter, σ_R^2, from Equation (B.6), introducing a reduction factor R:

$$\sigma_R^2 = R^2 \times 0.0146 A^{5/3} \frac{1 + \sqrt{1 + 4a(E_x - E_1)}}{2a} = R^2 \sigma_{EB06}^2, \tag{B.10}$$

where σ_{EB06}^2 is the spin cutoff parameter calculated with the parametrization from Ref.[17]. Figure B.9 shows the ratio of spin populated as a function of R at $E_x = S_n$. For $(d, p)^{243}$Pu and (^{3}He,d)^{233}Pa, the relative spin population is monotonically increasing while reducing the spin cutoff parameter, but this isn't the case for (^{3}He,t)^{232}Pa. For this reason, the relative populations obtained from Ref.[17] and Ref.[19] parametrizations cannot be taken as extrema without caution.

Beam energy dependence

With increasing beam energy, more units of spin can be transferred. The (d, p) reaction on actinides fails to populate the high spin tail of the intrinsic spin distribution. Figure B.10 shows the increase in the relative spin population for $(d, p)^{243}$Pu as a function of the beam energy, using the spin cutoff parameter from Ref [17].

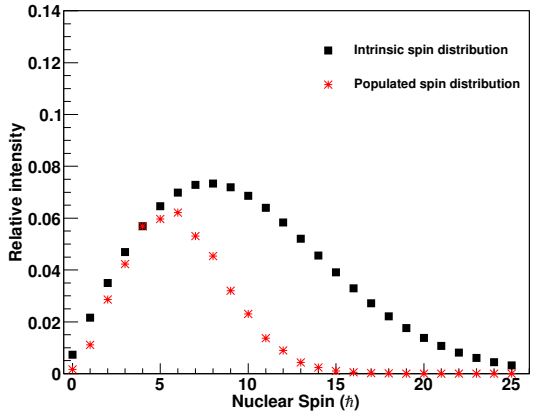

(a) $^{238}\mathrm{U}^{(a)}$.

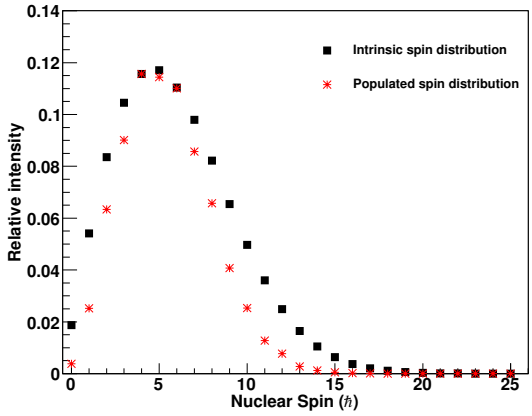

(b) $^{238}\mathrm{U}^{(b)}$.

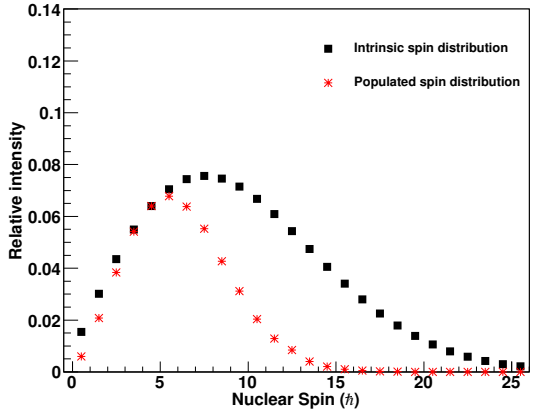

(c) $^{237}\mathrm{U}^{(a)}$.

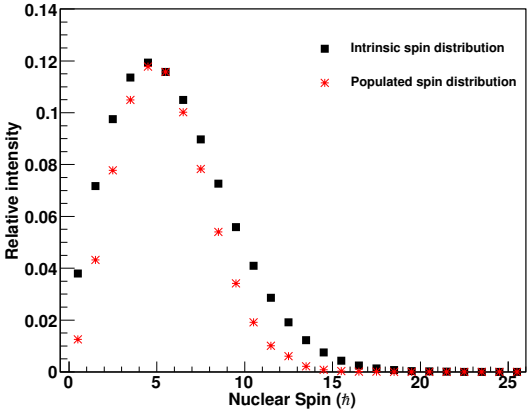

(d) $^{237}\mathrm{U}^{(b)}$.

Figure B.7: Comparison of the intrinsic spin distribution at the neutron separation energy (black squares) to the calculated population following (d, d') and (d, t) reactions on ^{238}U, for two spin-cutoff parameters from Ref. [17] (a) and Ref. [19] (b).

Table B.2: Parameters used for the calculation of the fraction of levels populated following nuclear reactions leaving the residual nucleus at $E_x = S_n$ for two spin cutoff parametrizations (^{a} for Ref [17] and ^{b} for Ref [19]).

Reaction	Projectile Energy [MeV]	Target	Product	S_n [MeV]	$\sigma(S_n)^a$	Population (%)^a	$\sigma(S_n)^b$	Population (%)^b
(d,p)	12	^{232}Th	^{233}Th	4.789	7.81	32	4.99	62
(d,p)	12	^{239}Pu	^{240}Pu	6.534	8.39	28	5.24	54
(d,p)	12	^{242}Pu	^{243}Pu	5.034	8.15	29	5.11	57
(d,p)	13.5	^{237}Np	^{238}Np	5.488	8.28	41	5.25	71
(d,p)	15	^{238}U	^{239}U	4.806	7.84	48	5.04	78
(d,d')	12	^{232}Th	^{232}Th	6.438	8.05	36	5.15	63
(d,d')	15	^{238}U	^{238}U	6.154	8.26	45	5.16	77
(d,t)	15	^{238}U	^{237}U	5.126	8.02	49	5.07	78
$(^3$He,^{3}He$')$	24	^{232}Th	^{232}Th	6.438	8.05	62	5.15	83
$(^3$He,$\alpha)$	24	^{232}Th	^{231}Th	5.118	7.78	73	5.04	82
$(^3$He,$t)$	24	^{232}Th	^{232}Pa	5.549	8.19	70	5.23	70
$(^3$He,$d)$	24	^{232}Th	^{233}Pa	6.529	8.82	62	5.28	86

^{a}from Ref [17]
^{b}from Ref [19]

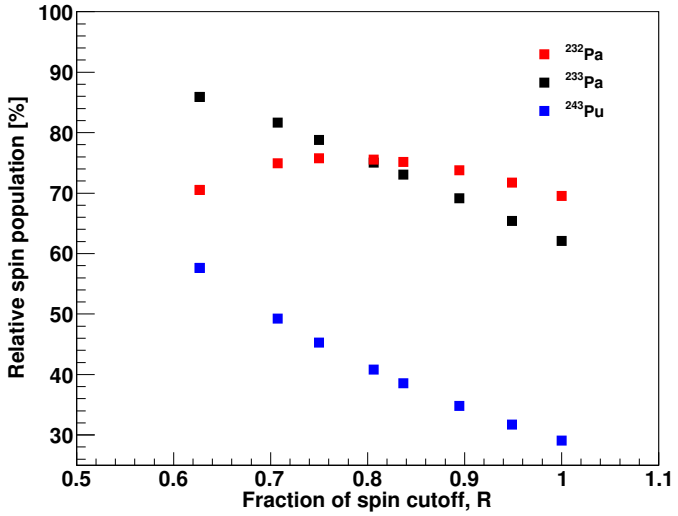

Figure B.9: Variation of the relative spin population as a function of the fraction of spin cutoff from Ref [17].

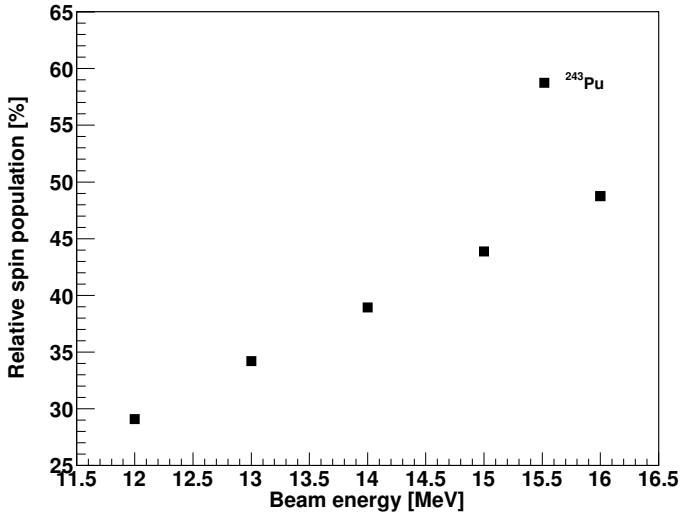

Figure B.10: Evolution of the relative spin population as a function of the beam energy using the spin cutoff parameter from Ref [17].

B.4 Conclusion

The Empire code has been modified in order to calculate relative spin population following charged particle reactions with the spin dependent level density parametrization from Ref[17] and Ref. [19]. As expected in Ref. [8, 114, 123], (d, p) reactions do no populate

all available levels in the actinides and a correction needs to be taken into account to extract the γ-ray strength function using the Oslo method [5].

Better knowledge of the spin cutoff parameter would allow to constrain the range of acceptable values for the relative population of the residual nuclei. Confirmation of the results by an independent method would bring confidence in the calculation and allow for uncertainty estimation.

B.5 Egidy.f

Egidy.f is the file that contains the subroutine ReadEgidy reading the data tables contains the parameters to calculate the spin dependent level density described in Refs.[17, 18, 19]. RO_EGIDY calculates the spin dependent level density for the parametrization from Refs. [17, 18] and RO_EGIDY2009 calculates the spin dependent level density for the parametrization from Ref. [19]. Both RO_EGIDY and RO_EGIDY2009 fill the level density matrix RO($E_x, J, \pi, Nnuc$) used later by EMPIRE to calculate the population in the residual nucleus. $Nnuc$ represents the nucleus id number.

```
1
2  SUBROUTINE ReadEgidy
3    %     COMMON/mas03/Zo(3200),Ao(3200),Elo(3200),Mexpo(3200),
4         &       dMexpo(3200),iio(0:511,0:511)
5          COMMON/rct2/Sno(3200),dSno(3200),Spo(3200),dSpo(3200)
6          COMMON/rct7/Pdo(3200),dPdo(3200),Pno(3200),dPno(3200),
7         &       Ppo(3200),dPpo(3200)
8          REAL Mexpo, dMexpo, S_primeo,Pa_primeo
9          CHARACTER Elo*3,dum1o*1,dum3o*3,dum4o*4,dumo,filnamo*255
10         CHARACTER*64 empiredir
11         INTEGER Zo,Ao,iio,Z0,A0,N0,ieo,idumo
12         DOUBLE PRECISION So,dSo, Pdo, dPdo
13          isig    = 4
14         itemp  = 1
15         Exx    = -1.
16         sig2   = -1.
17         CALL GETENV ('EMPIREDIR', empiredir)
18         WRITE(6,*)'Reading␣file␣mass.mas03'
19         OPEN(20,ERR=98,FILE=trim(empiredir)//'/data/egidy03'
20        &   //'/mass.mas03', STATUS='old')
21         DO i=1,39
22         READ(20,7,ERR=99)dum
23   7     FORMAT(A1)
24         ENDDO
25         DO i=1,3200
26         READ(20,11,END=12,ERR=99)dum1o,idumo,idumo,Zo(i),Ao(i),
27        &                    Elo(i),dum4o,Mexpo(i),dMexpo(i)
28   11    FORMAT(a1,i3,i5,i5,i5,1x,a3,a4,1x,f13.5,f11.5)
29          iio(Ao(i),Zo(i))=i
30         ENDDO
31   12    CONTINUE
32         WRITE(6,*)'Number␣of␣nuclei␣read␣is',i-1,
33        &   '␣with␣last␣(A,Z)␣=␣(', Ao(i-1),',',Zo(i-1),')'
34         WRITE(6,*)'Reading␣file␣rct2␣'
35         OPEN(21,ERR=98,FILE=trim(empiredir)//'/data/egidy03'
36        &   //'/rct2.mas03', STATUS='old')
37         DO i=1,39
38         READ(21,7,ERR=99)dumo
39         ENDDO
```

```
      DO i=1,3200
      READ(21,13,END=14,ERR=99)dum1o,idumo,dum3o,idumo,Sno(i),
     &                         dSno(i),Spo(i),dSpo(i)
 13   FORMAT(a1,i3,1x,a3,i3,1x,2(f10.2,f8.2))
      ENDDO
 14   CONTINUE
      WRITE(6,*)'Number␣of␣nuclei␣read␣is',i-1,
     &          '␣with␣last␣(A,Z)␣=␣(',Ao(i-1),',',Zo(i-1),')'
      WRITE(6,*)'Reading␣file␣rct7␣'
      OPEN(22,ERR=98,FILE=trim(empiredir)//'/data/egidy03'
     &   //'/rct7.mas03', STATUS='old')
      DO i=1,39
      READ(22,7,ERR=99)dumo
      ENDDO
      DO i=1,3200
      READ(22,15,END=16,ERR=99)dum1o,idumo,dum3o,idumo,Pdo(i),
     &      dPdo(i),Pno(i),dPno(i),Ppo(i),dPpo(i)
 15     FORMAT(a1,i3,1x,a3,i3,1x,3(f10.2,f8.2))
      ENDDO
 16   CONTINUE
      WRITE(6,*)'Number␣of␣nuclei␣read␣is',i-1,
     &    '␣with␣last␣(A,Z)␣=␣(',Ao(i-1),',',Zo(i-1),')'
      WRITE(6,*)'␣'
      WRITE(6,*)'Check␣that␣the␣same␣number␣of␣nuclei␣is␣read.'
      WRITE(6,*)'(If␣not,␣mismatch␣will␣give␣wrong␣results.)'
      GOTO 102
 98   WRITE(6,*)'Error␣during␣opening␣file'  C       STOP 99   WRITE(6,101)i
 101  FORMAT('Error␣during␣reading␣line:␣',I4)
 102  END

      SUBROUTINE RO_EGIDY(NNuc)
CCC
CCC   ********************************************************************
CCC   *                                                     CLASS:PPU*
CCC   *                          RO_EGIDY                              *
CCC   *                                                                *
CCC   *                                                                *
CCC   * CALCULATES TABLE OF ENERGY AND SPIN DEPENDENT LEVEL DENSITIES *
CCC   * FROM EGIDY AND BUCURESCU 2006                                  *
CCC   * Phys. Rev. C 72, 044311 - Published 27 October 2005;          *
CCC   * Erratum Phys. Rev. C 73, 049901 (2006)                        *
CCC   *                                                                *
CCC   * INPUT:                                                        *
CCC   *  NNUC - index of the nucleus                                   *
CCC   *                                                                *
CCC   * OUTPUT:RO(.,.,NNUC) - LEVEL DENSITIES                         *
CCC   *                                                                *
CCC   *                                                                *
CCC   ********************************************************************
      INCLUDE 'dimension.h'
```

```
90          INCLUDE 'global.h'
91          COMMON/mas03/Zo(3200),Ao(3200),Elo(3200),Mexpo(3200),
92         &       dMexpo(3200),iio(0:511,0:511)
93          COMMON/rct2/Sno(3200),dSno(3200),Spo(3200),dSpo(3200)
94          COMMON/rct7/Pdo(3200),dPdo(3200),Pno(3200),dPno(3200),
95         &       Ppo(3200),dPpo(3200)
96          REAL Mexpo, dMexpo, S_primeo,Pa_primeo
97          CHARACTER Elo*3,dum1o*1,dum3o*3,dum4o*4,dumo,filnamo*255
98          INTEGER Zo,Ao,iio,Z0,A0,N0,ieo,idumo,io
99          DOUBLE PRECISION So,dSo, Pdo, dPdo
100         REAL Eex ! excitation energy
101         DOUBLE PRECISION aa, a_asympt, roU, roJ, roPi, Temp, scof2
102 C
103 C FROM ROEMP
104 C COMMON variables
105 C
106         REAL*8 TCRt, ECOnd, ACRt, UCRt, DETcrt, SCR, ACR, ATIl ! CRIT
107         REAL*8 AP1, AP2, GAMma, DEL, DELp, BF, A23, A2       ! PARAM
108         INTEGER NLWst                                        ! PARAM
109         COMMON /CRIT / TCRt, ECOnd, ACRt, UCRt, DETcrt, SCR, ACR, ATIl
110         COMMON /PARAM / AP1, AP2, GAMma, DEL, DELp, BF, A23, A2, NLWst
111 C
112 C Dummy arguments
113 C
114         INTEGER Nnuc
115 C
116 C Local variables
117 C
118         REAL*8 aj, defit , dshif , dshift , ellq , pi2, rotemp, Ecrt
119         REAL FLOAT
120         INTEGER iz, kk, nplot
121         INTEGER INT
122         pi2 = PI*PI
123         dshift =0.0d0
124 C A, Z, N of nucleus
125         A0 = INT(A(Nnuc))
126         Z0 = INT(Z(Nnuc))
127         A23 = A(Nnuc)**0.666667d0
128 C  check if the nucleus is even-even/odd-even/odd-odd   N0=A0-Z0
129         IF((N0/2)*2.EQ.N0.AND.(Z0/2)*2.EQ.Z0)ieo=0 ! even-even nucleus
130         IF((N0/2)*2.NE.N0.AND.(Z0/2)*2.EQ.Z0)ieo=1 ! even-Z odd-N
131         IF((N0/2)*2.EQ.N0.AND.(Z0/2)*2.NE.Z0)ieo=2 ! odd-Z even-N
132         IF((N0/2)*2.NE.N0.AND.(Z0/2)*2.NE.Z0)ieo=3 ! odd-odd nucleus
133         io=iio(A0,Z0)
134 C  pariring  correction  Sprime from Eq (10) and (11)
135 C backshifted  Energy parameter E1 from (14) or (16) see  Correction  for  pi  parameters
136         IF(ieo.EQ.0)THEN
137         E1= -0.48 -0.5*(Pdo(io)/1000.) + 0.29*dSo
138         Sprime=So-0.5*(Pdo(io)/1000.)
139         ENDIF
```

```
140         IF(ieo.EQ.1)THEN
141         E1= -0.57 -0.5*(Pdo(io)/1000.) + 0.70*dSo
142         Sprime=So
143         ENDIF
144         IF(ieo.EQ.2)THEN
145         E1= -0.57 +0.5*(Pdo(io)/1000.) - 0.70*dSo
146         Sprime=So
147         ENDIF
148         IF(ieo.EQ.3)THEN
149         E1= -0.24 +0.5*(Pdo(io)/1000.) + 0.29*dSo
150         Sprime=So+0.5*(Pdo(io)/1000.)
151         ENDIF
152 C       for energy independent level density parameter BSFG
153 C       aa=FLOAT(A0)*(0.127 + 4.98E-03*Sprime -8.95E-05*FLOAT(A0))
154 C       for energy dependent level density parameter BSFG-ED, aa will be the asymptotic level density
        parameter
155           a_asympt=FLOAT(A0)*(0.127 -8.95E-05*FLOAT(A0))
156           C calculating the level density as a function of the excitation energy
157           DO kk = 1, NEX(Nnuc)
158           Eex = EX(Kk,Nnuc)
159           U=Eex-E1
160 C calculation of the level density parameter from its asymptotic value from Eq(5)
161           aa = a_asympt*(1 + Sprime/(Eex-E1)*(1-exp(-0.06*(Eex-E1))))
162 C gamma taken to be 0.06 Mev-1
163           Temp=(1.+sqrt(1.+4.*aa*(Eex-E1)))/(2.*aa)
164           scof2=0.0146*A0**(5./3.)*Temp
165           roPi=0.5
166           roU=exp(2.*SQRT(aa*U))/(aa**(1./4.)*(U**(5./4.)))
167           roU=roU/(12.*sqrt(2.)*2.)
168           DO i = 1, NLW
169           Aj = REAL(i) + HIS(Nnuc)
170           roJ=(2.*Aj+1.)/scof2**1.5
171       &       *exp(-(Aj+1/2.)**2/(2.*scof2))
172           rotemp=roPi*roU*roJ
173           RO(Kk,i,1,Nnuc) = rotemp
174           RO(Kk,i,2,Nnuc) = rotemp
175           ENDDO
176         ENDDO
177         RETURN
178         END
179
180
181
182       SUBROUTINE RO_EGIDY2009(NNuc)
183 CCC
184 CCC  ***************************************************************
185 CCC  *                                                    CLASS:PPU*
186 CCC  *                          RO_EGIDY                      *
187 CCC  *                                                        *
188 CCC  *                                                        *
```

```
CCC  * CALCULATES TABLE OF ENERGY AND SPIN DEPENDENT LEVEL DENSITIES *
CCC  * FROM EGIDY AND BUCURESCU 2009                                  *
CCC  * Phys. Rev. C 80, 054310                                       *
CCC  *                                                               *
CCC  * INPUT:                                                       *
CCC  *  NNUC - index of the nucleus                                  *
CCC  *                                                               *
CCC  * OUTPUT:RO(.,.,NNUC) - LEVEL DENSITIES                        *
CCC  *                                                               *
CCC  *                                                               *
CCC  ****************************************************************
       INCLUDE 'dimension.h'
       INCLUDE 'global.h'

       COMMON/mas03/Zo(3200),Ao(3200),Elo(3200),Mexpo(3200),
      &      dMexpo(3200),iio(0:511,0:511)
       COMMON/rct2/Sno(3200),dSno(3200),Spo(3200),dSpo(3200)
       COMMON/rct7/Pdo(3200),dPdo(3200),Pno(3200),dPno(3200),
      &      Ppo(3200),dPpo(3200)
       REAL Mexpo, dMexpo, S_primeo,Pa_primeo
       CHARACTER Elo*3,dum1o*1,dum3o*3,dum4o*4,dumo,filnamo*255
       INTEGER Zo,Ao,iio,Z0,A0,N0,ieo,idumo,io
       DOUBLE PRECISION So,dSo, Pdo, dPdo
       REAL Eex ! excitation energy
       DOUBLE PRECISION aa, a_asympt, roU, roJ, roPi, Temp, scof2
C
C COMMON variables
C
       REAL*8 TCRt, ECOnd, ACRt, UCRt, DETcrt, SCR, ACR, ATIl ! CRIT
       REAL*8 AP1, AP2, GAMma, DEL, DELp, BF, A23, A2       ! PARAM
       INTEGER NLWst                                        ! PARAM
       COMMON /CRIT / TCRt, ECOnd, ACRt, UCRt, DETcrt, SCR, ACR, ATIl
       COMMON /PARAM / AP1, AP2, GAMma, DEL, DELp, BF, A23, A2, NLWst
       INTEGER Nnuc
C
C Local variables
C
       REAL*8 aj, defit, dshif, dshift, ellq, pi2, rotemp, Ecrt
       REAL FLOAT
       INTEGER iz, kk, nplot
       INTEGER INT
       pi2 = PI*PI
       dshift =0.0d0
C A, Z, N of nucleus
       A0 = INT(A(Nnuc))
       Z0 = INT(Z(Nnuc))
       A23 = A(Nnuc)**0.666667d0

C  check if the nucleus is even-even/odd-even/odd-odd
       N0=A0-Z0
```

```
239         IF((N0/2)*2.EQ.N0.AND.(Z0/2)*2.EQ.Z0)ieo=0 ! even-even nucleus
240       IF((N0/2)*2.NE.N0.AND.(Z0/2)*2.EQ.Z0)ieo=1 ! even-Z odd-N
241       IF((N0/2)*2.EQ.N0.AND.(Z0/2)*2.NE.Z0)ieo=2 ! odd-Z even-N
242       IF((N0/2)*2.NE.N0.AND.(Z0/2)*2.NE.Z0)ieo=3 ! odd-odd nucleus
243       io=iio(A0,Z0)
244
245 C VALUES FROM E&B2009
246         Pa_prime = Pdo(io)/1000.
247         IF(ieo.EQ.0.OR.ieo.EQ.1)Pa_prime = -Pdo(io)/1000.      ! See page 3 of E&B2009
248         S_prime = REAL(So) + 0.5 * Pa_prime     !Eq. (11) E&B2009
249         aa = (0.199 + 0.0096*S_prime)*FLOAT(A0)**0.869
250         E1 = -0.381 + 0.5  *Pa_prime
251 C calculating the level density as a function of the excitation energy
252         DO kk = 1, NEX(Nnuc)
253         Eex = EX(Kk,Nnuc)
254         U=Eex-E1
255         Temp=(1.+sqrt(1.+4.*aa*(Eex-E1)))/(2.*aa)
256         scof2=0.391 *(FLOAT(A0)**(0.675))*(U-(E1+0.381))**0.312
257         roPi=0.5
258         roU=exp(2.*SQRT(aa*U))/(aa**(1./4.)*(U**(5./4.)))
259         roU=roU/(12.*sqrt(2.)*2.)
260           DO i = 1, NLW
261           Aj = REAL(i) + HIS(Nnuc)
262           roJ=(2.*Aj+1.)/scof2**1.5
263          &      *exp(-(Aj+1/2.)**2/(2.*scof2))
264           rotemp=roPi*roU*roJ
265           RO(Kk,i,1,Nnuc) = rotemp
266           RO(Kk,i,2,Nnuc) = rotemp
267           ENDDO
268         ENDDO
269         RETURN
270         END
271
272
273
274
275       SUBROUTINE ShellCorr(So,A0,Z0)
276 CCC
277 CCC  ****************************************************************
278 CCC  *                                                              *
279 CCC  * Calculates the Shell correction S(Z,N) from Eq. (7),(9) from *
280 CCC  * FROM EGIDY AND BUCURESCU 2006                                *
281 CCC  * Phys. Rev. C 72, 044311 - Published 27 October 2005;         *
282 CCC  * Erratum Phys. Rev. C 73, 049901 (2006)                       *
283 CCC  *                                                              *
284 CCC  ****************************************************************
285         COMMON/mas03/Zo(3200),Ao(3200),Elo(3200),Mexpo(3200),
286       &       dMexpo(3200),iio(0:511,0:511)
287         REAL Mexpo, dMexpo
288         DOUBLE PRECISION Mn,Mp,u,eps0,e2,rZ,rA,rN,r0,avol,asf,asym,
```

```
289         &  ass,Eb_on_A,pi,So,Mtheo
290          CHARACTER Elo*3
291          INTEGER Zo,Ao,Z0,A0,iio
292          i=iio(A0,Z0)
293          rZ=FLOAT(Z0)
294          rA=FLOAT(A0)
295          rN=rA-rZ
296          u= 931.494043
297          Mn= (8071.323/1000.)+u
298          Mp= (7288.969/1000.)+u
299          pi=ACOS(-1.)
300          avol=-15.65
301          asf=17.63
302          asym=27.72
303          ass=-25.60
304          r0=1.233
305          e2=(1.60217653E-19)**2  ! e**2 in units of C**2
306          eps0=8.854187817E-12    ! epsilon_0 in units of F/m
307          e2=e2/(4.*pi*eps0)
308          e2=e2*6.24150947E+12
309          e2=e2*(1.E+15)
310          Eb_on_A=-(avol+(asf*(rA**(-1./3.)))+((3.*e2)/(5.*r0))
311         &       *(rZ**2)*(rA**(-4./3.))+(asym+ass*(rA**(-1./3.)))
312         &       *((rN-rZ)/rA)**2)
313          Mtheo = rN*Mn + rZ*Mp - rA*(Eb_on_A +u)
314          So = (Mexpo(i)/1000.)-Mtheo
315          RETURN
316          END
317
318        SUBROUTINE dSdA(dSo,A0,Z0)
319 CCC
320 CCC  ****************************************************************
321 CCC  *                                                              *
322 CCC  * Calculates the derivative of the Shell correction S(Z,N) with *
323 CCC  * respect to the number of nucleons A, from Eq. (12) from       *
324 CCC  * FROM EGIDY AND BUCURESCU 2006                                *
325 CCC  * Phys. Rev. C 72, 044311 - Published 27 October 2005;         *
326 CCC  * Erratum Phys. Rev. C 73, 049901 (2006)                       *
327 CCC  *                                                              *
328 CCC  ****************************************************************
329          INTEGER A0,Z0
330          DOUBLE PRECISION S1,S2,dSo
331          CALL ShellCorr(S1,A0+2,Z0+1)
332          CALL ShellCorr(S2,A0-2,Z0-1)
333          dSo=(1./4.)*(S1-S2)
334          RETURN
335          END
```

Appendix C

TALYS calculations of the ^{242}Pu(n,γ) cross section

C.1 Default input

The default TALYS input is given below. The average neutron resonance spacing parameter D_0 and the average radiative capture width Γ_γ calculated by TALYS do not reproduce experimentally measured data. A normalization factor described in Section 5.6.3, $G_{\text{norm}} = 3.22$, is introduced in order to reproduce the average radiative capture width Γ_γ. By default, Talys tries to reproduce the RIPL-3 [25] tabulated $D_0 = 13.5(15)$ eV and $\Gamma_\gamma = 25(4)$ meV.

Table C.1: Default TALYS output of the D_0 and Γ_γ parameters.

	D_0 (eV)	Γ_γ (meV)
TALYS	12.7	7.8
Experimental	13.5(15)[a]	25(4)[a]

[a]Reference [25].

```
# # TALYS INPUT FILE
# 242Pu(n,g)243Pu

# description of the reaction
 projectile  n
element pu
mass 242
# list of energies for which we want the cross sections
energy  energies.txt

# outputs to be printed in the output file
 outlevels  y
```

```
outdensity y
outgamma y
astro n
```

C.2 The use of experimentally measured level density and γ-ray strength function

Several level density models are available in TALYS via the **ldmodel** keyword. In order to use our experimentally measured level density, **ldmodel 4**, which calls Goriely's tables, is used. The level density tables are available in the directory:
$TALYS$/structure/density/ground/goriely/.
Each element has a file containing level density tables for several isotopes. For example, the tables for Pu are contained in the **z094.tab** file and contains the spin dependent level density at a given excitation energy for isotopes 202-322. The excitation energy varies from $E_x = 0.25\,\text{MeV}$ to $E_x = 150\,\text{MeV}$ with variable energy binning. The table for ^{243}Pu is modified to include the measured level density. The experimentally measured level density (see Section 4.3.1) is implemented in the ^{243}Pu table using the constant temperature formula from Eq. (2.7). The spin distribution is given by the Eq. (B.3) with the spin cutoff parameter calculated using the parametrization from Egidy and Bucurescu[17, 18] given in Eq. (B.6). The constant temperature is slightly modified in order to reproduce the neutron resonance spacing parameter D_0 from the Ref. [110]. Table C.2 gives the parameters used to calculate the level density used as input for the TALYS calculation. The D_0 parameter calculated by TALYS is strongly dependent on the constant temperature.

Table C.2: Parameters used to calculate the ^{243}Pu energy and spin dependent level density, which is used as input for the TALYS calculation. The D_0 value is calculated by TALYS and the constant temperature T_{CT} is modified until agreement is found with the experimental value from Ref. [110].

a (MeV^{-1})	E1 (MeV)	$\sigma(S_n)$	T_{CT} (MeV)	E_0 (MeV)	D_0 (eV)
25.82[a]	-0.45[a]	8.15[a]	0.3833	-0.95	17

[a]Estimated from systematics [18].
[b]Estimated from systematics [19].

The Giant Electric Dipole Resonance (GEDR) parameters are implemented in TALYS using the EGLO model (see Section 2.2.6), specified by the keyword **strength 1**. The parameters of the GEDR are specified using the keywords **egr, sgr, ggr** for respectively the centroid of the resonance, its cross section, and its width. The temperature dependence of the EGLO model is modified in the source file **$TALYS$/source/fstrength.f**

Table C.3: Resonance parameters used to describe the γ-ray strength function in TALYS. The temperature of the EGLO tail of the GEDR is set constant and modified to reproduce the average radiative capture width Γ_γ.

	ω_1 (MeV)	σ_1 (mb)	Γ_1 (MeV)	ω_2 (MeV)	σ_2 (mb)	Γ_2 (MeV)	T_f (MeV)
GEDR	11.1	290	3.2	14.2	340	5.5	0.3860
PYGMY	4.4	9	1.0	7.4	20	1.3	
SCISSORS	1.99	0.45	0.60	2.81	0.51	0.83	

The temperature is set constant. Parameters for the two pygmy resonances and the scissors resonances are added in the fstrength.f file using standard Lorentzians.

To avoid TALYS using a normalization factor, it is forced to 1 via the keyword **gnorm 1.** Experimental values of the average radiative capture width Γ_γ is reproduced by slightly varying the constant temperature of GEDR low energy tail.

Finally, the s-wave strength S_0 and scattering radius R' are also calculated by TALYS and is influenced by the optical model parameters. The output gives for a neutron energy $E_n = 32.5\,\text{eV}$, $S_0 = 1.02 \times 10^{-4}\,\text{eV}^{1/2}$ and $R' = 9.64\,\text{fm}$. Those parameters fall within error bars of experimentally measured values [110, 112, 25, 134]. This should only be considered as a safety check and no extended work as been done since all evaluated S_0 and R' values from ^{229}Th to ^{249}Cf coincide within errors with their average: $\langle S_0 \rangle = 1 \times 10^{-4}\,\text{eV}^{1/2}$ and $\langle R' \rangle = 9.65$ fm [134].

The TALYS input file is shown below:

```
# # TALYS INPUT FILE
# 242Pu(n,g)243Pu

# description of the reaction
 projectile  n
element pu
mass 242
energy  energies.txt

# default mass model, from Goriely HFB-Skyrme tables
massmodel 2
# lower limit value to consider the transmission coefficient
transeps 1.00E-15
# limit in mb for considering cross sections in the reaction
xseps 1.00E-25
# limit in mb for considering population cross sections in the multiple emission calculation
popeps 1.00E-25

# number of included discrete levels for all residual nuclides that are considered in Hauser-
    Feshbach decay and the gamma-ray cascade. For nuclides that do not have maxlevelsres available in
     the discrete level file, we take the last known level as the last discrete level in our
    calculation
```

```
maxlevelsres 20

# NUCLEAR LEVEL DENSITY MODEL
# LDMODEL 4 is chosen but the tables are modified with the experimentally measured data
# SHIFT AND SLOPE ADJUSTMENT SHOULD BE ZERO
ldmodel 4
ctable 94 243 0.0
ptable 94 243 0.0

# Flag to invoke the dispersive optical model
dispersion y

# GSF-MODEL: TWEAKED GENERALIZED LORENTZIAN
# see fstrength.f source file
strength 1
gnorm 1.
# ADJUSTMENT OF GEDR PARAMETERS
egr 94 243 11.1 E1 1
sgr 94 243 290 E1 1
ggr 94 243 3.2 E1 1
egr 94 243 14.15 E1 2
sgr 94 243 340 E1 2
ggr 94 243 5.5 E1 2
# canceling the default m1 GDR by forcing small cross section
egr 94 243 4.6 M1
sgr 94 243 0.001 M1
ggr 94 243 1 M1

# Fake resonance with inexistant cross section
# forces TALYS to read the additional pygmy resonance section in fstrength.f where the observed
    pygmy + Scissors mode are added
epr 94 243 15 E1
spr 94 243 0.001 E1
gpr 94 243 1 E1

outdiscrete y
preequilibrium y
fileresidual y
outbasic y
outlevels y
outdensity y
outgamma y
astro n
```

Bibliography

[1] C.F. von Weizsäcker. Zur theorie der kernmassen. *Zeitschrift für Physik A Hadrons and Nuclei*, 96(7):431–458, 1935.

[2] M. Goeppert-Mayer and J.H.D. Jensen. *Elementary theory of nuclear shell structure*. John Wiley & Sons, 1955.

[3] M. Guttormsen, T. Ramsøy, and J. Rekstad. The first generation of γ-rays from hot nuclei. *Nuclear Instruments and Methods in Physics Research Section A Accelerators Spectrometers Detectors and Associated Equipment*, (3):518–523, 1987.

[4] M. Guttormsen, T.S. Tveter, L. Bergholt, F. Ingebretsen, and J. Rekstad. The unfolding of continuum γ-ray spectra. *Nuclear Instruments and Methods in Physics Research Section A: Accelerators, Spectrometers, Detectors and Associated Equipment*, 374(3):371–376, 1996.

[5] A. Schiller, L. Bergholt, M. Guttormsen, et al. Extraction of level density and γ strength function from primary γ spectra. *Nuclear Instruments and Methods in Physics Research Section A: Accelerators, Spectrometers, Detectors and Associated Equipment*, 447(3):498–511, 2000.

[6] M. Guttormsen, B. Jurado, J.N. Wilson, et al. Constant-temperature level densities in the quasicontinuum of Th and U isotopes. *Physical Review C*, 88(2):024307, 2013.

[7] D. Frekers, H.J. Wörtche, A. Richter, et al. Spin excitations in the deformed nuclei ^{154}Sm, ^{158}Gd and ^{168}Er. *Physics Letters B*, 244(2):178–182, 1990.

[8] M. Guttormsen, L.A. Bernstein, A. Görgen, et al. Scissors resonance in the quasicontinuum of Th, Pa, and U isotopes. *Physical Review C*, 89(1):014302, 2014.

[9] W. Hauser and H. Feshbach. The inelastic scattering of neutrons. *Physical Review*, 87(2):366, 1952.

[10] M. Arnould, S. Goriely, and K. Takahashi. The r-process of stellar nucleosynthesis: Astrophysics and nuclear physics achievements and mysteries. *Physics Reports*, 450(4):97–213, 2007.

[11] M.B. Chadwick, M. Herman, P. Obložinskỳ, et al. ENDF/B-VII.1 nuclear data for science and technology: cross sections, covariances, fission product yields and decay data. *Nuclear Data Sheets*, 112(12):2887–2996, 2011.

[12] G. Aliberti, G. Palmiotti, M. Salvatores, et al. Nuclear data sensitivity, uncertainty and target accuracy assessment for future nuclear systems. *Annals of Nuclear Energy*, 33(8):700–733, 2006.

[13] S. Krewald and J. Speth. Pygmy dipole resonances. *International Journal of Modern Physics E*, 18(07):1425–1451, 2009.

[14] H.A. Bethe. An attempt to calculate the number of energy levels of a heavy nucleus. *Physical Review*, 50(4):332, 1936.

[15] T. Ericson. The statistical model and nuclear level densities. *Advances in Physics*, 9(36):425–511, 1960.

[16] W. Dilg, W. Schantl, H. Vonach, and M. Uhl. Level density parameters for the back-shifted Fermi gas model in the mass range 40<A<250. *Nuclear Physics A*, 217(2):269–298, 1973.

[17] T. von Egidy and D. Bucurescu. Systematics of nuclear level density parameters. *Physical Review C*, 72(4):044311, 2005.

[18] T. von Egidy and D. Bucurescu. Erratum: Systematics of nuclear level density parameters [Phys. Rev. C 72, 044311 (2005)]. *Physical Review C*, 73(4):049901, 2006.

[19] T. Von Egidy and D. Bucurescu. Experimental energy-dependent nuclear spin distributions. *Physical Review C*, 80(5):054310, 2009.

[20] A. Gilbert and A.G.W. Cameron. A composite nuclear-level density formula with shell corrections. *Canadian Journal of Physics*, 43(8):1446–1496, 1965.

[21] A.V. Ignatyuk, K.K. Istekov, and G.N. Smirenkin. Role of collective effects in the systematics of nuclear level densities. *Sov. J. Nucl. Phys.*, 29(4), 1979.

[22] A.V. Ignatyuk, J.L. Weil, S. Raman, and S. Kahane. Density of discrete levels in ^{116}Sn. *Physical Review C*, 47(4):1504, 1993.

[23] J.R. Huizenga and L.G. Moretto. Nuclear level densities. *Annual Review of Nuclear Science*, 22(1):427–464, 1972.

[24] A.S. Iljinov, M.V. Mebel, N. Bianchi, et al. Phenomenological statistical analysis of level densities, decay widths and lifetimes of excited nuclei. *Nuclear Physics A*, 543(3):517–557, 1992.

[25] R. Capote, M. Herman, P. Obložinskỳ, et al. RIPL–reference input parameter library for calculation of nuclear reactions and nuclear data evaluations. *Nuclear Data Sheets*, 110(12):3107–3214, 2009.

[26] A.J. Koning, S. Hilaire, and M.C. Duijvestijn. TALYS-1.0. In *International Conference on Nuclear Data for Science and Technology*, pages 211–214. EDP Sciences, 2007.

[27] S. Binder, J. Langhammer, A. Calci, and R. Roth. Ab initio path to heavy nuclei. *Physics Letters B*, 736:119–123, 2014.

[28] M. Hillman and J.R. Grover. Shell-model combinatorial calculations of nuclear level densities. *Physical Review*, 185(4):1303, 1969.

[29] S. Hilaire, J.P. Delaroche, and M. Girod. Combinatorial nuclear level densities based on the Gogny nucleon-nucleon effective interaction. *The European Physical Journal A-Hadrons and Nuclei*, 12(2):169–184, 2001.

[30] S. Uhrenholt, H.and Åberg, A. Dobrowolski, T. Døssing, T. Ichikawa, and P. Möller. Combinatorial nuclear level-density model. *Nuclear Physics A*, 913:127–156, 2013.

[31] S. Goriely, S. Hilaire, and A.J. Koning. Improved microscopic nuclear level densities within the Hartree-Fock-Bogoliubov plus combinatorial method. *Physical Review C*, 78(6):064307, 2008.

[32] S. Siem, M. Guttormsen, K. Ingeberg, et al. Level densities and γ-strength functions in ^{148,149}Sm. *Physical Review C*, 65(4):044318, 2002.

[33] M. Guttormsen, A. Bagheri, R. Chankova, et al. Thermal properties and radiative strengths in ^{160,161,162}Dy. *Physical Review C*, 68(6):064306, 2003.

[34] E. Melby, M. Guttormsen, J. Rekstad, et al. Thermal and electromagnetic properties of ^{166}Er and ^{167}Er. *Physical Review C*, 63(4):044309, 2001.

[35] A. Schiller, A. Bjerve, M. Guttormsen, et al. Critical temperature for quenching of pair correlations. *Physical Review C*, 63(2):021306, 2001.

[36] G. Sugiyama and S.E. Koonin. Auxiliary field Monte-Carlo for quantum many-body ground states. *Annals of Physics*, 168(1):1–26, 1986.

[37] S.E. Koonin, D.J. Dean, and K. Langanke. Shell model monte carlo methods. *Physics Reports*, 278(1):1–77, 1997.

[38] Y. Alhassid, M. Bonett-Matiz, S. Liu, and H. Nakada. Direct microscopic calculation of nuclear level densities in the shell model Monte Carlo approach. *Physical Review C*, 92(2):024307, 2015.

[39] T. Ericson and T. Mayer-Kuckuk. Fluctuations in nuclear reactions. *Annu. Rev. Nucl. Sci.*, 16(CERN-TH-686):183–206, 1966.

[40] V. Mishra, N. Boukharouba, S.M. Grimes, et al. Determination of the level density of Si 29 from Ericson fluctuations. *Physical Review C*, 44(6):2419, 1991.

[41] A.V. Voinov, S.M. Grimes, U. Agvaanluvsan, et al. Level density of ^{56}Fe and low-energy enhancement of γ-strength function. *Physical Review C*, 74(1):014314, 2006.

[42] D.M. Brink. Ph.D. Thesis, 1955.

[43] P. Axel. Electric dipole ground-state transition width strength function and 7-MeV photon interactions. *Physical Review*, 126(2):671, 1962.

[44] K. Shibata, O. Iwamoto, T. Nakagawa, et al. JENDL-4.0: a new library for nuclear science and engineering. *Journal of Nuclear Science and Technology*, 48(1):1–30, 2011.

[45] O. Iwamoto. Development of a comprehensive code for nuclear data evaluation, CCONE, and validation using neutron-induced cross sections for uranium isotopes. *Journal of nuclear science and technology*, 44(5):687–697, 2007.

[46] A.J. Koning and D. Rochman. Modern nuclear data evaluation with the TALYS code system. *Nuclear Data Sheets*, 113(12):2841–2934, 2012.

[47] E. Fermi. Nuclear physics. In *A course given by Enrico Fermi at the University of Chicago, 1949, Chicago: University of Chicago Press, 1950, Rev. ed.*, volume 1, 1950.

[48] J. Suhonen. *From Nucleons to Nucleus: Concepts of Microscopic Nuclear Theory*. Springer Science & Business Media, 2007.

[49] E. Beardsworth, R. Hensler, J.W. Tape, et al. Double Gamma Decay in ^{40}Ca. *Physical Review C*, 8(1):216, 1973.

[50] B.A. Watson, T.T. Bardin, J.A. Becker, and T.R. Fisher. Two-Photon Decay of the 6.05-MeV State of ^{16}O. *Physical Review Letters*, 35(20):1333, 1975.

[51] J. Schirmer, D. Habs, R. Kroth, et al. Double Gamma Decay in ^{40}Ca and ^{90}Zr. *Physical Review Letters*, 53(20):1897, 1984.

[52] G.C. Baldwin and G.S. Klaiber. Photo-fission in heavy elements. *Physical Review*, 71(1):3, 1947.

[53] J. Speth and A. van der Woude. Giant resonances in nuclei. *Reports on Progress in Physics*, 44(7):719, 1981.

[54] A. Van der Woude. Giant resonances. *Progress in Particle and Nuclear Physics*, 18:217–293, 1987.

[55] Y. Suzuki, K. Ikeda, and H. Sato. New type of dipole vibration in Nuclei. *Progress of Theoretical Physics*, 83(2):180–184, 1990.

[56] A.S. Adekola, C.T. Angell, S.L. Hammond, et al. Discovery of low-lying $E1$ and $M1$ strengths in ^{232}Th. *Physical Review C*, 83(3):034615, 2011.

[57] K. Heyde, P. von Neumann-Cosel, and A. Richter. Magnetic dipole excitations in nuclei: Elementary modes of nucleonic motion. *Reviews of Modern Physics*, 82(3):2365, 2010.

[58] E.B. Balbutsev, I.V. Molodtsova, and P. Schuck. Orbital and spin scissors modes in superfluid nuclei. *Physical Review C*, 91(6):064312, 2015.

[59] E. Lipparini and S. Stringari. Sum rules and giant resonances in nuclei. *Physics Reports*, 175(3):103–261, 1989.

[60] J. Enders, P. von Neumann-Cosel, C. Rangacharyulu, and A. Richter. Parameter-free description of orbital magnetic dipole strength. *Physical Review C*, 71(1):6342, 2005.

[61] G.A. Bartholomew. Neutron capture gamma rays. *Annual review of nuclear science*, 11(1):259–302, 1961.

[62] A.F. Fantina, E. Khan, G. Colò, N. Paar, and D. Vretenar. Stellar electron-capture rates on nuclei based on a microscopic Skyrme functional. *Physical Review C*, 86(3):035805, 2012.

[63] M. Guttormsen, A.C. Larsen, A. Görgen, et al. Validity of the Generalized Brink-Axel Hypothesis in ^{238}Np. *Physical Review Letters*, 116(1):012502, 2016.

[64] M.S. Hussein, B.V. Carlson, and L.F. Canto. Multiple giant resonances in nuclei: their excitation and decay. *Nuclear Physics A*, 731:163–174, 2004.

[65] L. Netterdon, A. Endres, S. Goriely, et al. Experimental constraints on the γ-ray strength function in ^{90}Zr using partial cross sections of the reaction. *Physics Letters B*, 744:358–362, 2015.

[66] G.W. Misch, G.M. Fuller, and B.A. Brown. Modification of the Brink-Axel hypothesis for high-temperature nuclear weak interactions. *Physical Review C*, 90(6):065808, 2014.

[67] B.L. Berman and S.C. Fultz. Measurements of the giant dipole resonance with monoenergetic photons. *Reviews of Modern physics*, 47(3):713, 1975.

[68] S.S. Dietrich and B.L. Berman. Atlas of photoneutron cross sections obtained with monoenergetic photons. *Atomic Data and Nuclear Data Tables*, 38(2):199–338, 1988.

[69] G.A. Bartholomew, E.D. Earle, A.J. Ferguson, J.W. Knowles, and M.A. Lone. Gamma-ray strength functions. In *Advances in Nuclear Physics*, pages 229–324. Springer, 1973.

[70] C.M. McCullagh, M.L. Stelts, and R.E. Chrien. Dipole radiative strength functions from resonance neutron capture. *Physical Review C*, 23(4):1394, 1981.

[71] J. Kopecky and M. Uhl. Test of gamma-ray strength functions in nuclear reaction model calculations. *Physical Review C*, 41(5):1941, 1990.

[72] F. Bečvář, P. Cejnar, R.E. Chrien, and J. Kopeckỳ. Test of photon strength functions by a method of two-step cascades. *Physical Review C*, 46(4):1276, 1992.

[73] C.B. Dover, R.H. Lemmer, and F.J.W. Hahne. Damping of nuclear dipole states. *Annals of Physics*, 70(2):458–506, 1972.

[74] J. Kopecky and R.E. Chrien. Observation of the $M1$ giant resonance by resonance averaging in ^{106}Pd. *Nuclear Physics A*, 468(2):285–300, 1987.

[75] M. Uhl and J. Kopecky. Gamma-ray strength function models and their parameterization. *INDC (NDS)-335 (May 1995)*, page 157, 1995.

[76] P. Ring, L.M. Robledo, J.L. Egido, and M. Faber. Microscopic theory of the isovector dipole resonance at high angular momenta. *Nuclear Physics A*, 419(2):261–294, 1984.

[77] J.L. Egido and H.A. Weidenmüller. Linear-response calculation of electromagnetic strength functions for hot, rotating nuclei. *Physical Review C*, 39(6):2398, 1989.

[78] J.L. Egido and P. Ring. The decay of hot nuclei. *Journal of Physics G: Nuclear and Particle Physics*, 19(1):1, 1993.

[79] G.M. Gurevich, L.E. Lazareva, V.M. Mazur, G.V. Solodukhov, and B.A. Tulupov. Giant resonance in the total photoabsorption cross section of Z=90 nuclei. *Nuclear Physics A*, 273(2):326–340, 1976.

[80] S. Goriely and E. Khan. Large-scale QRPA calculation of E1-strength and its impact on the neutron capture cross section. *Nuclear Physics A*, 706(1):217–232, 2002.

[81] F. Knapp, N.L. Iudice, P. Veselỳ, et al. Self-consistent studies of the dipole response in neutron rich nuclei using realistic potentials. In *Journal of Physics: Conference Series*, volume 580, page 012055. IOP Publishing, 2015.

[82] E.G. Fuller. *Photonuclear reaction data, 1973*. Number 380. US National Bureau of Standards; for sale by the Supt. of Docs., US Govt. Print. Off., 1973.

[83] P. Axel, K. Min, N. Stein, and D.C. Sutton. New Resonances in Photon Transition Strength Functions. *Physical Review Letters*, 10(7):299, 1963.

[84] P. Axel, K.K. Min, and D.C. Sutton. Intermediate structure in the photon interaction cross sections of Sn and Zr. *Physical Review C*, 2(2):689, 1970.

[85] J. Kopecky, M. Uhl, and R.E. Chrien. Radiative strength in the compound nucleus ^{157}Gd. *Physical Review C*, 47(1):312, 1993.

[86] A. Voinov, S.M. Grimes, C.R. Brune, et al. γ-strength functions in ^{60}Ni from two-step cascades following proton capture. *Physical Review C*, 81(2):024319, 2010.

[87] A. Spyrou, S.N. Liddick, A.C. Larsen, et al. Novel technique for Constraining r-Process (n,γ) Reaction Rates. *Physical Review Letters*, 113(23):232502, 2014.

[88] N. Bohr. Neutron capture and nuclear constitution. *Nature*, 137(3461):344–348, 1936.

[89] H. Feshbach, C.E. Porter, and V.F. Weisskopf. Model for nuclear reactions with neutrons. *Physical Review*, 96(2):448, 1954.

[90] H. Fehsbach. *Theoretical nuclear physics: nuclear reactions*. John Wiley & Sons, Inc., New York, NY (United States), 1992.

[91] R.A. Henderson, J.M. Gostic, J.T. Burke, S.E. Fisher, and C. Wu. Electrodeposition of U and Pu on thin C and Ti substrates. *Nuclear Instruments and Methods in Physics Research Section A: Accelerators, Spectrometers, Detectors and Associated Equipment*, 655(1):66–71, 2011.

[92] M.S. Guttormsen, A. Atac, G. Løvhøiden, et al. Statistical gamma-decay at low angular momentum. *Physica Scripta*, 1990(T32):54, 1990.

[93] A. Schiller, L. Bergholt, and M. Guttormsen. Recent upgrades and performance of the CACTUS detector array. Technical report, Oslo Univ., Fysisk Inst., Oslo (Norway), 1998.

[94] M. Guttormsen, A. Bürger, T.E. Hansen, and N. Lietaer. The SiRi particle-telescope system. *Nuclear Instruments and Methods in Physics Research Section A: Accelerators, Spectrometers, Detectors and Associated Equipment*, 648(1):168–173, 2011.

[95] T.G. Tornyi, A. Görgen, M. Guttormsen, et al. A new fission-fragment detector to complement the CACTUS-SiRi setup at the Oslo Cyclotron Laboratory. *Nuclear Instruments and Methods in Physics Research Section A: Accelerators, Spectrometers, Detectors and Associated Equipment*, 738:6–12, 2014.

[96] M. Wang, G. Audi, A.H. Wapstra, et al. The Ame2012 atomic mass evaluation. *Chinese Physics C*, 36(12):1603, 2012.

[97] G.F. Knoll. *Radiation detection and measurement*. John Wiley & Sons, 2010.

[98] R.F. Casten, W.R. Kane, J.R. Erskine, A.M. Friedman, and D.S. Gale. States in ^{243}Pu from the (n,γ), (d,p), and (d,t) reactions. *Physical Review C*, 14(3):912, 1976.

[99] M.S. Guttormsen. MAMA Matrix Manipulation Program. Technical report, Tech. Rep. 94-05, Department of Physics, University of Oslo, 1994.

[100] M.S. Guttormsen. (private communication).

[101] G. Nelson and D. Reilly. Gamma-ray interactions with matter. *Passive Nondestructive Analysis of Nuclear Materials, Los Alamos National Laboratory, NUREG/CR-5550, LAUR-90-732*, pages 27–42, 1991.

[102] A.C. Larsen. (private communication).

[103] Data extracted using the NNDC On-Line Data Service from the NuDat 2.6 database. `http://www.nndc.bnl.gov/nudat2/`.

[104] J. Blons, B. Fabbro, C. Mazur, et al. High resolution fission probabilities for ^{229,230,232}Th(d,pf) and ^{233,236}U(d,pf) reactions. *Nuclear Physics A*, 477(2):231 – 255, 1988.

[105] B.B. Back, J.P. Bondorf, G.A. Otroschenko, J. Pedersen, and B. Rasmussen. Fission of U, Np, Pu and Am isotopes excited in the (d,p) reaction. *Nuclear Physics A*, 165(3):449 – 474, 1971.

[106] J.F. Mollenauer. A computer analysis for complex sodium iodide gamma spectra. Technical report, California Univ., Berkeley, CA (US). Lawrence Radiation Lab., 1961.

[107] C. Sükösd, W. Galster, I. Licot, and M.P. Simonart. Spectrum unfolding in high energy gamma-ray detection with scintillation detectors. *Nuclear Instruments and Methods in Physics Research Section A: Accelerators, Spectrometers, Detectors and Associated Equipment*, 355(2):552–558, 1995.

[108] A.C. Larsen. Ph.D. Thesis, 2008.

[109] A. Voinov, M. Guttormsen, E. Melby, et al. γ-ray strength function and pygmy resonance in rare earth nuclei. *Physical Review C*, 63(4):044313, 2001.

[110] S.F. Mughabghab. *Atlas of Neutron Resonances: Resonance Parameters and Thermal Cross Sections. Z= 1-100*. Elsevier, 2006.

[111] T. Young and S.D. Reeder. Total neutron cross section of ^{242}Pu. *Nuclear Science and Engineering*, 40(3):389–395, 1970.

[112] E. Rich, A. Tudora, G. Noguere, J. Tommasi, and J-F. Lebrat. Modeling of the n+^{242}Pu Reactions for Fast Reactor Applications. *Nuclear Science and Engineering*, 162(2):178–191, 2009.

[113] T. Ericson. A statistical analysis of excited nuclear states. *Nuclear Physics*, 11:481–491, 1959.

[114] T.G. Tornyi, M. Guttormsen, T.K. Eriksen, et al. Level density and γ-ray strength function in the odd-odd Np238 nucleus. *Physical Review C*, 89(4):044323, 2014.

[115] M.S. Guttormsen, M. Aiche, F.L. Bello-Garrote, et al. Experimental level densities of atomic nuclei. *The European Physical Journal A*, 51(12):1–8, 2015.

[116] M. Guttormsen, R. Chankova, U. Agvaanluvsan, et al. Radiative strength functions in $^{93-98}$Mo. *Physical Review C*, 71(4):044307, 2005.

[117] A.C. Larsen, R. Chankova, M. Guttormsen, et al. Microcanonical entropies and radiative strength functions of ^{50,51}V. *Physical Review C*, 73(6):064301, 2006.

[118] W. Thomas. Über die Zahl der Dispersionselektronen, die einem stationären Zustande zugeordnet sind.(Vorläufige Mitteilung). *Naturwissenschaften*, 13(28):627–627, 1925.

[119] F. Reiche and W. Thomas. Über die Zahl der Dispersionselektronen, die einem stationären Zustand zugeordnet sind. *Zeitschrift für Physik*, 34(1):510–525, 1925.

[120] W. Kuhn. Über die Gesamtstärke der von einem Zustande ausgehenden Absorptionslinien. *Zeitschrift für Physik*, 33(1):408–412, 1925.

[121] B.L. Berman, J.T. Caldwell, E.J. Dowdy, et al. Photofission and photoneutron cross sections and photofission neutron multiplicities for ^{233}U, ^{234}U, ^{237}Np, and ^{239}Pu. *Physical Review C*, 34(6):2201, 1986.

[122] M.A.P.V. De Moraes and M.T.F. Cesar. Photofission cross sections of ^{233}U and ^{239}Pu near threshold induced by gamma rays from thermal neutron capture. *Nuclear Instruments and Methods in Physics Research Section A: Accelerators, Spectrometers, Detectors and Associated Equipment*, 277(2):467–472, 1989.

[123] T.A. Laplace, F. Zeiser, M. Guttormsen, et al. Statistical properties of ^{243}Pu, and ^{242}Pu(n,γ) cross section calculation. *Physical Review C*, 93(1):014323, 2016.

[124] A. Bohr and B.R. Mottelson. *Nuclear Structure, Vol. II: Nuclear Deformations*. World Scientific, 1998.

[125] S. Goriely, N. Chamel, and J.M. Pearson. Skyrme-Hartree-Fock-Bogoliubov nuclear mass formulas: Crossing the 0.6 MeV accuracy threshold with microscopically deduced pairing. *Physical Review Letters*, 102(15):152503, 2009.

[126] M. Herman, R. Capote, B.V. Carlson, et al. EMPIRE: nuclear reaction model code system for data evaluation. *Nuclear Data Sheets*, 108(12):2655–2715, 2007.

[127] F. Giacoppo, F. L. Bello Garrote, L. A. Bernstein, et al. γ decay from the quasi-continuum of ^{197,198}Au. *Physical Review C*, 91:054327, May 2015.

[128] Q. Ducasse, B. Jurado, M. Aïche, et al. Investigation of the ^{238}U(d,p) surrogate reaction via the simultaneous measurement of γ-decay and fission probabilities. *Physical Review C*, 94:024614, Aug 2016.

[129] R.W. Hockenbury, A.J. Sanislo, and N.N. Kaushal. keV capture cross section of ^{242}Pu.[5 to 70 keV]. *Natl. Bur. Stand.(US), Spec. Publ.;(United States)*, 425, 1975.

[130] K. Wisshak and F. Käppeler. Neutron Capture Cross-Section Ratios of Plutonium-240 and Plutonium-242 Versus Gold-197 in the Energy Range from 50 to 250 keV. *Nuclear Science and Engineering*, 69(1):39–46, 1979.

[131] F. Zeiser. (private communication).

[132] A.C. Larsen, M. Guttormsen, M. Krtička, et al. Analysis of possible systematic errors in the Oslo method. *Physical Review C*, 83(3):034315, 2011.

[133] B.V. Kheswa, M. Wiedeking, F. Giacoppo, et al. Galactic production of ^{138}La: Impact of ^{138,139}La statistical properties. *Physics Letters B*, 744:268–272, 2015.

[134] E. Soukhovitskii, S. Chiba, J. Lee, O. Iwamoto, and T. Fukahori. Global coupled-channel optical potential for nucleon-actinide interaction from 1 keV to 200 MeV. *Journal of Physics G: Nuclear and Particle Physics*, 30(7):905, 2004.